CENTRO DE INVESTIGACIÓN Y DE ESTUDIOS AVANZADOS DEL INSTITUTO POLITÉCNICO NACIONAL

Unidad Mérida

DEPARTAMENTO DE FÍSICA APLICADA

"Metal oxides for solar water splitting: Analysis of the charge carrier dynamics at the semiconductor/electrolyte interface"

a thesis submitted by:

Ingrid Guadalupe Rodríguez Gutiérrez

In partial fulfillment of the requirements for the degree of

Doctor of Science

in

Physical Chemistry

Thesis directors:

Dr. Geonel Rodríguez Gattorno

Dr. Gerko Oskam

Mérida, Yucatán February 2019

CENTRO DE INVESTIGACIÓN Y DE ESTUDIOS AVANZADOS DEL INSTITUTO POLITÉCNICO NACIONAL

Unidad Mérida

DEPARTAMENTO DE FÍSICA APLICADA

"Óxidos de metales para la descomposición solar del agua: Análisis de la dinámica de portadores de carga en la interfase semiconductor-electrolito"

TESIS

que presenta

Ingrid Guadalupe Rodríguez Gutiérrez

Para obtener el grado de

Doctor en Ciencias

en

Fisicoquímica

Directores de Tesis:

Dr. Geonel Rodríguez Gattorno

Dr. Gerko Oskam

Mérida, Yucatán Febrero de 2019

Agradecimientos

Estos años como estudiante de doctorado me ha permitido aprender en el plano tanto profesional como personal. Esta oportunidad ha traído personas que han sido mi guía, quienes me han enseñado invaluables lecciones que llevaré conmigo por el resto de mi vida.

Quiero agradecer a Dios por permitirme vivir esta experiencia.

De igual manera, quiero agradecer al CONACYT por la beca doctoral que me brindaron para poder continuar mis estudios de posgrado. Así mismo, agradezco el apoyo económico recibido, en el marco de la Convocatoria 2014-01, del FONDO SECTORIAL CONACYT-SENER-SUSTENTABILIDAD ENERGÉTICA, dentro del Proyecto Consolidación de Laboratorio de Energía Renovable del Sureste (LENERSE) No. 254667 sub-proyecto 4, por medio del cual fue posible desarrollar la investigación y apoyar mi formación a nivel posgrado.

Agradezco el apoyo de LANNBIO (FOMIX-Yucatán 2008-108160 CONACYT LAB-2009-01-123913, 188345, 204822, 292692, 294643) en Cinvestav Mérida, por ayudarme a realizar las mediciones de SEM.

Agradezco al Dr. Geonel Rodríguez y al Dr. Gerko Oskam por aceptarme como parte de su grupo de investigación. Por brindarme su tiempo, dedicación, conocimiento; por sus consejos invaluables y por enseñarme que el éxito se encuentra de la mano con la calidad humana, muchas gracias por todo.

Agradezco al Dr. Lionel Vayssieres por brindarme la oportunidad de realizar una estancia de investigación en Xi'an Jiaotong University. Del mismo modo, agradezco al Dr. Jinzhan Su por su apoyo académico en China.

Al apoyo técnico y administrativo de M.C Beatriz Heredia, M.C Dora Huerta Quitanilla, M.C Jose Bante, M.C Daniel Aguilar,, Zhirnay Rodríguez, Sofia Alonzo y Yolanda Acosta. Ing. Gaspar Euan, Ing. Remigio Flores.

De igual manera quiero agradecer a mis compañeros de doctorado, principalmente a mis compañeros del laboratorio de nanomateriales quienes me ayudaron en los momentos que necesité. Principalmente quiero agradecer a las nanocholas, Dena, Wendy, Bety, Manuel, Alex, Maricarmen, Alberto, Lili y Renán quienes con su apoyo hicieron que el tiempo pase volando y el trabajo sea más divertido. Los quiero mucho chicos!

Agradezco a mis amigos por toda la paciencia que me tuvieron haciendo mención principal a Karla, Gabriel, David, Arely, Fercha. A todas las personas que hicieron mi estancia en China inolvidable, quienes me enseñaron la cultura de este gran país, me hicieron comprenderlo y disfrutar cada parte de él, ChenLu, Grace, Wang Jian, Fred, Carlos, Tracy, Oksana, John, Paul, ¡谢谢您!

Finalmente, pero no menos importante, agradezco a mi familia por brindarme el apoyo incondicional para poder cumplir una meta más en mi vida. Principalmente a mi mamá, mis hermanos Jorge, William y Fernando, por estar ahí en las buenas y en las malas.

Abstract

A transition from fossil fuels to renewable energy sources is necessary to start reducing the concentration of greenhouse gases in the atmosphere. Solar energy is the most promising source of renewable energy due to its abundance on the surface of the Earth, and photoelectrochemical water splitting is an ideal form of renewable energy production since the hydrogen that is produced can be utilized as a fuel with zero greenhouse emissions. However, achieving efficient water splitting has proven to be an elusive goal, and up to now no material has been found that efficiently absorbs sunlight and induces efficient water splitting. Some of the main limitations have been associated to fast recombination of charge carriers, either in the bulk or at the surface, and slow transfer kinetics from the semiconductor to the electrolyte solution. Unfortunately, the kinetic constants that describe these processes are parameters that are not easily accessible from conventional measurements.

Intensity-modulated photocurrent spectroscopy (IMPS) is a frequency-dependent technique suitable to study the charge carrier dynamics and reaction mechanisms in the photoelectrochemical cell, using an existing generalized analytical model for IMPS in electrochemical systems. In the present work, IMPS is used to determine the rate-determining steps in the charge carrier dynamics for photoelectrochemical water splitting, and we apply the generalized model to obtain the rate constants of charge transfer and surface recombination in a variety of metal oxide semiconductor materials and photoelectrode compositions and configurations.

Copper bismuth oxide ($CuBi_2O_4$) is an attractive p-type semiconductor, which meets the most important requirements to be used as a photocathode for solar water splitting. We have used inkjet printing as a novel technique to fabricate $CuBi_2O_4$ photocathodes. The steady-state photocurrent under simulated 1 sun illumination corresponding to water reduction for a 280 nm film at 0.2 V(RHE) was about 0.12 mA cm^{-2}, significantly lower than attainable for a 2 eV band gap semiconductor. IMPS has been used to distinguish between the photoelectrochemical processes involved and to determine the associated time constants, in order to gain insight in the loss processes responsible for the low efficiency.

The charge separation efficiency reaches up to 0.66 at sufficiently negative potential, however, the recombination rate constant is larger than that corresponding electron transfer to the solution. This results in a relative charge transfer efficiency between 0.2 - 0.4, explaining the low photocurrent. At low light intensity, the relative charge transfer efficiency increases up to 0.8, indicating the promise of the material. Interestingly, at sufficiently positive applied potential, the $CuBi_2O_4$ photoelectrode is characterized by a photo-oxidation process, however, the rate constant for hole transfer to the solution is small resulting in a negligible steady-state anodic photocurrent.

Tungsten trioxide (WO_3) is an interesting material to be used as a photoanode for solar water splitting. The VB is aligned with the water oxidation potential and WO_3 has a band gap of about 2.7 eV. The photoelectrochemical properties of nanostructured, porous WO_3 films deposited by screen printing have been characterized by steady-state and small signal modulation methods as a function of film thickness. Monoclinic WO_3 with a wide particle size distribution between 50 and 500 nm was synthesized by a very simple method, via the dehydration of tungstic acid. Related to its morphology and relatively large feature sizes, the optimal thickness for light harvesting and current collection is about 12 μm for front-side and about 20 μm for backside illumination. IMPS shows that the rate constant for charge transfer to the electrolyte solution is larger than that for surface recombination in most of the applied potential range, illustrating the promise of the material. However, charge collection is found to be an important process that can limit the photocurrent, especially for thicker electrodes in the photocurrent onset potential region.

A significant disadvantage of WO_3 is its limited stability under illumination in neutral electrolyte solutions; $CuWO_4$ is an attractive alternative option with much better stability. $CuWO_4$ films have been synthesized by drop casting using WO_3 nanorods as sacrificial template and a $Cu(NO_3)_2$ solution. The films annealed at 450 °C maintain the morphology of the template, and X-ray diffraction indicates that the films are composed of a $WO_3/CuWO_4$ composite. In contrast, phase-pure $CuWO_4$ films were obtained by sintering at 550 °C and 650 °C, however, the grain size and morphology changed as function of temperature. The photo-oxidation of water under front side and backside illumination

demonstrate that $CuWO_4$ suffers a charge collection problem limiting the photocurrent. The kinetic rate constants of surface recombination, charge transfer to the solution, and the photoelectrochemical cell RC time constant as a function of applied potential obtained from IMPS showed that purity and morphology influence directly surface recombination. Also, it was shown that the $CuWO_4/WO_3$ heterojunction reduce surface recombination and improves the collection efficiency related to the presence of WO_3. In addition, a $BiVO_4/CuWO_4$ heterojunction was prepared to improve absorption and to decrease surface recombination in a similar manner, which has been confirmed with IMPS measurements.

In order to optimize and evaluate different heterojunction configurations, a $WO_3/BiVO_4$ sandwich structure has been prepared by spin coating. Scanning electron microscopy images show that the particles of both phases are well interconnected forming a uniform layer of 300 nm. The I-V curves indicated that the pH plays an important role to improve the onset and the photoresponse. Measurement of the photoresponse under selective absorption conditions with a blue LED allowed to observe the charge transfer processes involved in the $BiVO_4$ component and clarified the role of WO_3 as electron collector. In contrast to the $BiVO_4/CuWO_4$ system, the external quantum efficiency of the $WO_3/BiVO_4$ system is not only determined by $BiVO_4$, implying that WO_3 also contributes.

In the last section, a preliminary study of the influence of tin doping on iron oxide photoanodes (Sn:α-Fe_2O_3) was determined using IMPS. A reduction of the photoresponse potential onset of 100 mV was observed for the doped film, which significantly improves the applicability of this system. IMPS results indicate that this is related to an improvement in the charge transfer rate in addition to a decrease of surface recombination rate in comparison of undoped films is observed.

It can be concluded that IMPS is an excellent method to evaluate the influence of the charge transfer and recombination rate constants on the efficiency of the solar water splitting process, providing important information on methods to improve performance via doping or the fabrication of heterojunctions.

Resumen

Para disminuir las emisiones de los gases que generan el efecto invernadero en la atmosfera, es necesario cambiar los combustibles fósiles por fuentes de energía renovables. Por su abundancia, la energía solar es el recurso renovable más prometedor, el cual puede ser aprovechado directamente o puede servir como auxiliar para generar combustibles limpios.

Al integrar energía solar en un sistema electroquímico capaz de disociar la molécula de agua, el hidrógeno obtenido puede ser utilizado como combustible, el cual, al ser utilizado no genera emisiones contaminantes. Sin embargo, para llevar a cabo este proceso de manera eficiente, se necesita un material semiconductor capaz de absorber de manera eficiente el espectro solar, que genere los portadores de carga y sea capaz de transferirlos a la solución. Desafortunadamente, aún no se ha encontrado el material ideal para esta tarea. Entre las limitantes encontradas para algunos semiconductores se encuentra la alta taza de recombinación de los portadores de carga, ya sea en el volumen o en la superficie, y/o una lenta cinética de transferencia desde el semiconductor hacia la solución electrolítica. Desafortunadamente, las constantes cinéticas asociadas a estos procesos no son fáciles de determinar.

La espectroscopía de fotocorriente de intensidad modulada (IMPS por sus siglas en inglés) es una técnica de frecuencia que ayuda a estudiar la dinámica de portadores dentro de una celda fotoelectroquímica. Ponomarev y Peters desarrollaron un modelo que ayuda a obtener las constantes cinéticas de recombinación y transferencia. En este trabajo, IMPS es utilizada para determinar el mecanismo de transferencia de carga en celdas fotoelectroquímicas por medio del cálculo de constantes cinéticas de transferencia y recombinación en diferentes sistemas.

En primer lugar, se empleó la técnica de impresión por inyección de tinta para sintetizar fotocátodos de $CuBi_2O_4$. La fotocorriente de estado estacionario correspondiente a la reducción de agua para una película de 280 nm a 0.2 V (RHE) fue de aproximadamente 0.12 mA cm^{-2}, lo cual es significativamente más bajo de lo que se puede obtener para un semiconductor que posee una banda prohibida de 2 eV. Con el fin de comprender mejor los

procesos de pérdida responsables de la baja eficiencia, IMPS ha sido utilizado para distinguir entre los procesos fotoelectroquímicos involucrados y para determinar las constantes de tiempo asociadas. La eficiencia de separación de carga alcanza hasta 0.66 a un potencial suficientemente negativo, sin embargo, la constante de velocidad de recombinación es mayor que la correspondiente a la transferencia de electrones a la solución. Esto da como resultado una eficiencia de transferencia de carga entre 0.2 y 0.4, lo que explica la baja fotocorriente. A baja intensidad de luz, la eficiencia de transferencia de carga relativa aumenta hasta 0.8, lo que indica el potencial del material. De manera interesante, a un potencial aplicado suficientemente positivo, el $CuBi_2O_4$ muestra un comportamiento asociado al proceso de fotooxidación, sin embargo, la constante de velocidad para la transferencia de huecos a la solución es pequeña, lo que da como resultado una fotocorriente anódica de estado estable despreciable.

Las propiedades fotoelectroquímicas de películas porosas y nanoestructuradas de WO_3 depositadas por serigrafía han sido caracterizadas por medio de IMPS en función de su espesor. El WO_3 monoclínico muestra una distribución de tamaño de partícula entre 50 y 500 nm las cuales fueron sintetizadas a partir de la deshidratación de ácido tungstico. El espesor óptimo para la recolección de luz y la obtención de fotocorriente es de aproximadamente 12 μm para la parte frontal y aproximadamente 20 μm para la iluminación de la parte posterior. IMPS muestra que la constante de velocidad para la transferencia de carga al electrolito es mayor que la de la recombinación superficial en la mayor parte del rango de potencial aplicado. Sin embargo, se considera que la colección de carga puede limitar la fotocorriente, especialmente para electrodos más gruesos.

Debido a su estabilidad en medios neutros, $CuWO_4$ es una opción atractiva para ser utilizado como fotoánodo. Las películas de $CuWO_4$ se sintetizaron por goteo utilizando de una película de nanoalambres de WO_3 con una solución 0.05M de $Cu(NO_3)_2$. Las películas sinterizadas a 450 ° C mantienen la morfología de WO_3, pero el patrón DRX indica que estas películas están compuestas por $WO_3/CuWO_4$. En contraste, las películas de fase pura de $CuWO_4$ se sintetizaron a 550 ° C y 650 ° C, sin embargo, el tamaño del grano y la morfología cambiaron en función de la temperatura. La fotooxidación del agua bajo iluminación del lado frontal y la parte trasera demuestra problemas de colección del

$CuWO_4$. Las constantes de velocidad cinética de recombinación y transferencia, así como la constante de tiempo de RC en función del potencial aplicado calculadas por IMPS mostraron que la pureza y la morfología influyen principalmente en la recombinación de la superficie. Además, se mostró que la heterounión $CuWO_4/WO_3$ reduce la recombinación superficial y mejora la eficiencia de colección de WO_3. Por otra parte; La heterounión $BiVO_4/CuWO_4$ ayuda a disminuir la recombinación superficial en el $BiVO_4$. Las mediciones de IMPS en función del potencial mostraron que la recombinación es la principal diferencia entre cada muestra. Además, se observa que la EQE máxima del sistema está dada por $BiVO_4$.

La estructura sándwich $WO_3/BiVO_4$ se depositó usando el método de centrifugación. En estas películas, las imágenes de SEM muestran que las partículas de ambas fases se encuentran interconectadas formando una capa uniforme de 300 nm. Las curvas I-V indicaron que el pH juega un papel importante para mejorar el "onset" y la fotorespuesta. Las mediciones de IMPS (con un LED azul) permitió observar los procesos de transferencia de carga en el $BiVO_4$ y mostraron que el WO_3 actúa como colector de electrones. A diferencia de la heterounión $BiVO_4/CuWO_4$, el EQE del sistema $WO_3/BiVO_4$ no solo está determinado por $BiVO_4$, lo que sugiere que WO_3 también contribuye en la transferencia.

En la última sección, se realizó un estudio preliminar de la influencia del dopaje Sn en los fotoánodos de óxido de hierro. En los espectros de IMPS se observó que existe una reducción del sobrepotencial en 100 mV para la película dopada. Para películas dopadas, la constante cinética de transferencia parece ser mayor, mientras que se observa una disminución más rápida de la constante de recombinación de la superficie en comparación con las películas no dopadas.

List of abbreviations

The following table describes the significance of various abbreviations and acronyms used throughout the thesis.

Abbreviation	Meaning
H_2	Hydrogen
O_2	Oxygen
α	Absorption coefficient
a-Fe_2O_3	Hematite
ALD	Atomic layer deposition
AO	Atomic orbital
$BiVO_4$	Bismuth vanadate
CB	Conduction band
C_H	Helmholtz capacitance
C_{SC}	Space charge capacitance
CSE	Charge separation efficiency
$CuBi_2O_4$	Copper-bismuth oxide
$CuWO_4$	Copper tungstate
DOS	Density of states
DS	Drop spacing
E_F	Fermi level
E_{fb}	Flat band potential
E_g	Band gap
EQE	External quantum efficiency
h	Plank constant
H	IMPS transfer function
HER	Hydrogen evolution reaction
IHP	Inner Helmholtz plane
IMPS	Intensity-modulated photocurrent spectroscopy
k_{rec}	Recombination rate constant
k_{tr}	Transfer rate constant
λ	Reorganization energy of the solvation shell
LHE	Light harvesting efficiency
MO	Molecular orbital
ν	Frequency
n	Density of holes
N_e	Number of electrons
NHE	Normal hydrogen electrode

$\mathbf{N_p}$	Number of holes
OER	Oxygen evolution reaction
OHP	Outer Helmholtz plane
Ox	Oxidized specie
p	Density of electrons
PEC	Photoelectrochemical
PLD	Pulsed laser deposition
PV	Photovoltaics
Red	Reduced specie
RHE	Reversible hydrogen electrode
SCR	Space charge region
Sn	Tin
STH	Solar to hydrogen
T	Temperature
VB	Valence band
$\mathbf{WO_3}$	Tungsten trioxide
$\mathbf{\Delta V_{photo}}$	Photovoltage
$\mathbf{\eta_{rel}}$	Charge transfer efficiency

Contents

List of figures

Introduction

Over the last 40 years, the intensive use and depletion of non-renewable, fossil energy sources combined with the excessive accumulation of greenhouse gases in the atmosphere has caused a wealth of energetic and environmental problems that people have to deal with every day. In order to fight against these issues, members of United Nations and the World Meteorological Organization, created the Intergovernmental Panel on Climate Change[1], which is responsible for creating overarching strategies focused on prevention and curative measures such as the reduction of CO_2 emissions from industrial sector.

Considering that the demand for energy is continuously increasing, the development and implementation of renewable energies are contemplated as one of the principal preventive actions that must be applied as soon as possible. The use of wind, hydroelectrical, nuclear, geothermal and solar energy has been employed to satisfy a part of the world's energy requirements. Unfortunately, the numbers are not yet comparable with fossil fuels.

Solar energy is the most available and abundant energy source in the world capable of supplying more than enough energy for the global energy consumption. In the past few decades, research efforts have aimed to design photovoltaic (PV) devices able to convert sunlight into electricity as alternative to electricity generation from non-renewable fuels. However, electrical energy storage systems in the market have small capacity, hence large-scale energy storage solutions need to be implemented. One alternative to overcome this problem consists in storing energy in the form of chemical fuels generated using solar energy.

Hydrogen is considered as a potential clean energy vector since H_2 possesses an energy density higher than fossil fuels and its combustion process gives water as a product. Despite the fact that H_2 is currently mostly produced by catalytic cracking of hydrocarbons, it can also be obtained employing sustainable processes. H_2 production through solar energy is a method where the photons drive a chemical reaction to split the water molecule. Light absorption and chemical cleaving of water are the principal steps involved in this process, which can be performed separate or at the same time. In the first option, the system acts as an electrolyzer, where a solar cell converts solar energy into electricity, which is then used

to drive water electrolysis. In the second case, a semiconductor photoactive material is designed to absorb photons from the solar spectrum and generate charge carriers, which are then employed to activate the oxidation-reduction reaction and produce hydrogen.

Photoelectrochemical (PEC) water splitting uses semiconductor photoelectrodes to split the water molecule. In this configuration, a semiconductor/liquid junction is created where the charge transfer processes are taking place at this boundary. In theory, solar to hydrogen (STH) efficiencies can be higher than 31.1% for dual junction cells[2]. Fujishima and Honda[3] were the pioneers of PEC cells; they showed that a TiO_2 film is capable of absorbing light, generate electron-hole pairs, and split the water molecule, demonstrating that this process is possible. From there, the scientific community has taken up the challenge to find the ideal semiconductor material for its use in a PEC system.

In the search of a good material for the synthesis of photoelectrodes, certain criteria need to be met. First, the semiconductor must be capable of absorbing sunlight, preferentially visible light since most of the photons from sunlight are found in the visible spectra. Light absorption is directly related to the band gap of the material. Secondly, the band edges need to be aligned with the redox potentials of water reduction and oxidation. The conduction band position must be higher than the reduction potential while the valence band energy has to be situated below the oxidation potential, making both reactions thermodynamically possible. It is important to highlight that intrinsic and extrinsic properties of the semiconductor present important repercussions for the charge separation and charge transport processes. Additionally, the semiconductor should exhibit excellent chemical stability in an aqueous solution under illumination. Lastly, as the process needs to be scalable in order to make an impact, the materials should be composed of inexpensive and abundant materials.[4,5]

Hence, it seems complicated to find the ideal semiconductor material for PEC water splitting. Although many materials have been studied by several groups, and their PEC performance has been improved by adding of different catalyst or heterojunction formations, mechanisms such as charge transfer processes have not yet been completely understood.

The aim of this thesis is to analyze the charge transfer processes at the semiconductor-electrolyte interface and study the influence of the intrinsic semiconductor nature on surface processes. In chapter I, the concept of PEC water splitting is explained in detail; also, a description of the electronic structure and properties of semiconductors and recent advances are given.

Chapter II describes the charge carrier dynamics in PEC systems, providing the principal basis of these processes, and introduces intensity-modulated photocurrent spectroscopy (IMPS) as a useful tool to understand the processes that occur at the semiconductor/electrolyte interface. Moreover, a theoretical model to analyze the results obtained proposed by Ponomarev and Peters is described in detail. Chapter III describes the main objectives of the thesis, and Chapter IV specifies the experimental methods.

Chapter V contains the results and discussion of several experimental systems that have been explored and is divided in 5 sections. First, the synthesis and photoelectrochemical properties of p-type copper-bismuth oxide ($CuBi_2O_4$) thin films by inkjet printing are evaluated. In the second section, a study of charge transfer and surface recombination as function of the applied potential and thickness of screen-printed, n-type tungsten trioxide (WO_3) photoanodes are examined. The next section addresses the understanding of the fundamental processes taking place at n-type copper tungstate ($CuWO_4$) photoelectrodes during water oxidation. The photoresponse enhancement due to the coupling with bismuth vanadate ($BiVO_4/CuWO_4$) is also reviewed. In the fourth section of chapter V, an insight into the charge transfer processes at $BiVO_4/WO_3$ with a sandwich-type structure is evaluated. In the last section, surface processes at the semiconductor/electrolyte and the semiconductor/catalyst/electrolyte interface for hematite (α-Fe_2O_3) and hematite doped with tin (Sn:α-Fe_2O_3) are shown to have a comprehensive role of catalyst on photoelectrode performance. General conclusions and outlooks are summarized in chapter VI.

.

Chapter I

I. Background

A general context of photoelectrochemical water splitting, the basis of semiconductor theory and the state of the art of the semiconductor materials synthesized in this work are described in this chapter.

I.1. Electrolysis of water

The electrolysis of water is defined as the breaking of water molecule into their components, hydrogen (H_2) and oxygen (O_2). In order to enhance the low conductivity of pure water, it is necessary to dissolve an acid, salt or base to form an electrolyte solution.[6]

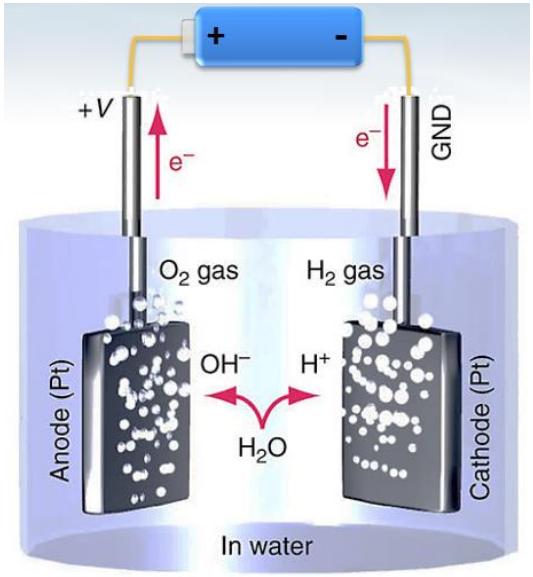

Figure I. 1. Illustration of the principal basis of water electrolysis.

Thermodynamically, this reaction is not spontaneous, implying that energy must be added to the system to break the bonds and produce hydrogen. In order to split water, two electrodes must be connected to a power source and placed into water. By applying a sufficiently high potential between the electrodes, thermodynamic and kinetic barriers are overcome to produce hydrogen at the cathode, where the electrons are transferred to the electrolyte solution, and oxygen at the anode, where electrons are collected and travel through the external circuit[6], as schematically shown in figure I.1.

The overall reaction of water splitting can be written as follows:

Overall reaction $2H_2O \leftrightarrow 2H_2 + O_2$ $E^o = 1.229\,V\ vs\ NHE$ (eq. I.1)

This process corresponds to an oxidation-reduction reaction where two half-reactions occur separately. If the electrolyte solution is acidic (pH = 0), the oxidation and reduction reactions are expressed as follows[6–8]:

Cathodic reaction $4H^+ + 4e^- \leftrightarrow 2H_2$ $E^o_{red} = 0.000\,V\ vs\ NHE$ (eq. I.2)

Anodic reaction $I_2O \leftrightarrow O_2 + 4H^+ + 4e^-$ $E^o_{red} = 1.229\,V\ vs\ NHE$ (eq. I.3)

When the pH of the electrolyte solution is basic (pH=14), both reactions can be written as follows:

Cathodic reaction $2H_2O + 4e^- \leftrightarrow H_2 + 4OH^-$ $E^o_{red} = -0.828\,V\ vs\ NHE$ (eq. I.4)

Anodic reaction $4OH^- \leftrightarrow 2O_2 + 4e^- + 2H_2O$ $E^o_{red} = 0.401\,V\ vs\ NHE$ (eq. I.5)

As can be observed, the reactions change as a function of the medium, which is related to the concentration of the ions found in the solution. As a consequence, in acidic media, H^+ ions present a higher activity than OH^- ions, while the opposite is observed in basic media. The Nernst equation (equation I.5) defines the influence of the pH on the standard potential (E^0) of the reactions:

$$E^0 = E^0_{equ} + \frac{RT}{nF} ln\left(\frac{a_{ox}}{a_{red}}\right) \quad \text{(eq. I.6)}$$

Where E^0 correspond to the standard potential, E^0_{equ} is the standard equilibrium potential, the universal gas constant R = 8.314 J/ (mol·K), T is the absolute temperature, the Faraday constant F = 96485 C/mol, n is the number of transferred electrons per ion, and a_{ox} and a_{red}

the activity of the oxidized and reduced species, respectively. If standard conditions are considered (T = 298 K), the equilibrium potential of H^+/H_2 is expressed as[8]:

$$E^0_{H^+/H_2} = E^0_{equH^+/H_2} + 0.059ln\left(\frac{a_{H^+}}{a_{H_2}}\right) \quad \text{(eq. I.7)}$$

Assuming that the solution is saturated with H_2, a_{H2} is equal to 1. As the pH is defined as the negative logarithm of the activity of H^+ the equation can be also written:

$$E^0_{H^+/H_2} = E^0_{equH^+/H_2} - 0.059pH \quad \text{(eq. I.8)}$$

Thus, the equilibrium potential of H^+/H_2 shifts by 0.059 V per pH unit. The same behavior it is observed for the equilibrium potential of OH^-/O_2. For this reason, to compare the activity of different materials in different electrolytes, the potential should be expressed versus the reversible hydrogen electrode (RHE), which takes in consideration the pH influence.

$$E^0_{RHE} = E^0_{Ag/AgCl} + 0.059pH \quad \text{(eq. I.9)}$$

Where $E^0_{Ag/AgCl}$ is 0.1976 V at 25 °C.

The water splitting process is endothermic and endergonic with an enthalpy ($\Delta H°$) of 285.9 kJ/mol and Gibs free energy ($\Delta G°$) of 237.2 kJ/mol. In order to be able to scale up water electrolysis and produce hydrogen, some energy must be applied to the electrolyzer. For this reason, many research groups focus on renewable energy thus accepting the challenge to develop the ideal semiconductor capable of absorbing sunlight to split the water molecule and obtain hydrogen by a green and sustainable method.[9–11]

I.2. Photoelectrochemical (PEC) water splitting

Solar water splitting is a green method where hydrogen and oxygen are produced from an aqueous solution, transforming the solar spectrum into chemical energy required for the redox reaction to take place. There are two main variants of water splitting processes[12]: the first is called photocatalytic water splitting, (fig II.2a) where a semiconductor in powder form is dispersed in an aqueous electrolytic solution; the suspension is irradiated with sunlight to decompose H_2O. The second way (fig II.2b) is known as photoelectrochemical

(PEC) water splitting: at least one of the electrodes is fabricated using a photoactive semiconductor. Subsequently, two electrodes are immersed in an aqueous solution, and the difference of potential generated between the electrodes when they are illuminated, should be enough to produce charge carriers and split the water molecule.

Although there are some significant differences, both configurations need a suitable semiconductor capable of absorbing photons efficiently and photogenerating charge carriers, which have sufficient energy to perform the oxygen evolution reaction (OER) and hydrogen evolution reaction (HER)[13]. Some design aspects of photoelectrodes design will be discussed in detail in the following chapters.

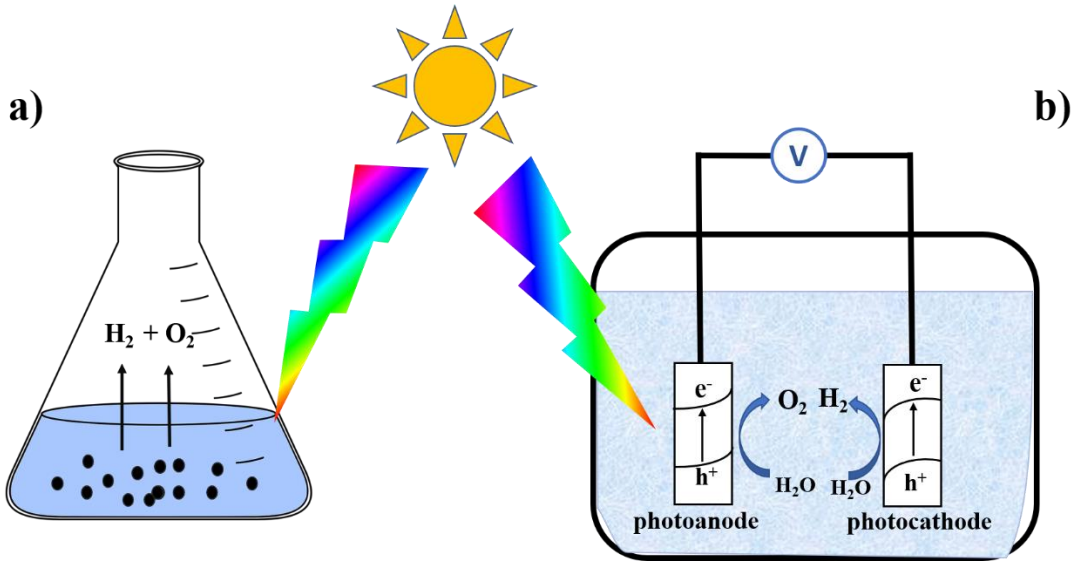

Figure I. 2. Schematic of different architectures for solar-driven water splitting a) photocatalytic configuration and b) photoelectrochemical configuration.

In 1972 the concept of water splitting was demonstrated by Fujishima and Honda.[14] Titanium dioxide (TiO_2) photoelectrodes were placed in water and illuminated with UV light to produce H_2. For the first time the idea to develop a TANDEM system capable to electrolyze water was considered around the world.

A PEC water splitting system configuration present three main variations[13] (figure I.3): (i) a photoanode coupled with a catalytic cathode, (ii) a photocathode couple with a catalytic anode, and (iii) a photoanode coupled with a photocathode. In the first two cases, the

photoelectrode must fulfill the energetic requirements; this means that generated carriers must be aligned to the OER and HER potentials. For the last case, since both electrodes are made with photoactive semiconductors, each half-reaction should take place at the suitable photoelectrode.

It is important to note that any configuration requires a direct connection between both electrodes in order to complete the circuit and allow charge transfer process to take place. In a metal-semiconductor contact (first and second case) it is not necessary to apply any external bias to make the device work, and the current density is determined by the performance of the photoelectrode. When two photoactive semiconductors are placed into the system, both electrodes supply a photocurrent and the working point of the overall device is related to the internal potential where the same photocurrent is observed in both electrodes[13,15]. If both electrodes are characterized separately, the working point of the system corresponds to the intersection point between the two current-voltage curves.

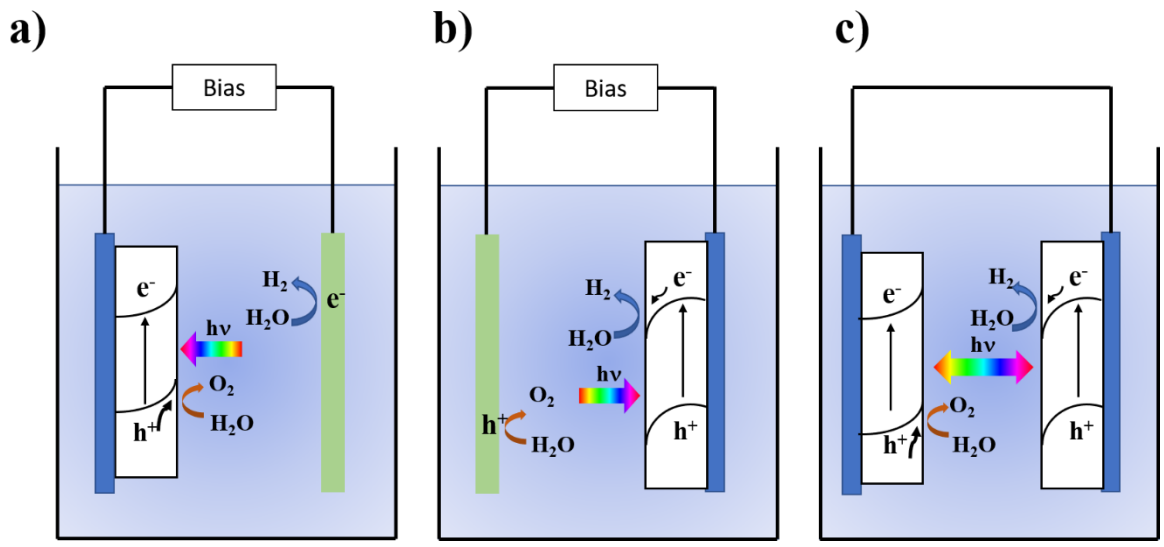

Figure I. 3. Photoelectrochemical water splitting systems using a) n-type semiconductor photoanode, b) p-type semiconductor photocathode, and c) tandem system.

As all systems mentioned above present a variety of difficulties, another configuration that has been used is by combining a photoelectrode with a solar cell. The Grätzel research group has connected two photosystems in series: a thin film of nanocrystalline WO_3 and a

dye-synthesized solar cell, where the WO_3 film absorbs the blue part of solar spectrum while the solar cell absorbs the green and red part of the solar spectrum.[16]

From the above, it is clear that semiconductors are the main key to scaling up solar water splitting. Their unique properties will be exposed in the next section.

I.3. Semiconductor fundamentals

A semiconductor is defined as a material with a conductivity that increases when the temperature increases. Compared with metals, semiconductors present an opposite behavior[17]. These materials are also defined as substances whose electrical properties are between those of metals and insulators.[18] These differences are related directly to their electronic band structure.

I.3.1. Band theory

The properties of semiconductors can be described as a function of their electronic structure, which can be described qualitatively with Molecular Orbital theory.[17,19,20] In a solid structure, the overlapping of the atomic orbitals (AO) creates several molecular orbitals (MO) with a minimal energy difference. When this effect is summed across an infinite crystal structure, the spacing between the energy levels becomes very small resulting in finite energy bands, the valence band and the conduction band.

In terms of molecular orbital theory, the overlapping of two AO produces a bonding molecular orbital and one antibonding molecular orbital. As there are a very large number of atoms in a solid, the MO number is also very large, which causes the simplification where MOs with similar energy are no longer observed as orbitals but simply as a continuous band. The energy levels filled by electrons are part of the valence band (VB) while the conduction band (CB) is associated to the empty levels[21]. The separation between those bands is known as the band gap, describing the energy space where there are no electronic energy levels.

With the help of the concept of the band gap, solid materials can be classified in three different classes (figure I.4). In case of metals, the VB is completely full while the CB overlaps, and is partially filled. As consequence, electrons easily flow through the crystal and present good conductivity properties. An opposite situation is observed for the insulator

structure, where a large band gap (E_g) is found between the VB and CB. With the VB completely filled there are no empty levels close in energy, hence, electrons cannot freely flow, resulting in a low conductivity. Lastly, the semiconductor structure presents an intermediate point between metals and insulators; their band gap is smaller than for insulators. Hence, at room temperature, there are sufficient electrons in the CB and holes in the VB to result in an intermediate conductivity. In addition, if it is applied an energy larger than E_g (via illumination or other means), additional electrons can be promoted from the VB to the CB generating a large density of mobile carriers. The conductivity is further directly related to the charge carrier mobility.[17,19,22]

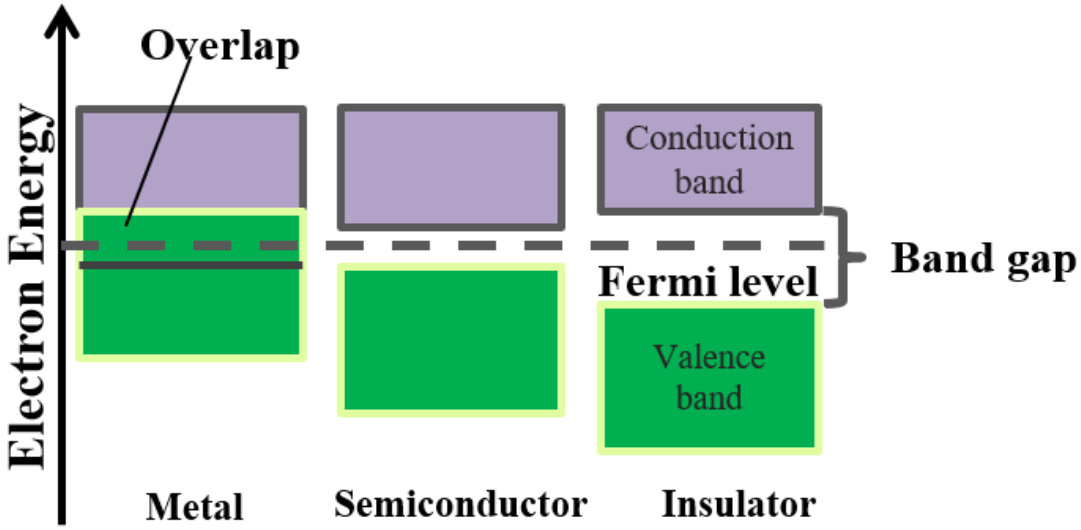

Figure I. 4. Band diagram comparison of different solid materials: metals, semiconductor and insulator materials.

It has been demonstrated that the conductivity of a semiconductor increases by doping.[13,20,23] Semiconductor materials are classified in two groups: intrinsic semiconductors, which do not include any doping agents in their structure, and extrinsic semiconductors where impurities are incorporated into the structure in order to tailor the electrical properties. In general, intrinsic semiconductors have a low conductivity as a consequence of a low mobile carrier density. When an impurity is incorporated into a semiconductor structure that needs an additional valence electron, the semiconductor behavior is classified as "p" type, where p comes from positive. In this case, the extra

needed valence electron is taken from the valence band of the semiconductor, thus leaving a hole as mobile charge carrier. However, when the doping agent has one extra valence electron, it can donate this electron to the conduction band as a mobile charge carrier; the semiconductor is called "n-type", where n comes from negative[17,19,24]. Figure 1.5 shows a schematic representation of the respective band diagrams.

In addition to affecting the conductivity, dopants or other impurities can also affect the chemical, optical and magnetic properties of the semiconductor, such as absorption and photoconductivity. The effect is sometimes desirable, but it can also be unwanted; for example, impurities may act as recombination centers, especially if the donor/acceptor level is close to the middle of the band gap. It is important to keep these aspects in mind when doping semiconductors for different applications[25,26].

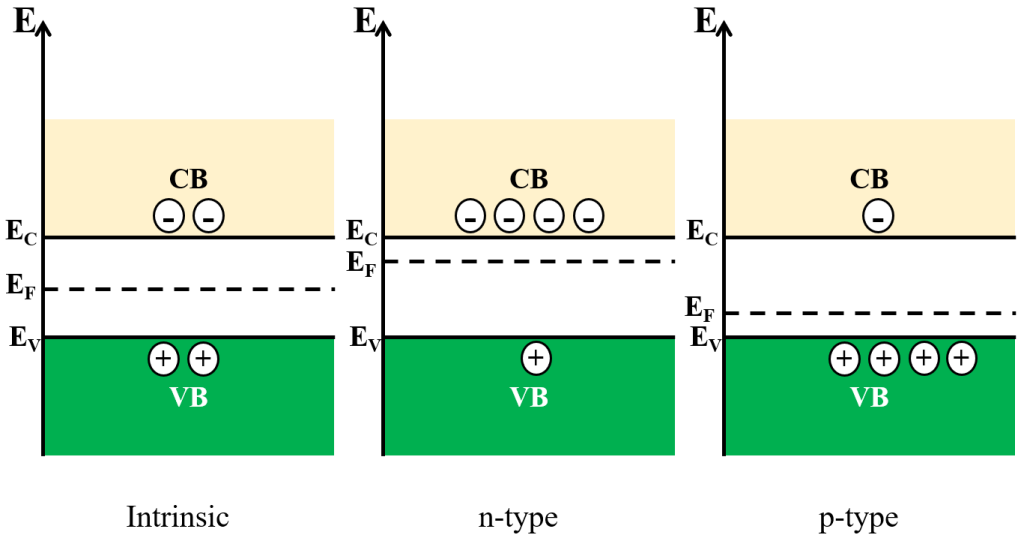

Figure I. 5. Band diagram of semiconductor types: intrinsic, n-type and p-type.

The Fermi-Dirac function represents the electron behavior in a solid. This model determines the probability that an electron occupies an electronic state with an energy *E* at a certain temperature *T*:

$$f(E) = \frac{1}{1 + \exp(\frac{E - E_F}{kT})} \qquad \text{(eq. I.9)}$$

Where k is the Boltzmann constant and E_F the Fermi level which is defined as the electrochemical potential of electrons in a semiconductor. Also, E_F corresponds to the

energy at which the probability of occupation by an electron is 0.5. For an ideal intrinsic semiconductor at T = 0 K, the VB is completely filled, while the CB is empty. Hence, the Fermi energy is in the middle between VB and CB. If the temperature increases, a fraction of thermally excited electrons is promoted to the CB, which is shown in the Fermi-Dirac distribution.

Electronic structure helps to determine parameters such as E_g, density of states (DOS) and number of carriers.[17,23,25] DOS corresponds to the number of states per interval of energy at each energy level available to be occupied.[18,19] Theoretically, at energies in the band gap, the DOS is equal to zero. For semiconductor materials, the number or holes (N_p) and the number of electrons (N_e) can be described according to the Boltzmann function because the DOS is low and, in that case, Fermi-Dirac model can be approximated by the Boltzmann equation.[27] From the density of states in the valence and in the conduction band, the density of holes p and the density of electrons n can be calculated respectively by:

$$n = N_c \exp\left(\frac{E_C - E_F}{kT}\right) \quad \text{(eq. I.10)}$$

$$p = N_v \exp\left(\frac{E_v - E_F}{kT}\right) \quad \text{(eq. I.11)}$$

N_v and N_c are the effective densities of states in the valence and the conduction band, and E_v and E_C are the energy levels of the valence and the conduction band, respectively. For an intrinsic semiconductor the density of holes is equal to the density of electrons and can be expressed as follows:

$$n \cdot p = n_i^2 = N_c N_v \exp\left(-\frac{E_g}{kT}\right) \quad \text{(eq. I.12)}$$

Where n_i is the number of holes or electrons in the intrinsic semiconductor. In case of extrinsic semiconductors, the number of electrons and holes depend on the dopant concentration.

I.3.2. Optical properties

The optical properties of semiconductors provide essential information on the electronic structure since through light absorption E_g can be determined. When the energy of incident photons is higher than E_g, the optical transitions result in an increase in the absorbance. Optical transitions can be direct or indirect (figure I.6): direct transitions are defined as

transitions where the highest energy band of the valence band is at the same wave vector *k* as the lowest CB energy levels. In case of indirect transitions, the VB maximum and CB minimum are located at different *k*. As consequence, direct transitions are possible when the electrons are excited with photons. However, in case of indirect transitions, additional to the photon energy, vibrations on the crystalline network are needed to promote the electrons from the VB to the CB.[18,19,28]

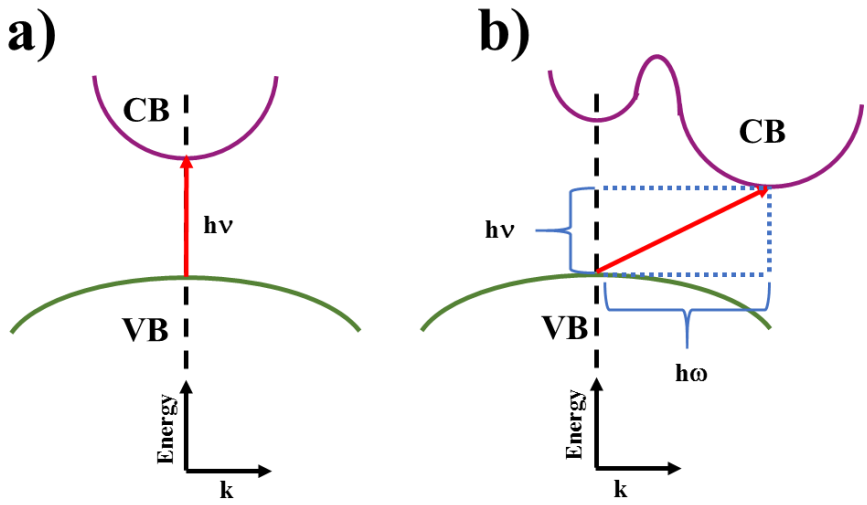

Figure I. 6. Optical transitions of semiconductors that present a) direct and b) indirect band gap.

Using UV- Vis spectroscopy, E_g can be determined.[18] Assuming that the graphs *E* vs *k* have a parabolic shape, the absorption coefficient (α) can be expressed as:

$$\alpha = \frac{A(h\upsilon - E_g)^m}{h\upsilon} \qquad \text{(eq. I.13)}$$

Where *A* is a constant and *m* depends on the optical nature of the transition: when the nature of the transition is direct *m* is equal to *1/2* while when its nature is indirect *m* is equal to *2*. The results can be analyzed using Tauc graph, where $(\alpha h\nu)^m$ is plotted against hν. A linear extrapolation until the intercept with the x axis proportions a value for E_g.

I.4. Electrolyte-semiconductor interface

In general, when two materials of different Fermi energy are brought into contact, a charge transfer process takes place until equilibrium is reached. The same situation it is observed in PEC systems where the semiconductor electrode is immersed into an electrolyte solution

with a redox couple dissolved. The redox pair is composed of oxidized (*Ox*) and reduced (*Red*) species in equilibrium:

$$Ox + ze^{-} \leftrightarrow Red \qquad \text{(eq. I.14)}$$

with z the number of electrons involved in the redox reaction.

When an electron is captured by the oxidized species forming the reduced species, the extra electron results in a change in the electrostatic interaction with the polar solvent (water); the negative pole of the solvent turn away from *Red* causing the potential energy to be smaller than that of *Ox* compared to vacuum level[17,24,27]:

$$2\lambda = E_{ox} - E_{red} \qquad \text{(eq. I.15)}$$

Where λ corresponds to the reorganization energy of the solvation shell. Considering not discrete energy levels, Gerischer[29] defined the probability *W* of finding an *Ox* or *Red* species with energy *E*:

$$W = \exp\left(\frac{(E_t - E)^2}{4\lambda kT}\right)\sqrt{\frac{1}{4\pi\lambda kT}} \qquad \text{(eq. I.16)}$$

Where E_t corresponds to the medium energy of the Ox or Red specie.

When a semiconductor gets in contact with the electrolyte solution, charge transfer reactions take place until thermodynamic equilibrium is reached, and E_F of the semiconductor equals the redox potential in the electrolyte. A charged interphase is created, resulting in potential drops both in the semiconductor and the electrolyte solution.

The region at the semiconductor-electrolyte interface can be divided in three zones (figure I.7): (i) a space charge region situated in the inner part of the semiconductor related to ionized, localized donor atoms [30–34]; (ii) the Helmholtz layer located between the solid surface and the outer Helmholtz plane (OHP), where ions are distributed uniformly to compensate the electric charge in the interface region of the semiconductor; and (iii) the diffuse double layer or Gouy-Chapman region where the remaining electrical charge is compensated in a diffuse distribution.

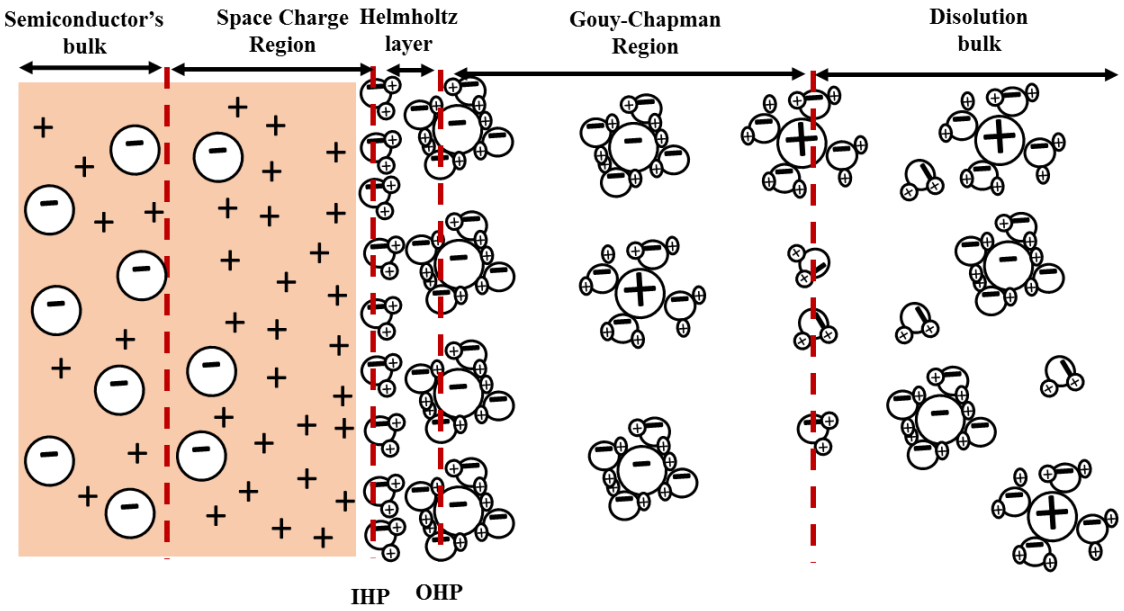

Figure I. 7. Illustration of electrolyte-semiconductor interface of an n-type semiconductor. The inner Helmholtz plane defined by the distance between the surface and the absorbed solvent or other ions.

The interface can be represented as a series of capacitances (C_H, C_{SC}, C_{GC}) in series that correspond to the capacitance of each region. Considering a high electrolyte concentration, C_{GC} can be neglected, implying that the total capacitance is dependent on C_H and C_{SC}:

$$\frac{1}{C} = \frac{1}{C_H} + \frac{1}{C_{SC}} \qquad \text{(eq. I.17)}$$

Two different situations can be distinguished:

- If $C_{SC} >> C_H$, an applied potential will be dropped over the Helmholtz layer, implying that the Fermi level of the semiconductor does not change, i.e. is pinned. In this case, when an external bias is applied, the charge carrier concentration does not appreciably change, indicating that the Fermi level is fixed in relation to the band edges.
- If $C_H >> C_{SC}$, an applied potential will be dropped over the space charge layer (SCR) in the semiconductor, implying that the Fermi level of the semiconductor shifts with external bias, resulting in a change of the charge carrier concentration at the surface; in this situation, the potential over the Helmholtz layer does not

change, implying that the band edge levels are pinned. The external bias provokes a shift on the Fermi level in reference to the band edges in the semiconductor bulk, but the edges do not change their position at the surface.

In the space charge region (SCR), also called depletion layer, a potential difference exists between the semiconductor bulk and surface ($\Delta\phi_{SC}$)[27], resulting in a driving force for charge carriers and a different electron density at the surface than in the bulk. In equilibrium the band bending in case of n-type semiconductors results from an excess of positively charged donors provoking an "upward" band banding, which is compensated by anion accumulation in the electrolyte solution at the surface. An opposite situation is observed in p-type semiconductors, where the Fermi level is below the redox potential of the electrolyte, implying that the band bending that develops is "downward".[17,24,29,35,36] The band bending diagram for n-type and p-type semiconductors are illustrated in figure I.8.

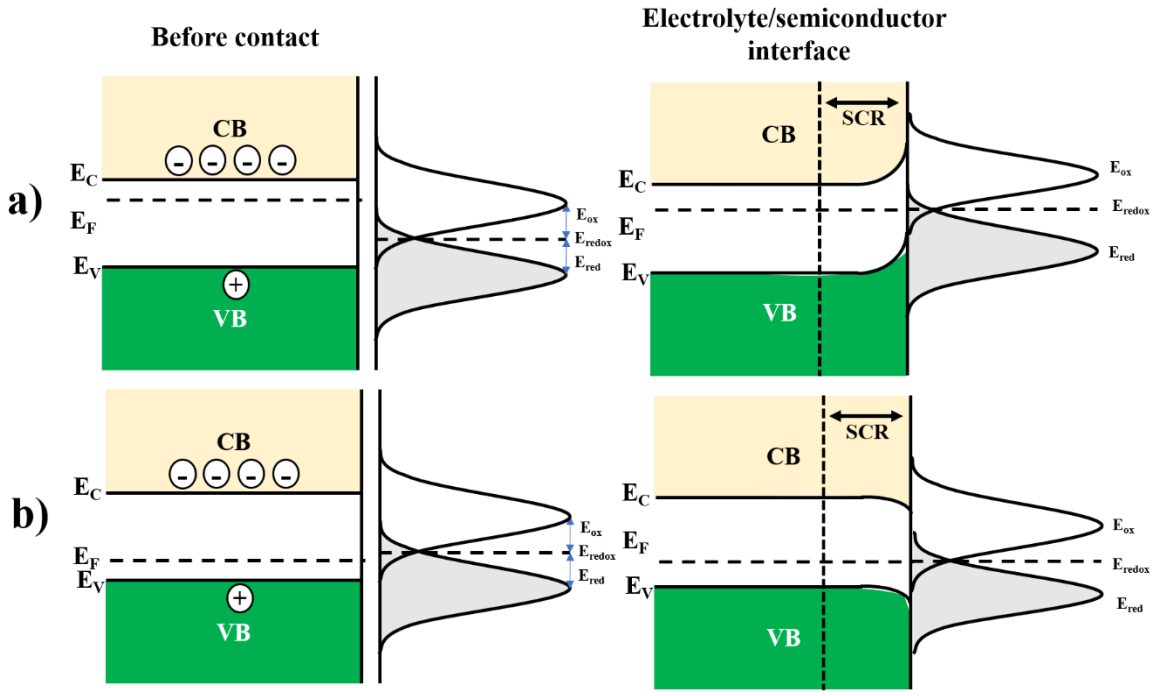

Figure I. 8. Energy diagram of a semiconductor and a redox electrolyte before and in equilibrium for an a) n-type semiconductor and b) p-type semiconductor.

The flat band potential (E_{fb}) is referred to the condition when a semiconductor in contact with another material is not polarized in the interfacial region. At this condition, the conduction and valence bands are flat and no electric field acts on the charge carriers.[26] It is important to mention that all these phenomena are held under dark conditions, if the semiconductor is illuminated additional effects are observed.

I.5. Current- potential curves

At equilibrium, the Fermi level in the semiconductor is equal to the redox potential in the electrolyte solution, and a band bending exists resulting in a lower concentration of majority carriers at the surface, n_s, than in the bulk, n_b:

$$n_s = n_b \, e^{\left(\frac{-eV_{sc}}{kT}\right)} \qquad \text{(eq. I.17)}$$

where eV_{sc} corresponds to the band bending, and n_s and n_b generally correspond to the density of electrons in an n-type semiconductor, whereas p_s and p_b are used for the hole density in p-type semiconductors; note that the sign of eV_{sc} is positive in eq. I.17).

If a positive potential is applied (reverse bias), the E_f in the semiconductor moves downward relative to the solution redox level, and the electron density at the surface decreases; electron flow from the redox system to the semiconductor becomes thermodynamically possible, however, a large barrier exists for the electrons to be injected in to the CB, resulting in a very small, positive current. On the other hand, if a negative potential is applied (forward bias), the band bending decreases and electron flow from the semiconductor to the oxidized species in the electrolyte becomes thermodynamically possible. The current will increase as the potential is made more negative and the concentration of electrons at the surface rises. Hence, the current – potential curve is characterized by a forward regime, where the current increases exponentially with applied potential, and a reverse regime, where the current is very small.

Under illumination, electron-hole pairs are produced in the semiconductor. Under open circuit conditions, the Fermi level rises by the amount of the generated internal photovoltage (ΔV_{photo}). Since there is no thermodynamic equilibrium in the space-charge region anymore, the concept of quasi Fermi energies is applied, which describes the

electrochemical potential of photo-generated electrons $E_{F,n}$ and holes $E_{F,p}$ separately (equations I.18 and I.19 respectively). Those photo-generated charge carriers can be separated across the space charge layer, or they may recombine.

$$E_{f,n} = E_C + \mathrm{kT}\ln(\frac{n}{N_C}) \quad \text{(eq. I.18)}$$

$$E_{f,p} = E_V + \mathrm{kT}\ln(\frac{p}{N_V}) \quad \text{(eq. I.19)}$$

Where E_C and E_V are the energies of the conduction and valance bands respectively, n and p the concentration of the majority charge carrier and N_C and N_V the density of states in the conduction and valance bands, respectively.

Under illumination, the majority carrier concentration is not significantly affected (under low injection conditions), however, if the generated electron – hole pairs are efficiently separated, a minority carrier flux toward the surface, and subsequent transfer to the solution can be achieved. If the charge separation efficiency is not a function of applied potential, a minority carrier flux proportional to the photon flux, i.e. light intensity, can be obtained. The net current across the illuminated semiconductor/electrolyte interface is constituted by the current due to the reactions involving photogenerated minority carriers as well as majority carriers. The Gärtner equation calculates the current - potential curves for an ideal semiconductor/electrolyte interface. In this model, recombination in the space charge layer and at the surface is neglected; however, in real systems, recombination is often important. Specifically, in the potential regime where the band bending is not sufficiently large, surface recombination may occur, effectively preventing a photocurrent to be observed. Consequently, the onset of the photocurrent shifts to potentials further into to reverse regime, until the surface density of majority carriers is so low that surface recombination becomes negligible. Additionally, OER and HER are slow processes where there are some adsorbed intermediates making this model not ideal for describe the photoelectrode behavior. Figure I.9 shows the theoretical curves for an ideal n-type semiconductor in dark and under illumination.

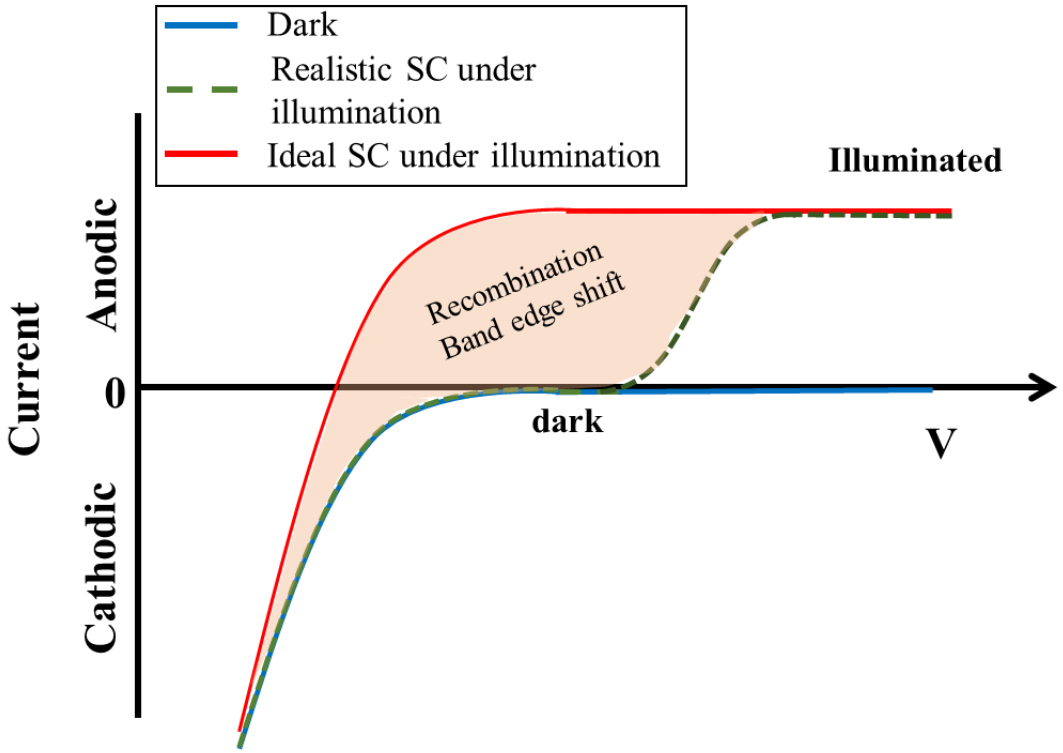

Figure I. 9. Current-potential curves for an n-type semiconductor in the dark (blue line) and under illumination. The red line corresponds to the theoretical curve of an ideal n-type semiconductor under illumination while the green dotted line represents a realistic curve of an n-type semiconductor. The difference between both curves is due to surface recombination and a possible shift of the band edges. Adapted from Ref. [37,38].

On the other hand, if recombination occurs in the SCR or at the surface, the steady state photocurrent voltage plots will deviate from the ideal form. When the electrode is illuminated, minority carriers are photogenerated; then, they move to the interface generating an instant current related to a change in the C_{SC}. The flux of minority carriers to the surface may be accompanied with trapping of charge at the surface, for example, related to partial oxidation or reduction of the surface: this leads to a change in the electrostatic equilibrium at the interface, and a shift of the band edges. This effect in general also leads to a shift of the onset potential of the photocurrent further into the reverse regime.

As a consequence of these effects, a typical current – potential curve of an n-type semiconductor is also observed in figure I.9, indicating the importance of the balance between all possible processes under illumination. The onset potential and the photocurrent

that can be achieved are both key parameters for the efficiency of solar water splitting of a certain material. In order to improve the photocurrent, charge separation should be very efficient, and in order to obtain an onset potential as far as possible towards the forward regime, surface recombination and charge trapping should be minimal; this also depends on the rate of the charge transfer processes – if charge transfer is very fast, these processes may be minimized.

For a p-type semiconductor, all the same principles hold, and the current – potential curve exhibits the same features. However, in this case the forward current is positive, and is observed at positive potentials, while the reverse region is characterized by a negative photocurrent plateau, i.e., the graphs are essentially the graph for an n-type electrode rotated by 180 degrees.

I.6. Photoelectrode design

Although many materials present photoactivity just a few of them fulfill with the requirements to be used as photoelectrode for PEC water splitting. Two of the most important requirements are directly related to their electronic structure: E_g must be larger than the enthalpy of water electrolysis and the redox potentials of each half-reaction must be aligned with the band edge positions; CB must be positioned at higher energy than the hydrogen evolution redox energy, while the VB must be at lower energy than the oxygen evolution redox energy. If these requirements are satisfied, in principle, when the semiconductor absorbs photons, an electron will be promoted from the VB to the CB, which is energetically allowed to reduce the water molecule and the hole can be transferred for the water oxidation reaction.

In order to improve the OER and HER efficiency, other parameters need to be optimized. In section I.3.2, the optical absorption concept was introduced. If the semiconductor band gap is small, photogeneration is high; however, the reaction rates may be low. In order to allow for overpotential losses for both reactions, the ideal value of E_g is around 1.6-2.0 eV.[13, 23,40] Figure I.10 shows the band edge positions and the E_g of different semiconductors used for water splitting at pH = 0.

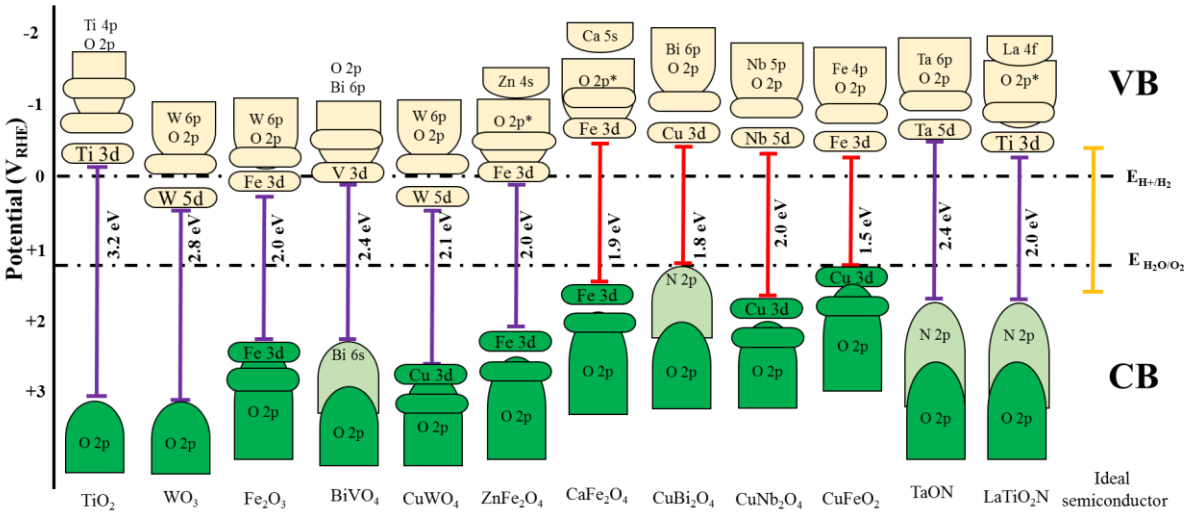

Figure I. 10. Bandgap energy of n-type (purple) and p-type (red) semiconductor materials used for solar water splitting. The potential is expressed respect to the reversible hydrogen electrode. Source Ref. [39].

Chemical stability is necessary for a long performance lifetime in an aqueous environment. If the semiconductor material presents corrosion or photocorrosion, the electrons or holes photogenerated would be used to reduce or oxidize the electrode, not to drive the water splitting reactions, and the electrode will deteriorate with time. The use of acidic or basic media might cause collateral reactions, implying that the choice of the electrolyte should be carefully analyzed for each semiconductor material.

Once the main requirements of the photoelectrodes are defined, it is important to determine if the electrodes will act as photoanode or photocathode. The minority carriers are involved in the respective water splitting reaction: holes (h^+) are the minority carriers of an n-type semiconductor, resulting in the OER and an anodic current; the electrons migrate to the bulk due to the electric field in the SCR. For a p-type semiconductor, electrons are the minority carriers, and are responsible for the HER and a cathodic current; the holes migrate to the bulk as it will be explained in section II.

I.6.1. Photocathodes

As mentioned before, p-type semiconductors constitute the photocathodes. Due to the metallic vacancies that act as VB electron acceptors, mixed oxides are often used as photocathodes. The choice of p-type photocatalysts, however, is much more limited than n-type photocatalysts principally related to the observation that p-type semiconductors are often unstable in contact with an electrolyte solution.[40]

Oxides such as NiO,[41–43] Cu_2O,[44–47] CuO,[48–50] $CaFe_2O_4$,[51–53] $CuFeO_2$[30] and $CuBi_2O_4$[54–56] are some examples of the most studied p-type oxide materials. Other non-oxide materials have been extensively studied and employed as photocathodes, including Si, GaAs, InP, GaP, nitrides, etc., however, due to their abundance, low cost, and wide variety of mixed compounds, this work is focused on mixed oxides.

Related to its high theoretical STH efficiency of around 18%[57], Cu_2O is one of the most studied oxides. It presents an E_g of 1.9-2.2 eV, indicating a good absorption of the solar spectrum.[33,44,57] Unfortunately, this oxide presents a low stability under illumination in aqueous solution both cathodically, attributed to the reduction potential of Cu, and oxidatively vía oxidation to CuO.[58] To improve its performance and stability, several strategies such as change in morphologies, addition of protecting layers or co-catalysts have been explored, [45] however, stability is still low.

Mixed oxides are a suitable option to resolve stability issues. Some of these oxides crystallize in a structure delafossite structure with a general formula of ABO_2. In this structure, oxidation states of A and B are +1 and +3, respectively. $CuCrO_2$,[59–61] $CuGaO_2$,[46] $CuFeO_2$[62] and $CuRhO_2$[63] are some delafossites that are applied in PEC water splitting. Mixed oxides can also crystallize as perovskites[64] (ABO_3), ABO_4 or $A_2B_2O_7$, which have shown a promising photocatalytic activity.

Spinel structures present a general formula of AB_2O_4. As these materials can present a p-type behavior and have a narrow band gap, their use as photocathodes are also being studied. Compounds such as $CaFe_2O_4$ and $CuBi_2O_4$ are some examples. $CuBi_2O_4$ is an attractive p-type semiconductor that presents a higher photoactivity than TiO_2 under visible light. Previous reports on $CuBi_2O_4$ films have illustrated its attractive properties for PEC applications.

I.6.1.1. $CuBi_2O_4$

Copper Bismuth Oxide ($CuBi_2O_4$) is an attractive p-type semiconductor, which meets the most important requirements to be used as photocathode for PEC water splitting. This oxide crystallizes as a spinel with a tetragonal structure with lattice parameters a = b = 8.500– 8.511 Å, c = 5.814–5.823 Å, Z = 4, and space group P4/ncc.[55,65] In the structure (figure I.11), Cu ions are connected to four O atoms to form CuO_4 planes stacked along the c axis while the Bi ion is bonded with six O atoms. Density functional theory (DFT) calculations show that the CB consists of Cu 3d orbitals while the VB contains the O 2p orbitals. Intrinsic defects associated to Cu vacancies generate free holes in the VB, accompanied by a shift of the Fermi level closer to the VB, corresponding to the p character.

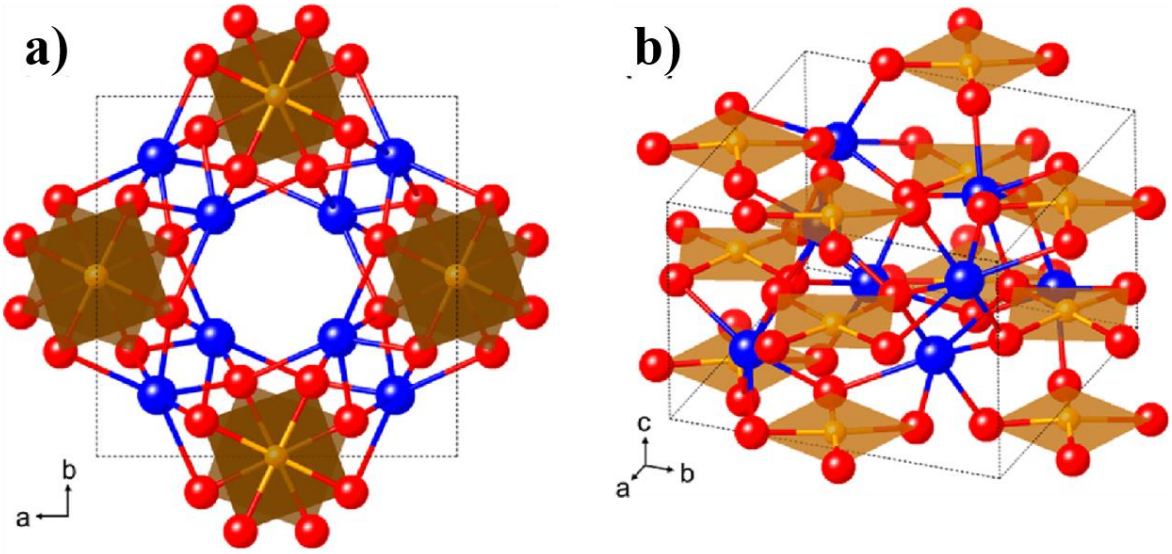

Figure I. 11. $CuBi_2O_4$ crystal structural as viewed a) along the c-axis and b) at an arbitrary angle. Bi, Cu and O atoms are represented with blue, orange and red spheres, respectively. Source: Ref [65]

Arai Takeo and coworkers demonstrated that, due to its characteristics, this oxide can be used as photocathode for PEC water splitting. $CuBi_2O_4$ has a positive photocurrent onset potential up to 1 V (RHE), and an E_g of 1.5-1.8 eV,[54–56] illustrating the potential to absorb a large part of the solar spectrum.[66,67] The conduction band minimum is estimated to be located at a more negative potential than the thermodynamic potential for water reduction enabling solar H_2 production, and its valence band maximum is located at a much more positive potential than that of other semiconductor materials, such as Si and p-type

Cu_2O.[56,66,68] Thin films have been synthesized using a variety of techniques such as drop casting, electrodeposition, spray pyrolysis and spin coating where their photocatalytic activity has been shown. Despite the high theoretical photocurrent of $CuBi_2O_4$ films of 20 - 30 mA cm^{-2}, the observed photocurrent density of the films has been significantly below this limit. It has been shown that film porosity, morphology, incomplete substrate coverage and film thickness are some of the factors that affect the PEC response. In addition, (n-type) fluorine-doped thin oxide (FTO) is generally used as substrate for $CuBi_2O_4$ films, which may negatively affect the PEC performance. Recently it has been shown that the photocurrent can be significantly increased by using a forward gradient self-doped $CuBi_2O_4$ photoelectrode and adding H_2O_2 as an electron acceptor;[47] of course, in this case, hydrogen is not generated.

To enhance the photoelectrochemical performance, the formation of junctions such as $SnO_2/CuBi_2O_4$,[69] $BiVO_4/CuBi_2O_4$,[70] $WO_3/CuBi_2O_4$,[71] and $CuO/CuBi_2O_4$[67] have been analyzed. However, although some important parameters have been determined by previous groups, the charge transfer and recombination processes and kinetics have not been well established yet.

I.6.2. Photoanodes

Photoanodes are composed of n-type semiconductors. Metal oxides with oxygen vacancies in their structure present donor sites that provide the n-type character. Photoexcited holes are transported to the interface in order to oxidize the water molecule. The disparity between the oxygen-centered VB and the OER potential at 1.23 V vs NHE presents a major challenge for the development of high-performance photoanode materials. Regrettably, few semiconductors satisfy all requirements of electronic structure and stability.

Several metal oxide materials meet several of the requirements to be tested as photoanodes for water oxidation. The redox-active metal ions in metal oxide photoanodes can include early transition metals, as well as d^{10} configuration ions. Additionally, group 1 through 3 metal ions can be added as inert components to help to produce specific crystal structures.[72] TiO_2 is one of the most studied oxide photoanodes for multiple applications, including water oxidation. Although its band gap is relatively high (3.0 - 3.2 eV), this non-toxic oxide presents good chemical stability in both acidic and basic media.[73,74] However, TiO_2 suffers

a high recombination rate and very limited light absorption. Modifications such as the addition of dopants[75–77], morphology changes[75,78–80] or conversion to titanates[81–84] have been tried to improve the performance.

In order to find alternatives to TiO_2 that harvest sunlight more efficiently, materials such as WO_3, $CuWO_4$ and α-Fe_2O_3 and their combinations have been studied. All these materials have a lower E_g and have demonstrated that their visible light absorption ability is better than TiO_2. Other groups that are promising candidates are the bismuth based oxides;[85] their electronic structure comprises of Bi 6s orbitals O 2p orbitals in the valence band, while the valence band of other metal oxides generally consists of O 2p orbitals only. This electronic band structure results in an E_g significantly smaller than 3 eV. One of the most studied oxides is $BiVO_4$, which presents remarkable optical absorption properties.

I.6.2.1. WO_3

Tungsten trioxide has been used in a variety of applications such as electrocatalysis[86–88], gas sensors,[89–91] electrochromic material[92–94] and as photoanode for PEC water splitting[95–97]. The VB is aligned with the water oxidation potential and WO_3 has an E_g of about 2.7 eV.[98,99] It has been reported that WO_3 crystallizes in different phases, but the monoclinic structure is the most active for OER. The unit cell for monoclinic structure is shown in figure I.12 and consists of 8 W atoms and 24 O atoms, where W is hexa-coordinated with O atoms.

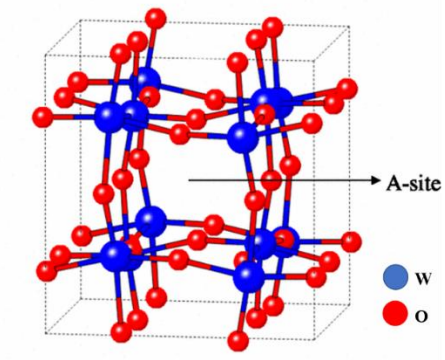

Figure I. 12. Unit cell of monoclinic WO_3. The red and blue circles represent O and W, respectively. Source: Ref. [100]

Butler and co-workers[101] showed that WO_3 can be used as a photoanode for OER. Since that moment, several different methods have been reported to synthesize the material in powder form and films. Mesoporous and compact films have been obtained by solvothermal[88,97,102,103], screen-printing,[104] electrophoresis,[105]electrodeposition,[106–108] etc.

WO_3 presents a moderate hole diffusion length (150 nm) and good electron transport properties, which helps achieving good charge extraction and low recombination rates. Unfortunately, it only can utilize 12% of solar spectrum and it presents a low stability in neutral solutions;[109]at pH > 4, the interaction with the OH^- ions dissolves the oxide. Additionally, the material suffers from photocorrosion when the water oxidation reaction is taking place. The maximum current density reported is up to 2.5 mA/cm^2, however, the use of electrochemical doping, addition of oxygen vacancies, the formation of heterojunctions ($WO_3/BiVO_4$, $WO_3/CuBi_2O_4$) or double-stack configuration have resulted in an improvement in photocurrent density. The use of Keggin-type polyoxometallates as water oxidation catalyst and Na-doped WO_3 resulted in the highest photocurrent reported under 1 sun illumination for a WO_3-based photoanode of 4.5 mA/cm^2.[110] One method to overcome stability problems in neutral media and low absorption, WO_3 can react with Cu^{2+} to obtain $CuWO_4$.

I.6.2.2. $CuWO_4$

Copper tungstate ($CuWO_4$) is an attractive n-type semiconductor that presents interesting photocatalytic properties; the material usually crystallizes in a triclinic structure (figure I.13).[111] The band edges are aligned to the water oxidation potential and the band gap (2.2-2.4 eV) is sufficiently low to classify it as a promising material that can be used as photoanode.[34,112,113] As this material is generally considered to be an indirect n-type semiconductor, a thicker film is necessary for good light absorption. However, for thicker films, the photocurrent density may be low due to a low carrier mobility related to trap states associated with Cu 3d electrons. The low current density is also associated with reduced chemical efficiency and slow surface kinetics. [113,114]

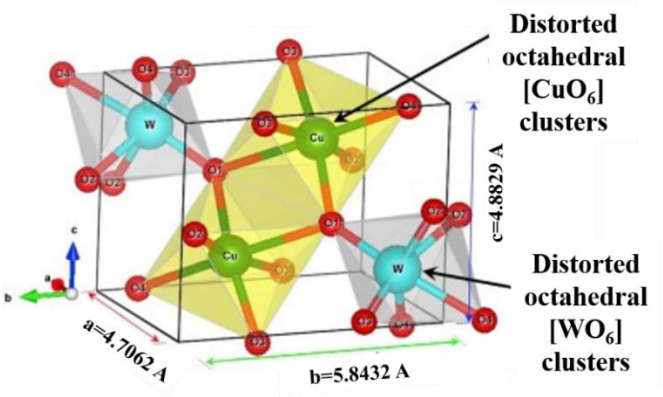

Figure I. 13. Unit cell of triclinic $CuWO_4$. Cu, W and O are represented by green, blue and red spheres, respectively. Source: Ref. [111].

In materials such as α-Fe_2O_3 and $BiVO_4$, the impact of the low carrier mobility has been mitigated by the synthesis of thin films, on the order of the carrier diffusion length.[115] However, as $CuWO_4$ presents characteristics of an indirect semiconductor, this method is not ideal.

$CuWO_4$ films have been synthesized by spray pyrolysis, electrodeposition, pulsed laser deposition (PLD), sputtering, atomic layer deposition (ALD), and more. Diverse studies have shown that $CuWO_4$ have better stability in neutral solutions than WO_3, as expected.[113] For amorphous films, it has been shown that when the composition varies, both E_g and the conductivity are affected.[116] Gaillard and co-workers investigated the effect of thermal treatment on the crystallographic and PEC properties of sputtered $CuWO_4$ films and found that annealing at 500°C under argon atmosphere resulted in a change in conductivity of the material, related to a transition from amorphous to polycrystalline material.[117]

Strategies to improve the PEC performance includes the incorporation of dopants or catalysts like Ag,[115] Fe,[118] MnPO,[119] MnNCN[120] and Co-Pi[121] on the surface. Annealing the films in an H_2 atmosphere has been used to improve the photocurrent density. $WO_3/CuWO_4$[114,119,122,123] heterojunctions have demonstrated an increase in charge collection efficiency in comparison with the pure phase. $CuWO_4$/ $BiVO_4$[124,125] displayed a shift on the onset potential for water oxidation in $NaHCO_3$ compared to Na_2SO_4.

The Hamann group studied the influence of the surface states on $CuWO_4$ electrodes by EIS and determined the hole collection efficiency in different electrolytes by IMPS.[126,127] They

concluded that surface states are acting as recombination center principally under water oxidation conditions.

I.6.2.3. $BiVO_4$

Bismuth vanadate ($BiVO_4$) is considered as one of the most promising oxides for PEC water splitting. Although $BiVO_4$ can crystallize in different phases, the monoclinic scheelite structure (figure I.14) structure is the most photoactive and has been studied extensively as photoanode.[128,129] The scheelite structure contains V ions coordinated by eight O atoms from eight different VO_4 tetrahedral units.[130] For this phase, the hybridization of Bi 6s and O 2p orbitals provoke a shift of the VB edge and reduce the E_g.[128,129,131] Additionally, an increase in the crystal size results in a decrease of band gap and a reduction of the V-O bond length, increasing the delocalization of charge carries and increasing O_2 production. [132,133] Although a good charge separation efficiency has been reported in scheelite $BiVO_4$, electron transport is limited due to the reduced overlap between the V_{3d}- V_{3d} and V_{3d}- Bi_{6p} orbitals in the CB.[39]

$BiVO_4$ has a band gap of 2.4 eV and a theoretical maximum Solar to Hydrogen (STH) efficiency of 9.2%. The carrier diffusion length for this oxide is 70 nm indicating recombination becomes important for thicker films.[134] $BiVO_4$ has been synthesized by different techniques such as spin coating, spray pyrolysis, sol-gel, hydrothermal synthesis, ALD, PLD to mention a few. To improve its efficiency, several methods have been used; one of this methods consist in replace some V^{5+} ions for W^{6+} or Mo^{6+} in order to increase the electronic conductivity and carrier collection.[135,136] Surface modifications by addition of co-catalysts such as CoPi,[137] FeOOH,[138] NiOOH[139] or Zn[140] have been used to improve the PEC response.

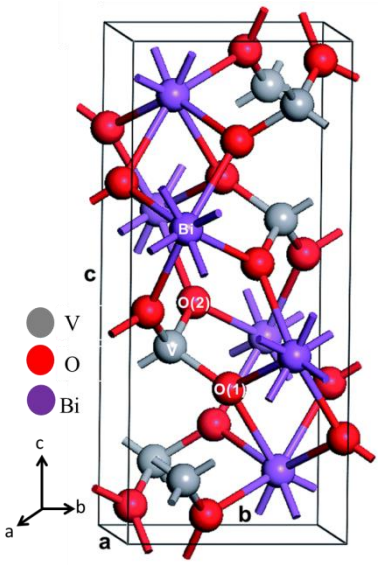

Figure I. 14. Crystal structure of scheelite $BiVO_4$. The Bi, V and O atoms are in purple, gray and red, respectively. Source Ref.[130].

The $WO_3/BiVO_4$ system have shown a photocurrent density much higher than for bare films.139–143 The exceptional light harvesting of $BiVO_4$ combined with the good electron conductivity of WO_3 make this system as one of the most potential heterojunctions for PEC water splitting. The favorable band alignment between both oxides (figure I.15), make transfer of photoexcited electrons from CB of $BiVO_4$ to the CB of WO_3 possible, followed by rapid diffusion to the external circuit, promoted by the higher charge mobility of WO_3.[141] Several groups have been investigated this heterojunction, including the implementation of a sandwich structure.[142]

Charge transfer processes have been analyzed with help of IMPS by two groups. Antuch[143] and co-workers determined that at voltages smaller than the positive photocurrent onset, the IMPS plots represent a p-type semiconductor, indicating that surface states acts as electron recombination centers but do not take part of the charge transfer process towards the electrolyte. In other work, Zachaus and co-workers[137] analyze the effect of Co-Pi on $BiVO_4$ photoanodes, and they conclude that Co-Pi decrease the surface recombination, indicating that $BiVO_4$ photocurrent is not limited by surface reaction kinetics but by surface recombination. Although charge transfer processes at $WO_3/BiVO_4$ heterojunctions have been analyzed using ultrafast transient absorption spectroscopy,[144,145] the role of each phase in the system is not yet fully understood.

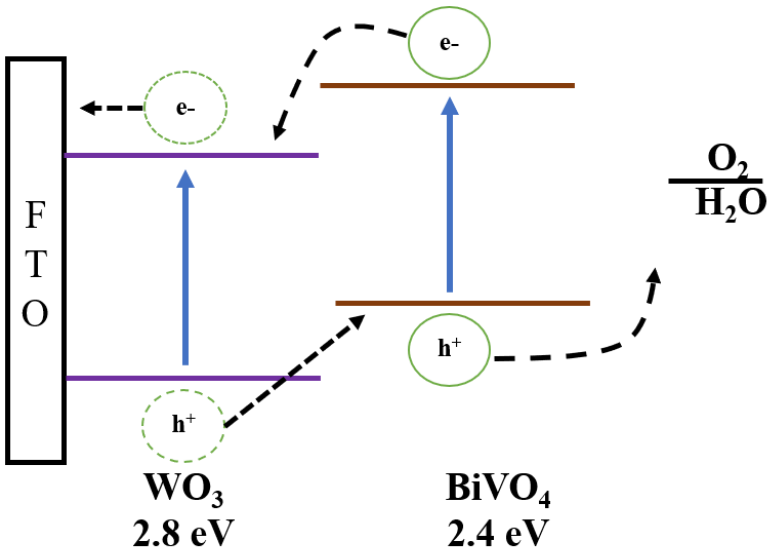

Figure I. 15. Band alignment diagram of $WO_3/BiVO_4$ heterojunction. Source: Ref. [146].

I.6.2.4. Fe_2O_3

Another interesting oxide semiconductor is Fe_2O_3, which presents several polymorphic phases, being α and γ the most studied (figure I.16). In both cases, an octahedral coordination of Fe ions is observed. α–Fe_2O_3 (hematite) presents a band gap around 2.0 - 2.2 eV; this implies that it can absorbs 40% of visible spectrum. This material also has good stability in aqueous solutions with pH > 3.[147] However, its small absorption coefficient, a low carrier mobility limit[148,149] and small hole diffusion length[150] limit its application in PEC systems. These problems are due to the compact radius of 3d orbitals, which render unpaired spins highly localized resulting in strong overlap with bridging oxo-ligands.[148]

To overcome the limitation of α-Fe_2O_3, controlled growth and doping tactics have been used; by synthesizing very thin films to correct the short hole diffusion length.[150] Morphologies such as dendrimers,[151] nanorods[152] and nanotubes[153] have been shown to exhibit improved photocurrent response performance compared to compact films.

The morphological design of an efficient hematite photoelectrode is essentially an optimization between maximizing light absorbance, minimizing the distances required for

photoelectron collection, and that of photohole diffusion to the semiconductor-electrolyte interface.

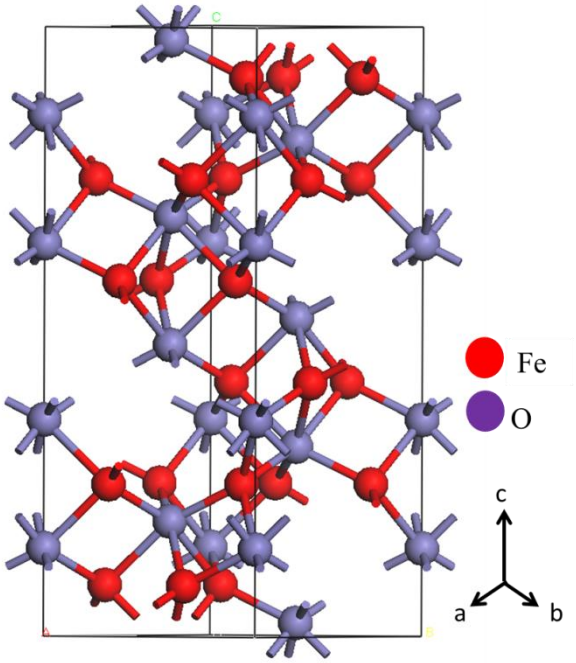

Figure I. 16. Unit cell of α-Fe_2O_3. Red spheres correspond to oxygen atoms while the blue spheres represent Fe atoms. Source: ref: [154].

Substitutional cationic doping in hematite is another strategy to improve its performance in PEC water splitting. As an electron donor, the substitution doping of Ti^{4+} at the Fe^{3+} site improves the conductivity of the iron oxide and hence the collection efficiency of the photoelectrons. Since Zn^{2+}-doped hematite has a lower charge density compared to pristine hematite, this gives a wide space-charge region that enhances photocharge separation.[155] Other dopants such as Mg^{2+},[24] Al^{3+},[25] and co-doping of Ti^{4+} and Mg^{2+},[26] have also been explored.

Peter and co-workers studied the charge transfer processes at hematite photoelectrodes and the influence of surface states on the electrode performance.[156]

Chapter II

When a PEC cell is illuminated, electron-hole pairs are produced in the photoelectrode; the processes in which charge carriers are involved to carry out the water oxidation/reduction reactions will be described in this chapter. Additionally, the use of intensity modulated photocurrent spectroscopy (IMPS) to clarify charge carrier kinetics will be discussed in detail.

II. Analysis of charge carrier dynamics in PEC systems

Three main processes are involved in the water oxidation/reduction reaction. The first process consists in generating charge carriers through light absorption. As it has been mentioned before, when the photons have an energy higher than the band gap, electron-hole pairs are generated. Then, the photogenerated electron-hole pairs must be separated by transport where drift is the dominant mechanism. This process takes place in the SCR due to the electric field present in this region. In the bulk, diffusion is the predominant process and the carrier diffusion length limits carrier transport dynamics. Carriers that are generated in the bulk with a distance to the space charge region larger than the carrier diffusion length recombine. Charge carriers that are not lost by recombination are transferred from the surface to the electrolyte, which is determined by thermodynamics and kinetics for charge transfer.

For an n-type semiconductor (figure II.1a) holes must be transferred at the interface to oxidize water, while for a p-type material (figure II.1b) electrons are the carriers transferred. Generally, oxygen evolution kinetics is a slow process because it needs four holes. The transfer of these holes does not occur at the same time, implying the presence of intermediate processes.

As the band bending is influenced by the applied bias, charge transfer processes should be analyzed at different potentials in order to elucidate the processes taking place. Furthermore, the addition of a co-catalyst can produce significant surface modifications that could increase the electrode performance by reducing recombination, changing the band bending, or speeding up charge transfer. All these processes are not observed in standard electrochemical measurements, limiting the understanding of the photoelectrode

performance. Intensity-modulated photocurrent spectroscopy (IMPS) is an AC technique that can help to elucidate the mechanism governing the performance of photoelectrodes. In the following section, the principles of this technique will be explained.

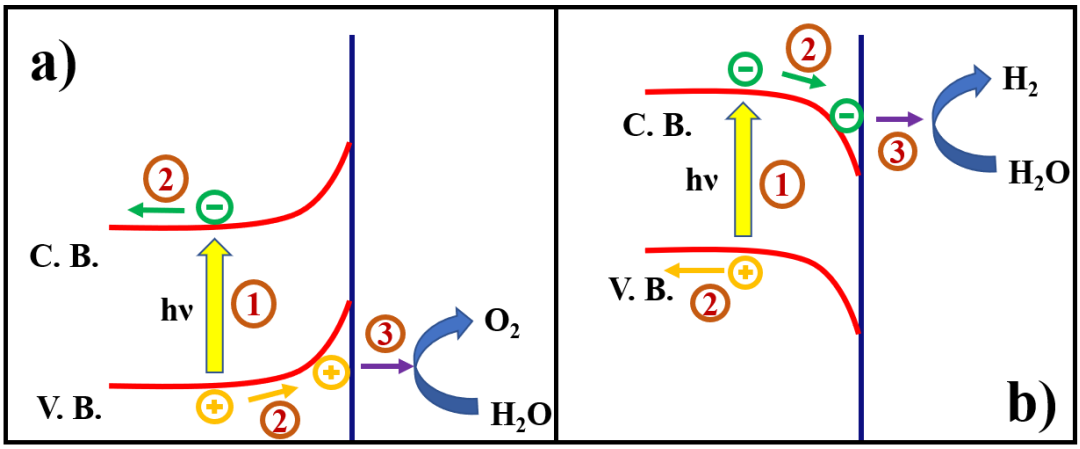

Figure II. 1. Processes involved in PEC water splitting on a) n-type semiconductor and b) p-type semiconductor: 1) photogeneration, 2) diffusion and 3) transfer of carriers.

II.1. Intensity Modulated Photocurrent Spectroscopy (IMPS)

Non-stationary techniques are particularly useful in the study of the kinetics of the processes involved in photoelectrochemical reactions at the semiconductor/ electrolyte interface.[156–161] Intensity-modulated photocurrent spectroscopy (IMPS) is a powerful small amplitude perturbation technique that allows deconvolution of the rate constants for charge transfer and recombination at illuminated semiconductor electrodes.[156] In this technique, a sinusoidally modulated, small amplitude light perturbation of variable frequency is applied to the system at a constant potential. The modulated light source can be described as follows:

$$\tilde{I} = I_0 + I\sin(\omega t) \qquad \text{(eq. II.20)}$$

Where I_0 corresponds to the intensity of the light source in DC current and $Isin(\omega t)$ is the modulation of the light intensity. A modulated response of the photocurrent with the same

frequency but with a phase shift is obtained.[137,156,159,162] figure II.2 describes the relationship between the illumination and the modulated photoresponse.

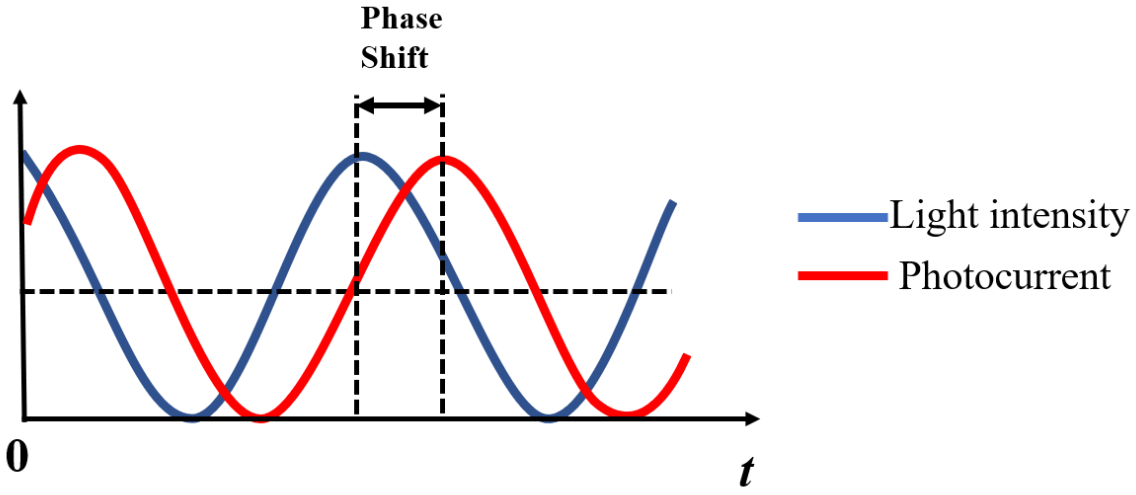

Figure II. 2. Representation of input signal and output signal on IMPS technique.

The IMPS transfer function, *H*, can be defined as:

$$H = \frac{\tilde{J}_{ph}}{\tilde{I}} = \frac{J_{ph}}{I}\exp(i\varphi) \qquad \text{(eq. II.21)}$$

where $\tilde{j}_{ph}$ is the modulated photocurrent generated because of the modulated light intensity, $\tilde{I}$ and φ corresponds to the phase shift. As the modulation on the light source is a periodic function φ can be expressed as ωt and, consequently, using Euler's formula for imaginary numbers:

$$H = \frac{J_{ph}}{\tilde{I}}\exp(i\omega t) = Re(H) + i\,Im(H) = H' + iH'' \qquad \text{(eq. II.22)}$$

with *Re(H)* and *Im(H)* the real and imaginary part of the complex transfer function, respectively.

The results can be represented in a graph plotting *Im(H)* versus *Re(H)* for the entire frequency range measured resulting in a Nyquist plot. The response is generally characterized by semicircles where the frequency at the apex represents the time constant of a specific process. If *H* is a real number, its value represents the external quantum

efficiency (EQE) for the conversion of incident photons in charge carriers. Figure II.3 shows a typical spectra that can be obtained by measuring IMPS.[157,158,162] First, the high frequency semicircle corresponds to the time constant for current collection, and is related to the cell time constant or, alternatively, to the charge carrier transport time constant: at very high frequency, no modulated photocurrent is measured as the current-generating process cannot follow the modulation. With decreasing frequency, an out-of-phase photocurrent can be observed, which at a sufficiently low frequency can follow the modulation, resulting in an in-phase signal. The crossing point on the real axis of the resulting semicircle in the *Im(H)* vs. *Re(H)* plot at medium frequency corresponds to the charge separation efficiency (*CSE*) across the electric field, such as that in the space charge layer, for the case where the light harvesting efficiency (*LHE*) is 1. If only a fraction of the incident photons is absorbed, then the intercept is a measure for the product of the light harvesting and charge separation efficiencies *(CSE)*. As such, the intercept can be interpreted as the maximum attainable external charge collection efficiency, in the absence of losses due to recombination. Note that within a modulation cycle for a p-type semiconductor (figure II.3a) the negative photocurrent increases when the light intensity increases, resulting in the negative sign of *Re(H)* and the location of the semicircle in the third quadrant.

The semicircle in the second quadrant represents the competition between electron transfer to the solution and surface recombination processes: the intercept of the low frequency arc in the IMPS plot for $\omega \rightarrow 0$ is directly related with the external quantum efficiency (*EQE*), i.e., the steady-state photocurrent.[156–163] Note that for surface recombination, a charge carrier needs to travel across the electric field in opposite direction, which results in a decrease of the collection efficiency and (modulated) current observed in the external circuit; bulk recombination does not result in a change of the observed current upon modulation of the light intensity and can hence not be directly investigated using IMPS. There are three expected results for three different electron transfer efficiencies (figure II.3a, b): if charge transfer to the solution is much faster than surface recombination, the loop in the second quadrant is not observed, while in the case that surface recombination is much faster than charge transfer, the upper loop ends back in the origin. For a relative transfer efficiency of 0.5, the upper loop intersects with the *Re(H)* axis

halfway. For a given photoelectrode, one would expect the time constant of the lower loop in the third quadrant to be independent of the charge transfer efficiency, as long as the time constants are at least 2 orders of magnitude apart.

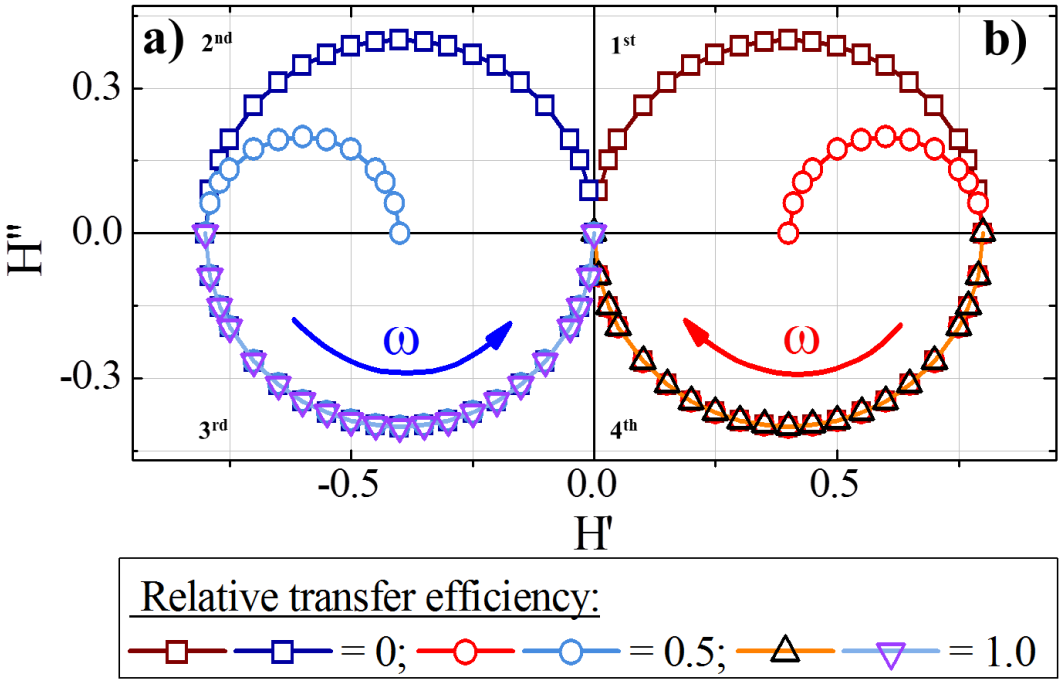

Figure II. 3. Schematic IMPS for a) p-type and b) n-type semiconductors. The lower loop (3rd and 4th quadrant) corresponds to the cell time constant while the upper loop (1st and 2nd quadrant) reveals the competition between charge transfer and recombination.

For an n-type semiconductor, a positive photocurrent is measured and in IMPS plot (figure II.3 b) the same features are observed, but since in this case the photocurrent is positive, the spectrum is the mirror image in the *Im(H)*-axis. Note that for a doped semiconductor, the majority carrier density is generally orders of magnitude larger than the photogenerated carrier density, and a photocurrent is not observed in the forward regime.

Hence, a lot of information can be obtained from IMPS Nyquist plots, however, the results need to be analyzed in more detail using a model; in this work, we apply the model proposed and developed by Ponomarev and Peter.[157]

II.2. Model

To analyze the IMPS spectra in more detail, the above discussed balance of charge transfer to the solution and surface recombination can be quantified using the simple model in figure II.4a. The analysis of the competition between hole transfer and surface recombination at the semiconductor/electrolyte interface and the deconvolution of the reaction rate constants can be possible if some considerations are assumed. First, bulk processes (e.g., band-to-band recombination, trapping) are supposed to be non-significative in comparation of surface processes. Since bulk recombination processes are much faster than surface processes, this assumption is likely to hold. Moreover, the relevant processes should occur on the same time scale as the IMPS measurements, which is indeed the case for most surface recombination processes. Lastly, the band bending is assumed to remain constant during the modulated illumination. This is true if the space charge capacitance and the density of majority carriers do not change significantly during the modulation of the light intensity. So, considering the upper semicircle which is related to surface processes, the transfer function *H* can be defined as follows:

$$H = \frac{\tilde{j}_{ph}}{\tilde{I}} = \left(\frac{j_0}{j_{photon}}\right) \frac{k_{tr} + i\omega}{k_{tr} + k_{rec} + i\omega} \qquad \text{(II.23)}$$

where j_0 and j_{photon} are the amplitudes of the modulated photocurrent (*electrons* cm^{-2} s^{-1}) and incident photon flux (*photons* cm^{-2} s^{-1}), respectively; hence, for the case where the second term of the equation is equal to 1, j_0/j_{photon} equivalent to the maximum obtainable external quantum efficiency (*EQE*). This can be achieved in two ways: (i) when the charge transfer rate constant, k_{tr}, is much larger than the surface recombination rate constant, k_{rec}, and $i\omega$; and (ii) for sufficiently high frequencies.

As for the second condition, it should be noted that the *RC* time constant of the cell is not taken into account in this simple model: if the *RC* time constant is at least two orders of magnitude smaller than the charge transfer and recombination time constants, then the processes are sufficiently separated to be analyzed with eqn. (II.20); in this case, condition (ii) is reached for intermediate frequencies, before the onset of the *RC* loop at higher frequencies.

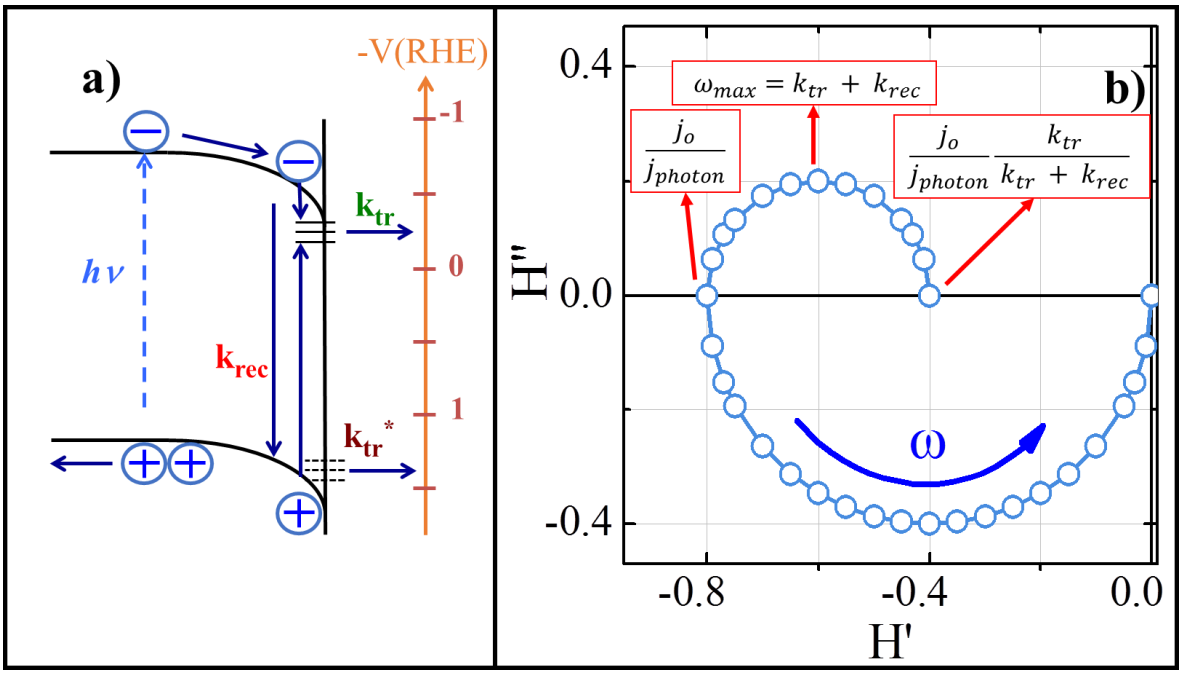

Figure II. 4. a) Band diagram illustrating the processes taking place at a photocathode. Minority carrier electrons can be trapped at the interface and subsequently either be transferred to the solution or recombine with holes. Holes may also be trapped at the surface and be transferred to the solution. b) Theoretical IMPS plot of a typical photocathode to represent the calculation and interpretation of charge transfer and recombination rate constants.

In this case, the imaginary photocurrent reaches a maximum when the frequency matches the characteristic relaxation constant of the system:

$$\omega_{max} = k_{tr} + k_{rec} \qquad \text{(II.24)}$$

Additionally, the high and low frequency intercepts with the x-axis correspond to the initial maximum and the steady state photocurrents in a photocurrent transient plot, respectively. At the high frequency intercept, recombination is "frozen" due to fast modulation, which means that the measured current is equal the maximal current that the electrode can be achieved without recombination (j_0/j_{photon}).

The low frequency intercept then represents the fraction of the transferred minority carrier flux to the overall surface processes (transfer and recombination). This point corresponds to the charge transfer efficiency (η_{rel}) multiplied by, j_0/j_{photon}. Figure II.4b) summarize the relations with k_{tr}, k_{rec} and IMPS plot; η_{rel} describes the fraction of the minority carrier flux that is involved in the charge transfer reaction:

$$\eta_{rel} = \frac{k_{tr}}{k_{tr} + k_{rec}} \quad \text{(II.25)}$$

It is important to mention that the amplitude of the applied modulation should be small enough to ensure a linear response of the electrodes that can be confirmed by Lissajous plots. If IMPS is used correctly, it could be a helpful tool to understand the charge carrier dynamics in the electrolyte/semiconductor interface.

Chapter III

III. General objective

Following the previous backgrounds, one could envisage the photoelectrochemical water splitting as based on three fundamental steps, namely: i) photon absorption and charge carrier generation within the active phase, (ii) the dynamics of charge separation and transport to the interfaces, and (iii) charge transfer processes at the semiconductor / electrolyte interface corresponding to the electrochemical reactions involved in water splitting. Note that the optical processes in several semiconductor oxides are well studied and many of them can accomplished excellent performance on charge generation during photon absorption; on the other hand, the electrode reactions during water splitting is also a well-understood phenomenon which has been under study since the work carried by Michael Faraday more than a century ago. However, the study of the dynamic of charge carriers transfer have had to wait for the establishing of novel fast tools of characterization such as the electrochemical impedance spectroscopy that consolidates with the development of frequency response analyzers in the 1970s. The understanding of the charge transport processes allows the improvement of the materials to increase the efficiency of PEC cells.

The general objective of the present work is to investigate the charge carrier dynamics in both n-type and p-type semiconducting metal oxide materials for solar water splitting, including $CuBi_2O_4$, WO_3, $CuWO_4$, $WO_3/BiVO_4$ and α-Fe_2O_3, using small-signal modulation techniques, in particular intensity-modulated photocurrent spectroscopy, and to determine the balance between charge separation, recombination either in the bulk or a the surface, and charge transfer to the solution. These oxides are composed of earth-abundant elements and their properties make them promising materials to be used as photocathodes or photoanodes for solar water splitting. Different synthesis methodologies such as inkjet printing, screen printing, hydrothermal methods, spin coating and anodization were employed to prepare a variety of semiconducting oxide films and heterojunction photoelectrodes.

Chapter IV

IV. Experimental section

IV.1. Photoelectrode synthesis

Prior to deposition, fluorine-doped tin oxide (FTO) coated glass substrates TEC 15 (2 cm x 2 cm) were cleaned by sonication in Liquinox phosphate-free detergent (Aldrich), deionized water and isopropanol for 20 min each.

IV.1.1. $CuBi_2O_4$ photocathodes

The $CuBi_2O_4$ photocathodes were synthesized in CINVESTAV-Mérida as follows: 3 mmol $Bi(NO_3)_3 \cdot 5H_2O$ (Aldrich; 98%) and 2 mmol $Cu(NO_3)_2 \cdot H_2O$ (Aldrich; 99.99%) were dissolved separately into a solution containing 35% diethylene glycol, 1% diethylene glycol monobutyl ether and 64% of acetic acid. The solutions were mixed and sonicated for 30 min and then diluted to 10 mL. The DIMATIX inkjet printer (figure IV.1) was used to print the films, using 10 pL cartridges with the precursor solutions jetting voltage and frequency of 15 V and 5 kHz, respectively. After deposition, the films were sintered in air for 90 min at 650 ºC in a Thermo Scientific Lindbergh Blue M box furnace.

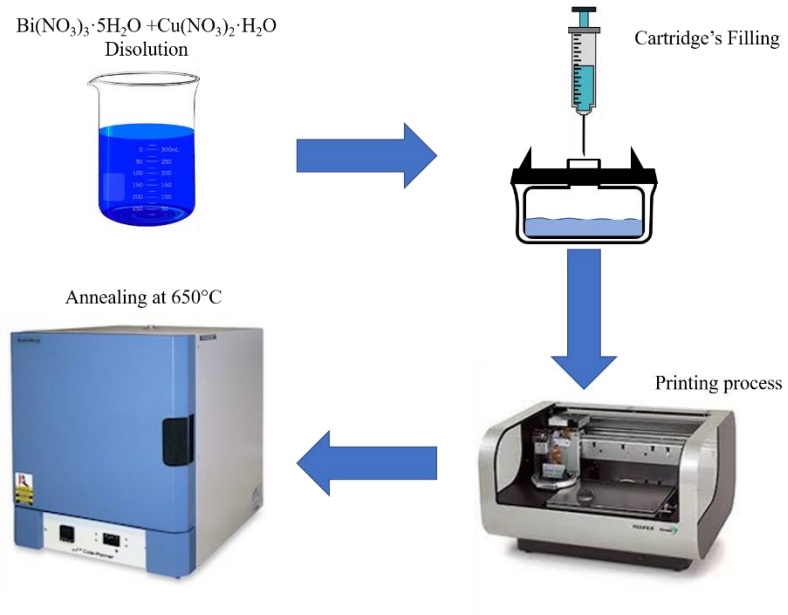

Figure IV. 1. Scheme of synthesis of $CuBi_2O_4$ photocathodes.

IV.1.2. WO_3

Synthesis and characterization of WO_3 were done in CINVESTAV-Mérida.

Synthesis of monoclinic WO_3. Tungsten trioxide was synthesized using hydrated tungsten acid as a precursor material (H_2WO_4•$2H_2O$, Aldrich 99%) in a thermal method as reported previously.[164] For this purpose, an amount of H_2WO_4•$2H_2O$ was introduced in a furnace and heated for 2 hours at 550 °C (5 °C/min.).

Preparation of WO_3 paste. The powder obtained was used for the preparation of WO_3 paste, where 0.1 g of WO_3 was dispersed in 10 mL isopropyl alcohol ($CH_3CHOHCH_3$ J.T. Baker > 99.88 %) with an ultrasonic Ti horn (130 W, 50% amplitude) for 15 min; then, 1 mL α-terpineol ($C_{10}H_{18}O$, Fluka, 97%) was added and mixed for 15 minutes, 0.03 g ethyl cellulose (100 cp, Aldrich, 48%) previously dispersed in 10 mL isopropyl alcohol was added to the first solution and mixed for 30 minutes. The excess ethanol in the final dispersion was removed with a rotary-evaporator until a paste with a desirable viscosity was obtained.

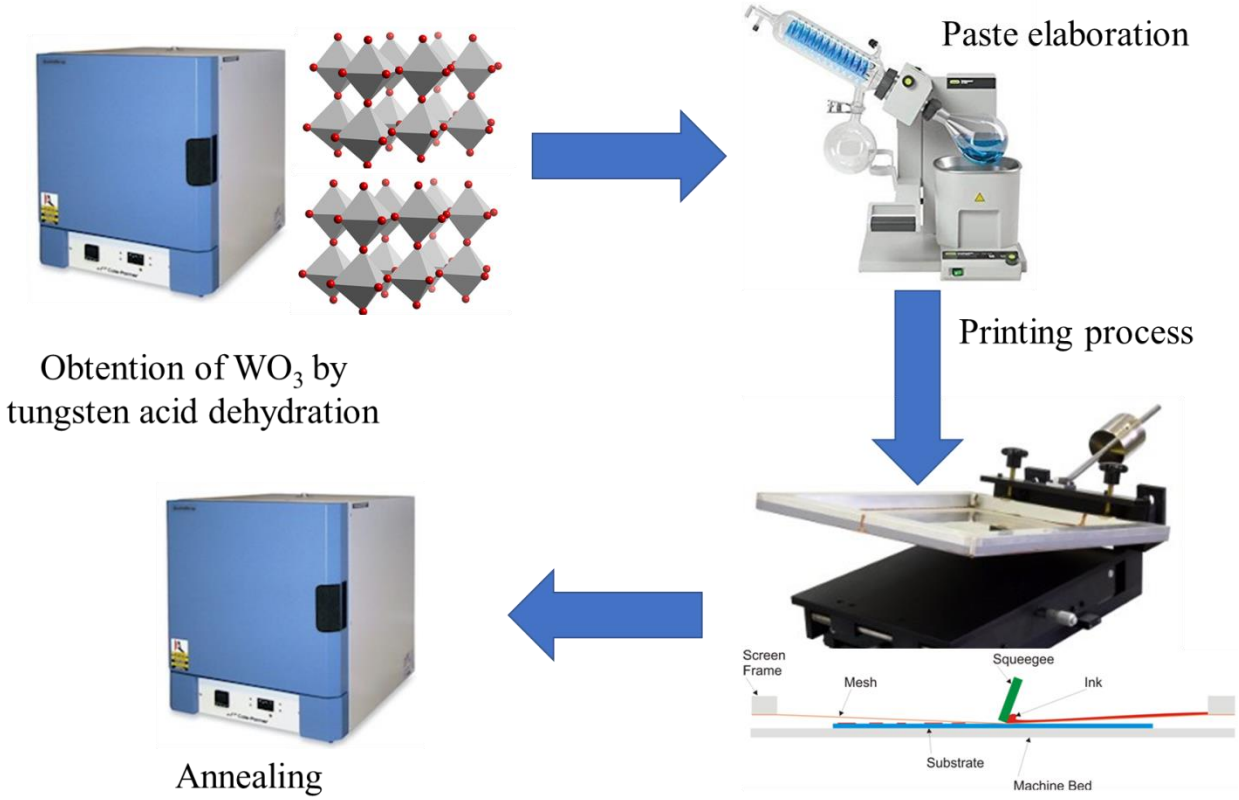

Figure IV. 2. WO_3 films synthesis procedure.

Deposition of WO_3 films. The films were deposited using the screen-printing method (figure IV.2) with a polyester screen having a mesh opening w = 60 μm, thread diameter d = 50 μm and 90 threads per cm. The screen allows printing films with a circle-shaped design of 1 cm in diameter, which will be the effective area of the working electrode. The stored WO_3 paste was ultrasonically mixed for 1 hour before film deposition. A circular layer of the WO_3 paste was coated on the FTO glass by screen printing and was dried under ambient condition for 10 minutes at 125 °C in a hot plate. This procedure was repeated several times, to obtain electrodes of different thickness. The FTO substrates coated with the paste were gradually heated (2.5 °C/min) to 550 °C for 60 minutes in ambient atmosphere to remove the organic materials and facilitate the interconnection of WO_3 particles. The films were generally whitish green, opaque in appearance, which is related to use of powder aggregates for the preparation of the paste.

IV.1.3. $CuWO_4$

Synthesis and structural characterization of $CuWO_4$ films were held in the International Research Center for Renewable Energy in Xi'an Jiaotong University while photoelectrochemical measurements including IMPS were performed in CINVESTAV Mérida.

Synthesis of WO_3 nanorod array precursor film. The WO_3 nanorod array films were synthesized follow the methodology developed by Liu *et. al*[165]. 1 g of Ammonium paratungstate ($H_{40}N_{10}O_{41}W_{12}{\cdot}xH_2O$) was heated in lactic acid until complete dissolution to get a final concentration of 10 wt %. Then, 1 mL of the solution was diluted 10 times by volume with ethanol to obtain the seed layer precursor solution. The precursor solution was deposited on the substrate via spin-coating at 3000 rpm for 15 s. The coated substrates were annealed at 500 °C for 3 h in a furnace to get the WO_3 seed layer.

The substrates with the seed layer were placed into a Teflon-lined hydrothermal reactor filled with the precursor solution that was prepared by mixing 1.25 g of an ammonium paratungstate solution (10 wt %) with 8.75 g of lactic acid in 20 g of ethanol containing 0.1383 g of L-glutathione reduced ($C_{10}H_{17}N_3O_6S$). The reactor was positioned onto a stainless-steel autoclave and heated at 200°C for 4 h. The obtained films were rinsed with ethanol and annealed in air at 550°C for 1 h.

Synthesis of $CuWO_4$ porous films. WO_3 nanorods array were used as sacrificial template to fabricate $CuWO_4$ films. A certain amount of $Cu(NO_3)_2$ was dissolved in acetic acid to obtain a 0.05M as final concentration. 50 µL of the Cu^{2+} solution was drop-casted onto the surface of the WO_3 nanorods array and dried in air at room temperature. The procedure was repeated 3 times and then, the samples were annealed in air at different temperatures (450 °C, 550 °C, and 650°C). Figure IV.3 schemes the process.

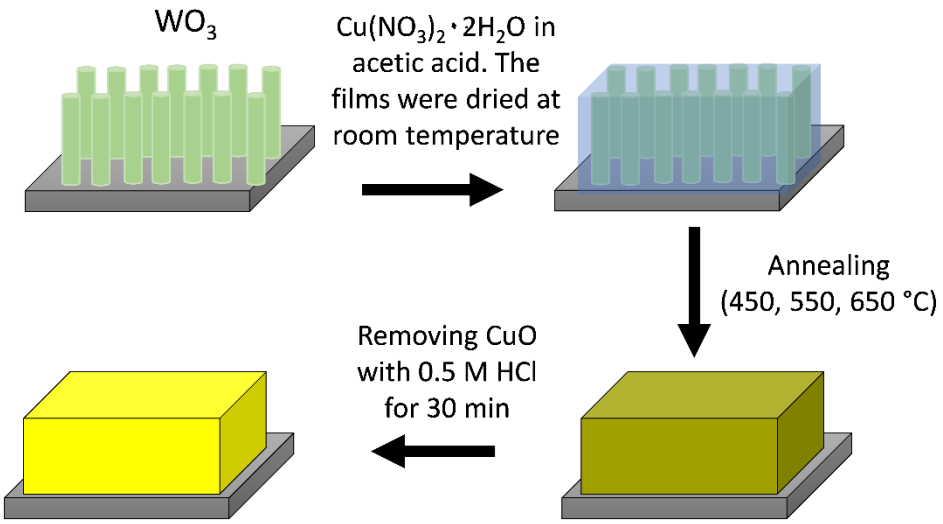

Figure IV. 3. Obtention of $CuWO_4$ porous films.

Preparation of $BiVO_4$-$CuWO_4$ heterojunction. To prepare $BiVO_4$/$CuWO_4$ electrodes, first, a bare film of $CuWO_4$ was synthesized by the method previously described. Subsequently, a layer of $BiVO_4$ precursor solution was deposited by spin-coating at 3000 rpm for 30 s and subsequently annealed onto a rapid thermal annealing furnace at 500 °C for 120 s. The procedure was repeated 3 times, and finally annealed at 500°C for 2 hours in air atmosphere. The $BiVO_4$ precursor solution (0.125 M) was prepared with 0.01 mol of $Bi(NO_3)_3$ x $5H_2O$, 0.01 mol NH_4VO_3 and 10 mL concentrated nitric acid (HNO_3) and 30 mL of de-ionized water, then mixed with 40 mL PVA solution (5g/100 mL).

IV.1.4. $BiVO_4$/WO_3 system

Synthesis and structural characterization of films were held in the International Research Center for Renewable Energy in Xi'an Jiaotong University while photoelectrochemical measurements including IMPS were performed in CINVESTAV Mérida.

Preparation of spin coated $BiVO_4$-WO_3 sandwich heterojunction. WO_3 precursor solution (0.125 M) was prepared as follow: 0.01 mol tungsten acid (H_2WO_4) and 25 mL H_2O_2 (30 wt%) were dissolved in 15 mL de-ionized water (H_2O), then mixed with 40 mL of a PVA (poly vinyl alcohol) precursor solution (0.5 g PVA dissolved in 10 mL H_2O). For the $BiVO_4$ precursor solution (0.125 M), 0.01 mol Bi $(NO_3)_3 \cdot 5H_2O$, 0.01 mol NH_4VO_3 and 10 mL concentrated HNO_3 were dissolved in 30 mL de-ionized water, then mixed with 40 mL PVA solution.

The sandwich structure was synthesized by spin-coating overlapping the deposit of WO_3 and $BiVO_4$ layer by layer, the spin rate was controlled at 3000 rpm for 30 s. After each deposition, the layers are sintered on the rapid thermal annealing furnace at 500 °C for 120 s. After all deposits, the samples are annealed at 500 °C for 2 hours. The scheme of the processes is observed in figure IV.4. Phase pure films were deposited by spin coating repeating the process 3 times.

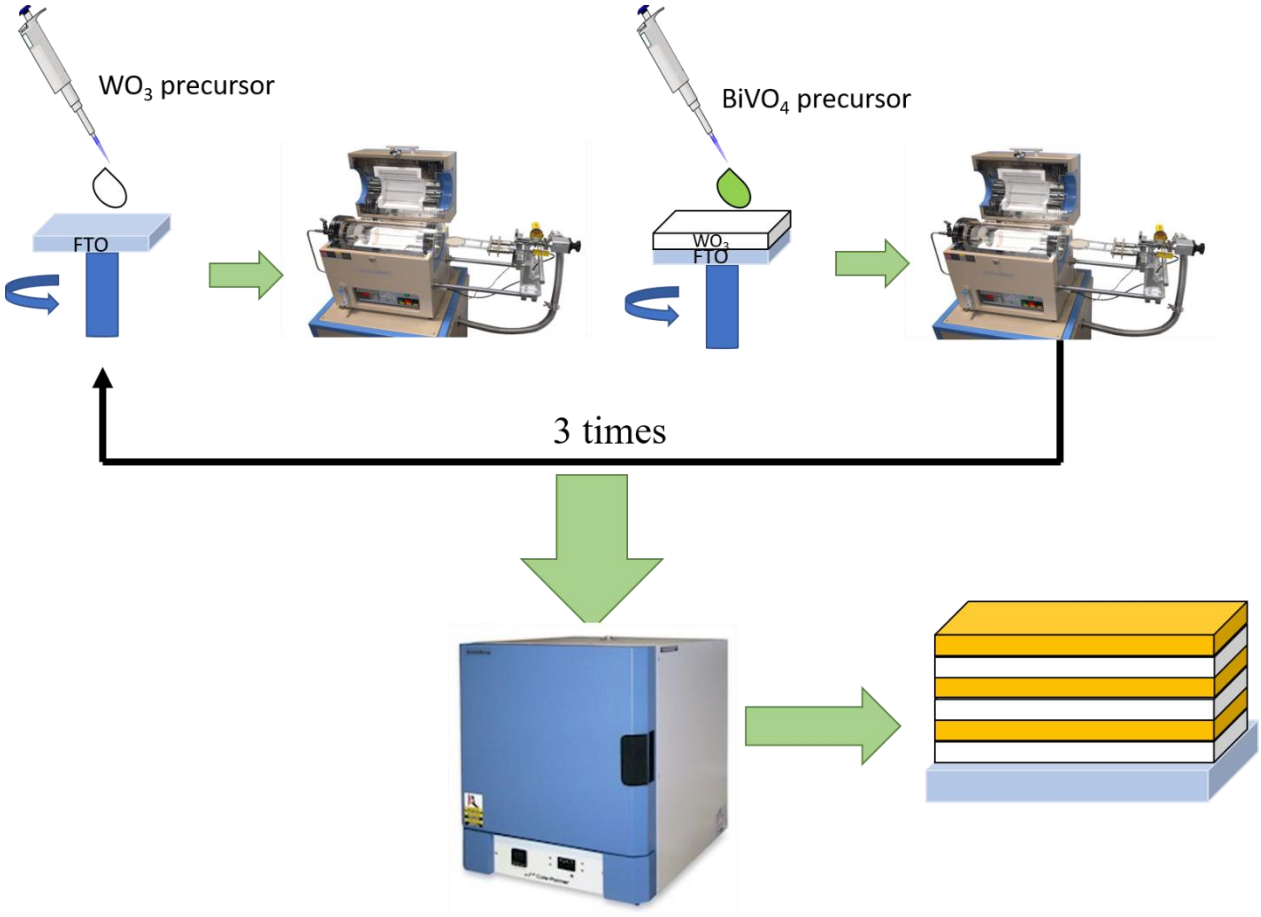

Figure IV. 4. Sandwich structures synthesized of WO_3-$BiVO_4$ by spin coating method. The white rectangles correspond to WO_3 deposited by spin coating, the yellow corresponds to spin coated $BiVO_4$ layer.

IV.1.5. Sn-doped iron oxide

Synthesis, structural and DC photoelectrochemical characterization of films were held in the Clean Energy and Nanotechnology (CLEAN) Laboratory, Joint Laboratory for Energy and Environmental Catalysis, School of Energy and Environment, City University of Hong Kong while the IMPS measurements were performed in CINVESTAV Mérida.

Iron foil (Alfa Aesar, 0.1 mm thickness, 99.99% metal basis, cut into 1 cm × 1cm size) were cleaned by sequential sonication in water, ethanol, and acetone for 20 min each and then dried under flowing N_2. Anodization of Fe foil was carried out in a two-electrode system with iron foil as the anode and platinum foil as the counter electrode. The electrolyte consisted of predetermined amount of SnF_2 (99%, Aldrich) dissolved in 3% deionized water (18.2 MΩ, Millipore) / 97% ethylene glycol (99.8%, Aldrich). The anodization voltage was modulated in a continuous negative-to-positive square wave pattern at 100 Hz using the Solartron Modulab potentiostat equipped with high voltage and current booster modules. The as-prepared samples were rinsed with deionized water and annealed in a muffle furnace (Thermo). Samples were annealed at the predetermined temperature (ramping 3 $^{o}C\ min^{-1}$) for 1 h. figure IV.5. summarizes the anodization process.

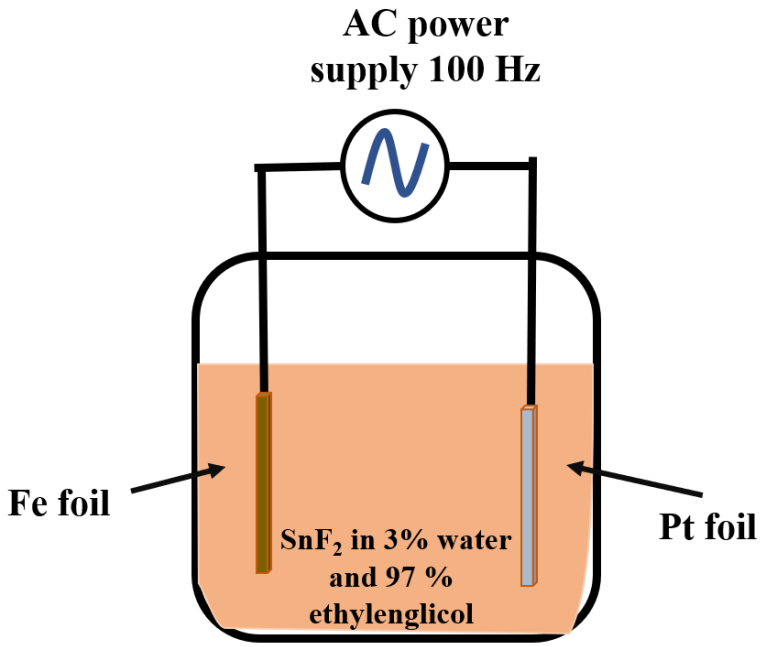

Figure IV. 5. Electrochemical cell used for anodization process of Fe foil to obtain Fe_2O_3 films.

Co-Pi cocatalyst was deposited onto the iron oxide substrate by immersing in 0.1 M potassium phosphate buffer (pH 7) containing 0.5 mM $CoCl_2$ (98%, Aldrich). Potential bias of +0.38 V vs Ag/AgCl was applied whilst irradiating with a 300 W Xenon lamp (Newport) at 100 mW cm^{-2} intensity.

IV.2. Characterization techniques

IV.2.1. X-ray diffraction (XRD)

Grazing XRD measurements were performed using a grazing angle of 0.5° between the X-ray. A Siemens D-5000 diffractometer (Cu-Kα radiation, λ = 1.5418 Å) at 34 kV and 25 mA was used to obtain the XRD patterns for $CuBi_2O_4$ and WO_3 samples. For $CuWO_4$ and $BiVO_4/WO_3$ films, a X'pert PRO diffractometer (PANalytical, Cu Kα irradiation) was used to determine the crystal structure.

To analyze the measured diffractograms, reference files from the Joint Committee on Powder Diffraction Standards (JCPDS-NBS) were used to identify the crystal structure of the samples.

IV.2.2. Scanning electron microscopy (SEM)

SEM measurements were carried out using a scanning electron microscope (JEOL JSM-7600F) operated at an accelerating voltage of 10 kV and using the lower secondary electron image (LEI) and upper secondary electron image (SEI) as image mode.

IV.2.3. Uv-Vis spectroscopy

To determine the optical absorption of the samples, UV-Vis measurements were performed with an UV−Vis Agilent Cary 5000 spectrometer with a integrate sphere and using $BaSO_4$ as reference for $CuWO_4$ and $BiVO_4/WO_3$ films. The transmission measurements were performed in a wavelength region between 300 – 900 nm. In case of $CuBi_2O_4$ and WO_3 films, the spectra were obtained using an Ocean Optics (USB 2000) fiber optics spectrophotometer adapted with an integration sphere in the same range.

IV.2.4. Photoelectrochemical measurements

Current - potential curves and intensity-modulated photocurrent spectroscopy measurements were carried out with an Autolab PGSTAT302N/FRA2 set-up (Metrohm Autolab). A 400 W ozone-free Xe arc lamp (Newport 66921) with an AM 1.5G and a water filter was employed as

simulated sunlight. The light intensity was adjusted to 100 mW cm^{-2} using a calibrated silicon solar cell with incorporated KG-5 filter. The geometric area exposed was 0.8 cm^2 and the measurements were performed using different electrolyte solution for each sample in order to improve stability and photoresponse. In case of FeOx samples de geometric area was 0.13 cm^2. The cell configuration consisted of a single compartment cell adapted with a quartz window, using the three-electrode configuration: the synthesized film as working electrode, a Ag/AgCl/NaCl (3 M) as reference electrode and a platinum wire as counter electrode (figure IV.6). Electrochemical potentials were converted to the reversible hydrogen electrode (V vs RHE) scale.

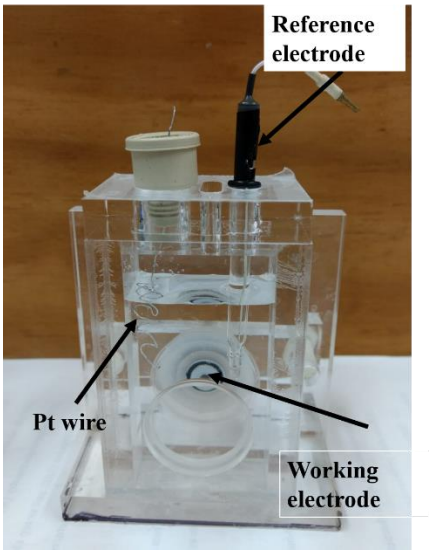

Figure IV. 6. Electrochemical cell used for photoelectrochemical measurements. The cell consists in a three electrodes configuration using a Pt wire as counter-electrode, the synthesized films as working electrode and a Ag/AgCl electrode as reference electrode.

IV.2.5. IMPS

IMPS measurements were performed in the frequency range from 20,000 Hz to 0.02 Hz, using a sinusoidal intensity modulation and bias illumination from a 455 nm high intensity blue LED. The amplitude of the sinusoidal modulation was about 25% of the base light intensity, and the linearity of the response was tested and confirmed using Lissajous plots. Normalization was performed by determining the number density of incident photons with a calibrated silicon photodiode, assuming that the LED used is monochromatic at the maximum wavelength, followed by a calculation of the corresponding maximum photocurrent if each irradiated photon

generates one electron-hole pair. To relate the amplitude of the light modulation to the modulated photocurrent, the zero-frequency limit intercept with the real axis of the EQE was taken to be equal to the DC value for the EQE observed for the potential at which the experiments were performed.

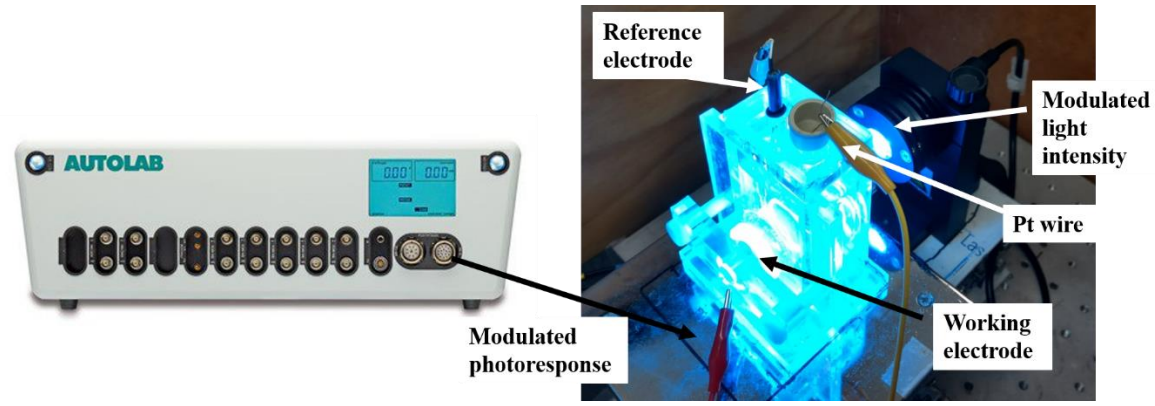

Figure IV. 7. IMPS experimental set-up.

Chapter V

V. Results and discussions

Semiconductors materials are the main key for a successful PEC cell. The performance of the photoanode and photocathode into the system determinates the STH efficiency. Despite some semiconductors have been widely studied and some important parameters have been determined, the understanding of the main processes at semiconductor/electrolyte interface and in the bulk are not completely defined. In this chapter, the synthesis and characterization of one photocathode ($CuBi_2O_4$) and 4 different photoanodes (WO_3, $CuWO_4$, $WO_3/BiVO_4$ and α-Fe_2O_3) have been exposed. The influence of some parameters on charge transfer processes at the surface will also be discussed.

V.1. Study of the charge carrier dynamics on Copper-Bismuth Oxide ($CuBi_2O_4$) photocathodes.

A single-composition ink base was used for the deposition of $CuBi_2O_4$ films onto FTO using the DIMATIX printer using different drop spacing to control the amount of material deposited. The morphology of the $CuBi_2O_4$ film at sintering temperature of 650 ºC was evaluated. Figure V.1 shows the XRD pattern for drop spacing (DS) of 10. The diffractogram corresponds to the reference pattern for $CuBi_2O_4$ (JCPDS #42-0334); the peaks at 26.7° and 51.76° are related to FTO.

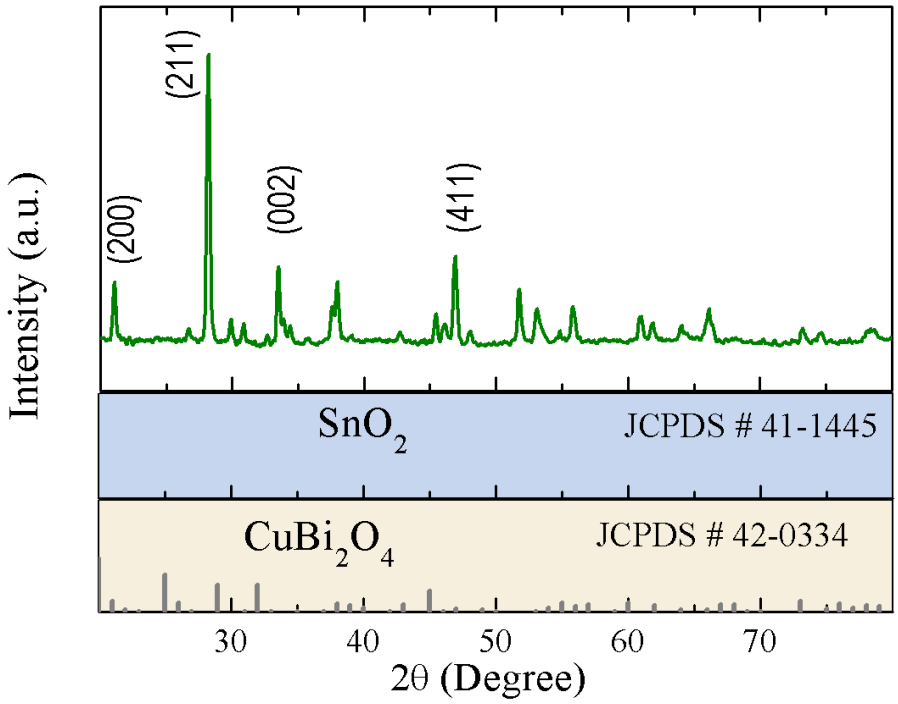

Figure V. 1. XRD diffractogram for the films deposited onto FTO by inkjet printing at 15 V, 5 kHz and 10 DS and subsequent sintering at 650 ºC on FTO.

In agreement with previous reports, the visual color of the films are light brownish.[68] In all the different DS, the SEM images illustrated in figure V.2 show porous films where part of the FTO are not covered. It is also observed that films are polycrystalline and there is an inverse relationship between the film thickness and the DS, the thickness can be somewhat modified by the drop spacing: for smaller DS the film thickness increases, maintaining the same general morphology. The grain size of each films is similar to the thickness.

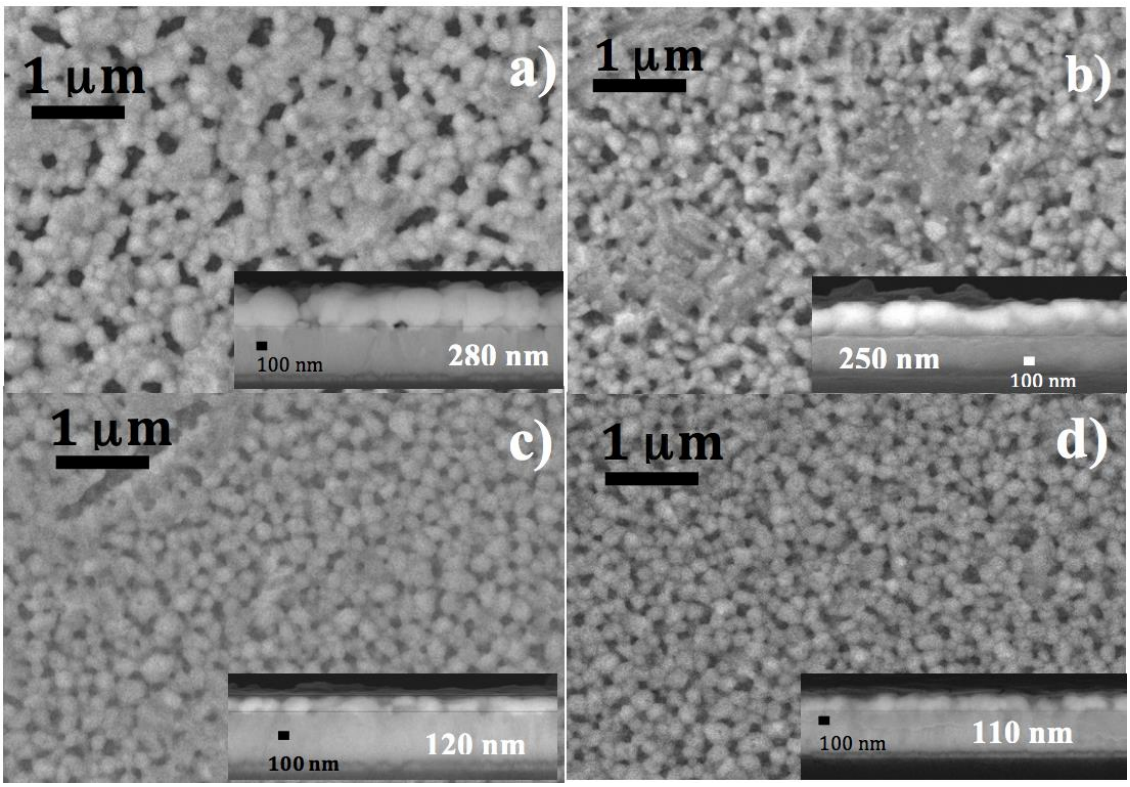

Figure V. 2. SEM top view images of a $CuBi_2O_4$ film deposited at different drop spacing: a) DS 10; b) DS 15; c) DS 20; d) DS 25. The insets correspond to the cross-sectional views and the $CuBi_2O_4$ film thickness is indicated; the thickness of the FTO film is 400 nm.

Figure V.3 shows the *I-V* curves under chopped illumination of the films synthesized by inkjet printing. For $CuBi_2O_4$ photocathodes, a 1 M $NaClO_4$ at pH 5 was used as electrolyte solution. The films exhibit an increase of the photocurrent density (*j*) in function of thickness increment. Interestingly, in the curve a cathodic current is observed at potentials below 0.8V (RHE)that is a typical p-type semiconductor behavior while an anodic current is observed at 1.2 V (RHE). Additionally, a spike is observed when the electrode is illuminated which is related to recombination. At potentials more negative than 0.2 V (vs. RHE), the cathodic current increases, both in the dark and under illumination, which is likely due to a reaction at the exposed FTO surface related to the porosity of the $CuBi_2O_4$ film. It is important to mention that the reduction of copper centers in the $CuBi_2O_4$ may occur, which has been reported previously and has been related to a limited stability against reduction.[56,68] A maximum value of approximately 0.15 mA cm^{-2} for a 280 nm $CuBi_2O_4$ film it is observed. The theoretical maximum photocurrent density calculated for $CuBi_2O_4$,

considering 100% absorption of the AM 1.5 spectrum for $E > 1.8$ eV is about 20 mA/cm^2.[65] To understand the reason why the photocurrent is much lower than theoretical value, an analysis of external quantum efficiency (EQE) is needed.

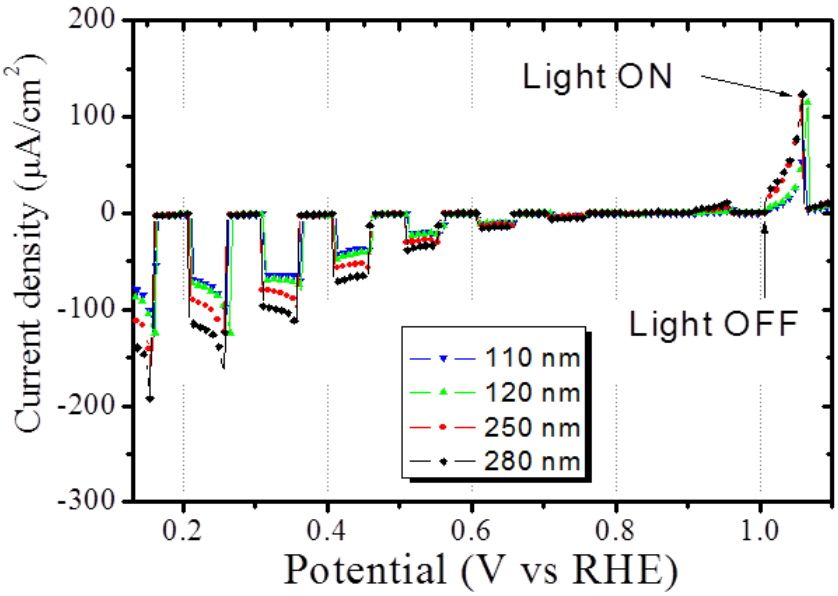

Figure V. 3. Current - potential curves for $CuBi_2O_4$ films as a function of film thickness by deposition at different drop spacing. The scan was performed from positive to negative potential. The measurements were performed at 1 sun in 1 M $NaClO_4$ at pH 5.

Figure V.4 shows the absorbance and the *EQE* as a function of wavelength for a 280 nm inkjet-printed $CuBi_2O_4$ film on FTO/glass. The absorbance spectrum shows an onset at about 800 nm (1.55 eV), whereas the absorbance increases strongly again at higher energies, with an onset at about 600 nm (2.06 eV). These results are in agreement with previous reports, where it has been shown that the electronic absorption spectrum of $CuBi_2O_4$ embodies two main features at different wavelengths. As it was mentioned before, the optical edge at lower energy is typically found between 1.5 to 1.85 eV[65,68,166], which according to theoretical quantum calculations is essentially related with transitions from the valence band (VB) into a band with a high contribution from Cu 3d orbitals[68]. The change in the absorbance profile at higher energy (> 2.0 eV) may be correlated with transitions from the VB into a band with marked character of Bi 3p states. Both bands are schematically represented by the highlighted Gaussian curves drawn below the absorbance curve. The absorbance spectrum can be used to determine the light harvesting efficiency

(*LHE*) as a function of wavelength, within the assumption that absorption is equal to absorbance, *A*, using $LHE = 1 - 10^{-A}$.[120]

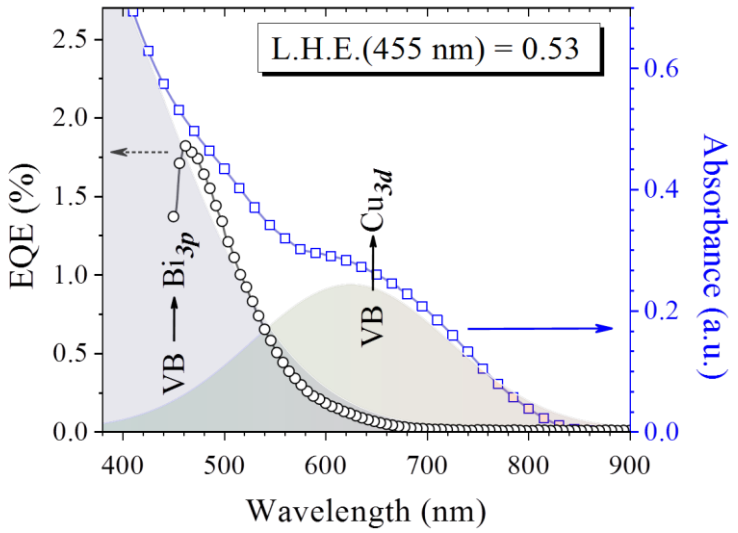

Figure V. 4. Absorbance and *EQE* (external quantum efficiency) versus illumination wavelength for $CuBi_2O_4$ photocathodes with a film thickness of 280 nm. The *EQE* was measured at 0.6 V(RHE) in a 0.1 M Na_2SO_4 solution (pH = 5.7). The value for the *LHE* represents the average of 5 films.

From the *EQE* curve, charge collection starts to be effective only at wavelengths below 680 nm (E > 1.8 eV), suggesting that the lower energy optical transitions do not lead to efficient charge separation. The effective bandgap for charge collection is about 2.0 eV for the inkjet-printed $CuBi_2O_4$ material. The EQE reaches a maximum of around 1.8% at about 460 nm, indicating that the collection efficiency of the $CuBi_2O_4$ photocathodes is in general rather low. Combined with the observation that the light harvesting efficiency (*LHE*) is about 0.53, this implies that only 3.3% of the generated electron (CB) – hole (VB) pairs result in a current in the external circuit at this potential.

Steady-state experiments of the *EQE* and current – potential curves provide only limited information on the reason for the low external efficiency, and measurements in the frequency domain can be very helpful to distinguish between various loss processes, such as recombination in the bulk and surface recombination, and can provide important clues on the charge transfer and collection efficiencies.

The external quantum efficiency can be considered as the product of the light harvesting efficiency and the charge collection efficiency; the latter depends on the charge separation efficiency, which in turn is determined by the electric field, and the balance between charge transport and extraction, both at the FTO and the solution interface, on the one hand and recombination on the other hand.[55,58,167,168] Electrochemical impedance spectroscopy was performed to characterize the electrodes, however, the interpretation of the results was not straightforward, related to the porosity of the film, and the n-type character of the FTO substrate as opposed to the primarily p-type character of $CuBi_2O_4$. An important advantage of IMPS is that only the photoactive material is probed, thus significantly simplifying the interpretation.

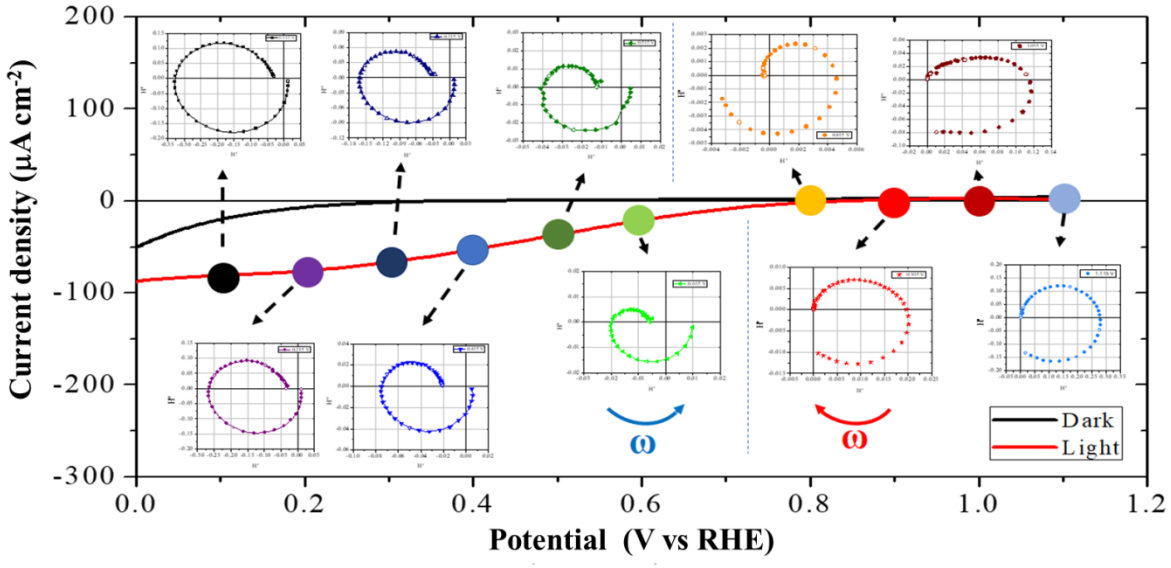

Figure V. 5. Steady-state current - potential curves in the dark and under blue LED illumination. The insets correspond to the IMPS spectra at each determined potential.

Figure V.5 shows the current density - potential (*I-V*) curve in the dark and under illumination of a 280 nm $CuBi_2O_4$ photoelectrode on FTO using a high power, blue LED (455 nm; 2.7 eV). The general aspects of the curves are the same as for white light illumination, however, the LED allows us to modulate the light intensity and determine the IMPS response using an LED driver. The insets of figure V.5 show the representative IMPS spectra for the potentials indicated in the curve. The *I-V* curve and IMPS spectra can be divided in three regions: (i) potentials more negative than 0.75 V(RHE), where the cathodic photocurrent corresponds to the reduction of water; (ii) the potential range

between 0.75 V and 1.15 V(RHE), where no steady-state photocurrent is observed; and (iii) potentials more positive than 1.15 V(RHE). The IMPS spectra measured at potentials between 0.1 and 1.15 V(RHE) are observed in figure V.6.

For V>0.75V RHE, at high frequencies (> 10 kHz), the data points are close to the origin, and upon decreasing the frequency, a semicircle in the third quadrant is observed. At intermediate frequencies, the data points correspond to a negative real value for *H*, with the imaginary part being negligible, which gives the external charge collection efficiency (*ECCE*) in the absence of recombination and charge transfer. At lower frequencies, a second semicircle develops, eventually reaching again a negative real value, which depends on the applied potential. In figure V.6b shows that upon applying more negative potentials in region (i), the intercept for $\omega \rightarrow 0$ moves away from the origin indicating the onset of a DC photocurrent, which coincides with the observations in the steady-state *I-V* curve. At potentials more negative than 0.4 V(RHE), the medium frequency crossing point with the real axis increases, indicating that the charge separation efficiency (*CSE*) is increasing with more negative potential; however, the low frequency intercept does not increase much correlating with an essentially constant steady-state photocurrent. This may be due to two different situations: (i) surface recombination becomes faster, or (ii) electron transfer to the solution becomes slower. In order to distinguish between these two mechanisms, the results need to be analyzed in more detail, which will be discussed below.

On the other hand, at potentials between 0.75 V and 1.15 V(RHE), as it is observed in figure V.5, the steady state photocurrent density is close to zero, however, the IMPS spectra indicate that charge carrier generation and separation can be achieved, but that surface recombination prevents a steady-state photocurrent to be observed. In this potential range, a very interesting observation is apparent: the collection loop moves to the fourth quadrant, instead of the third quadrant, and the recombination / charge transfer loop is observed in the first quadrant, instead of the second. These results are characteristic of an n-type semiconductor, where the minority carrier flux corresponds to holes in the valence band, and the (modulated) photocurrent is positive corresponding to water oxidation. Hence, it appears that $CuBi_2O_4$ is either an almost intrinsic semiconductor with a low acceptor density or a compensated semiconductor, where both cathodic and anodic photocurrents are

possible, depending on the applied potential, the light intensity, and, undoubtedly, the synthesis method.[169] However, it is observed that in the entire potential range between 0.75 V and 1.15 V(RHE), the intercept at for $\omega \rightarrow 0$ is in the origin, which illustrates that surface recombination wins over hole transfer to the solution; hence, a steady-state oxidation photocurrent is not observed, in agreement with the *I-V* curve, indicating the slow transfer kinetics for the water oxidation reaction.

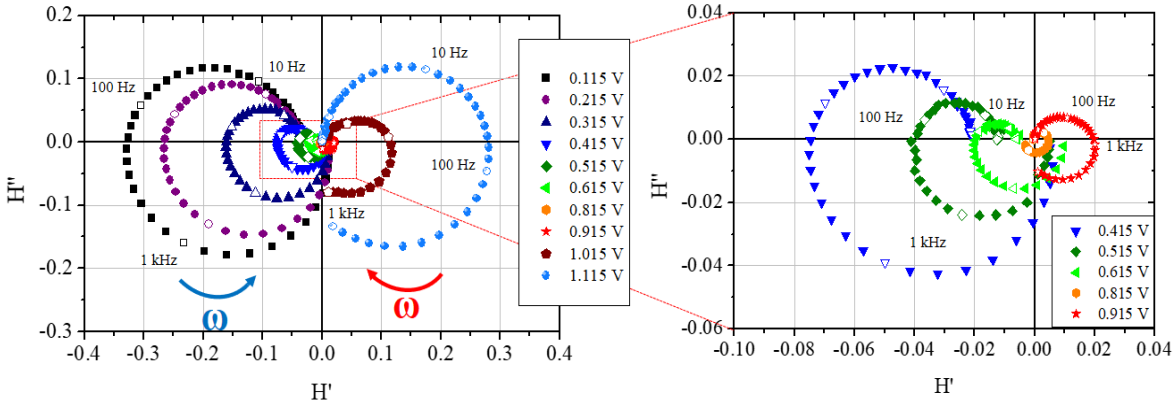

Figure V. 6 On left IMPS spectra obtained at potentials 0.115-1.115 (V vs. RHE). On right, zoom of the IMPS spectra for the potential range from 0.415 - 0.915 V(RHE)). The measurements were performed in a 1 M $NaClO_4$ solution at pH 5.

In classical semiconductor electrochemistry, the energetic position of the valence and conduction band edges at the interface are independent of the applied potential, and the potential dependence of the charge carrier density at the surface determines the corresponding reaction rates. Figure V.7a shows the rate constants versus applied potential obtained from fitting the results shown in figure V.6. It can be observed that both the RC time constant and the recombination rate constant are essentially independent of applied potential for V < 0.75 V(RHE), in agreement with expectations. On the other hand, the charge transfer rate constant is constant between 0.75 and 0.40 V(RHE) but decreases somewhat at more negative potentials. In addition, at V > 0.75 V(RHE), the rate constant decreases significantly, can be related to the change in process from a cathodic to an anodic reaction. Hence, the water oxidation rate constant is significantly smaller that for water reduction. An important result is that the recombination rate constant is found to be larger than the charge transfer rate constant in the entire potential range, indicating that the relative charge transfer efficiency is much lower than 1 in the entire potential range.

Figure V.7b shows the relative charge transfer efficiency as a function of applied potential, and the highest efficiency is close to 0.4 in the potential range between 0.45 V and 0.75 V(RHE). At more positive potential the relative transfer efficiency goes to 0 while at more negative potentials, the relative transfer efficiency decreases to about 0.2, which is an interesting phenomenon. This observation is correlated with an increase in the dark current of the photoelectrode, as well as a decrease in stability. In general, it was found that the material is not stable at potentials more negative than about 0.2 V(RHE), which is most likely related to reduction of copper centers in the $CuBi_2O_4$ material, in agreement with previous reports.[56,68,55] Hence, the decrease in transfer efficiency may be related to a change in surface chemistry, via a decrease of the charge transfer rate constant at potentials more negative than $V < 0.40$ V(RHE).

Figure V.7c shows the potential dependence of the medium frequency intercept on the *Re(H)* axis, i.e. the maximum attainable product of *CSE* and *LHE* in the absence of recombination, and the low frequency intercept corresponding to the small-signal value of the steady-state *EQE*. The maximum low frequency intercept is about 0.035 at 0.2 V(RHE) and these results are in good agreement with the *EQE* measurements in figure V.4. The low frequency curve mimics the steady-state *I-V* curve.

The medium frequency crossing point increases with more negative potential, approaching a value of 0.35 at 0 V(RHE); as it was mentioned in chapter 2, the negative sign in the graph indicates that this is a photoreduction process, as opposed to a photooxidation process. Hence, assuming that the light harvesting efficiency is independent of applied potential, charge separation becomes more efficient at more negative potential, suggesting that the band bending increases as expected. The charge separation efficiency can be determined from the intercept by dividing by the *LHE* of 0.53, resulting in *CSE* = 0.66. Hence, per absorbed photon, 0.66 electron-hole pairs are successfully separated across the space charge layer at 0 V(RHE). This indicates that about a third of the generated pairs is lost by bulk recombination. On the other hand, the relative charge transfer efficiency at 0 V(RHE) is 0.2, hence, 80% of successfully separated electron-hole pairs are lost via surface recombination. In fact, the relative charge transfer efficiency is optimal in the potential range where the charge separation efficiency is still low; the combination of both effects

explains the photocurrent potential curve. In general, it can be concluded that, although photoreduction of water is achieved, the efficiency needs to be improved by either slowing down recombination, speeding up electron transfer, or improving the charge separation efficiency at more positive potentials.

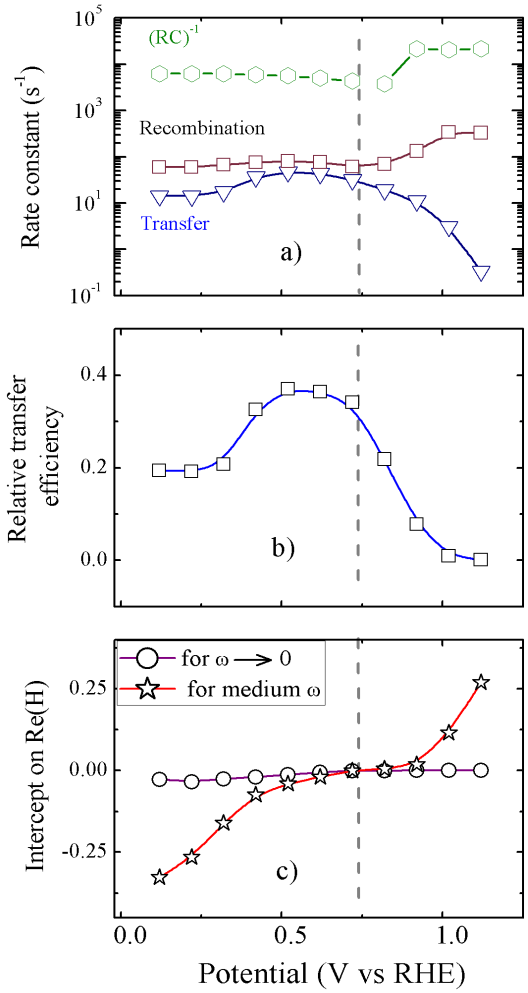

Figure V. 7. Applied potential dependence of: (a) electron transfer rate constant (k_{tr}), surface recombination rate constant (k_{rec}), and cell constant; (b) relative transfer efficiency; and (c) intercept on *Re(H)* axis, corresponding to the product of *CSE* and *LHE* at medium frequency, and the small-signal external quantum efficiency for the frequency limit to zero, respectively.

Measurements as a function of the light intensity can give information of the effect of charge density and trapping on the respective rate constants. The charge transfer and recombination rate constants are in principle expected to be independent of light intensity,

however, charge trapping may affect the reaction rates as well as the charge transport kinetics. Figure V.8 illustrates that the photocurrent is dependent on the light intensity, although not linearly: at lower intensities, the photocurrent is surprisingly high, suggesting that the *EQE* depends on light intensity.

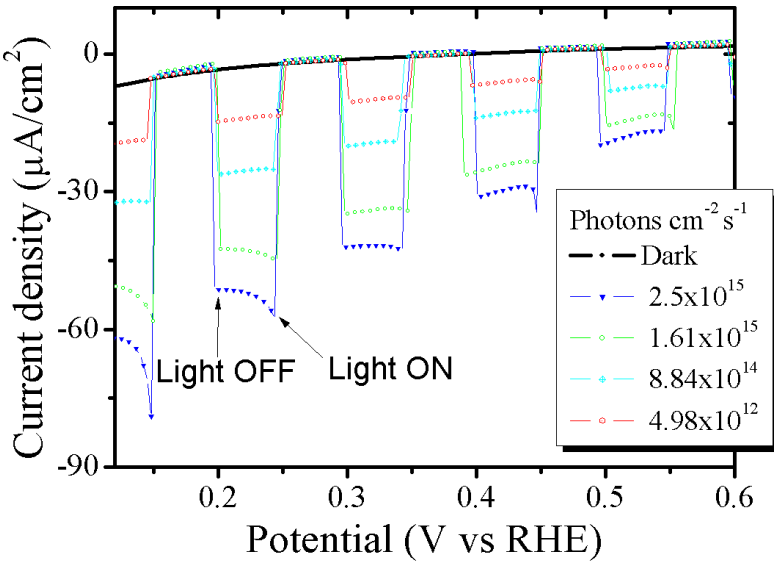

Figure V. 8. Current - potential curves for a 280 nm $CuBi_2O_4$ photoelectrode as a function of the incident light intensity. The scan was performed from positive to negative potential, in 1 M $NaClO_4$ at pH 5.

IMPS measurements by varying light intensity (figure V.9) show that, beside *CSE* is higher when the number of irradiated photons is higher, the recombination/transfer loop become smaller when light intensity decreases. Additionally, the intercept at lower frequencies stay away from zero suggesting again that the rate constants are not independent of light intensity.

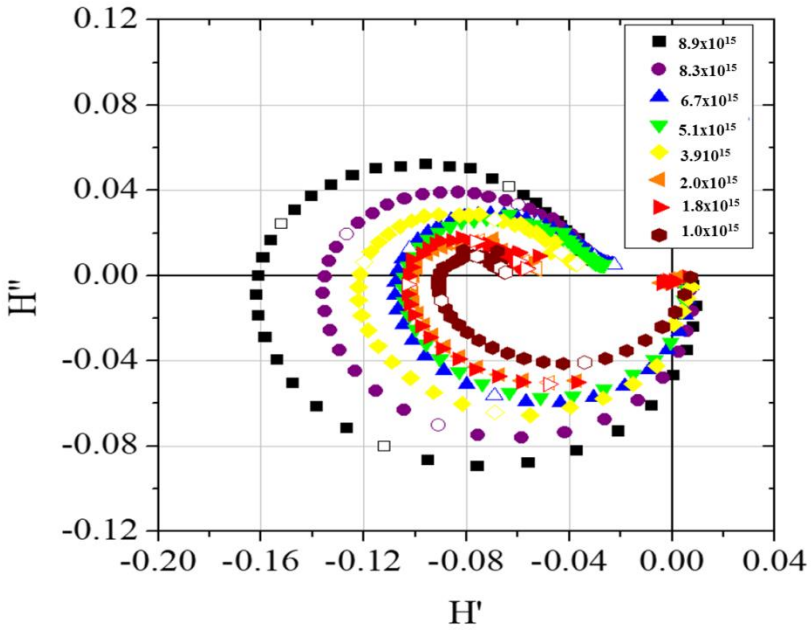

Figure V. 9. IMPS measurements as a function of light intensity. The analysis was performed at an applied potential of 0.32 V(RHE).

In Figure V.10, the charge transfer and recombination rate constants are shown as a function of illumination intensity. In addition, it can be seen that the *RC* time constant is slightly dependent on the light intensity suggesting that charge trapping occurs, which may result in a slight decrease of the resistance with increasing charge density.

The results shown in Figure V.10 are obtained in the region where water reduction occurs and, under these conditions, photogenerated electrons are trapped at the surface due to the very slow transfer kinetics. This may result in the reduction of surface species, which could lead to a higher trap density. In turn, surface traps can facilitate recombination, thus resulting in an increase in recombination rate constant with higher light intensity. On the other hand, it is found that the electron transfer rate constant decreases with increasing light intensity, suggesting that a higher trapped electron density at the surface results in slower electron transfer, which is in accordance with the observations as a function of applied potential in figures V.10a and b. These results indicate that the change of surface chemistry is essential in determining both the electron transfer and surface recombination rate constants. Figure V.10a shows that the relative charge transfer efficiency increases significantly with decreasing light intensity: at intensities smaller than about a photon flux equivalent to 0.1 sun, the relative transfer efficiency is as high as 0.80, illustrating that high

efficiencies could be achieved for this material. In order to achieve these high efficiencies, it is necessary to avoid charge trapping at the surface, thus optimizing the kinetics of electron transfer to the solution and decreasing the surface recombination rate.

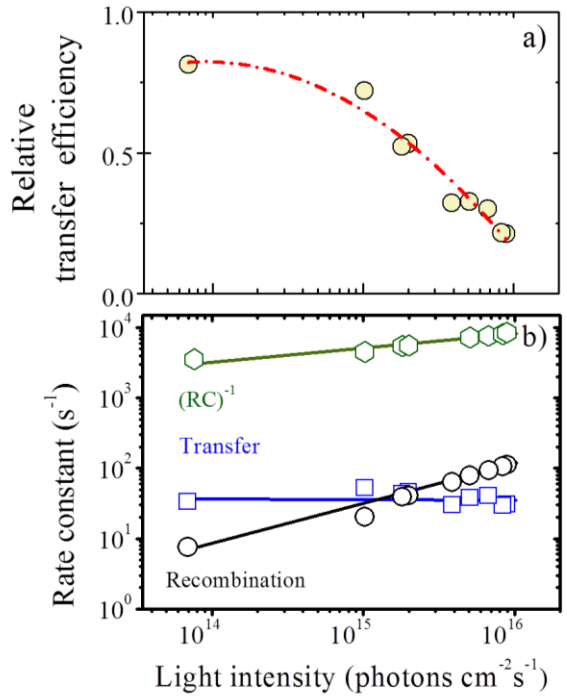

Figure V. 10. Light intensity dependence of: (a) the relative transfer efficiency; and (b) the electron transfer and surface recombination rate constants and $(RC)^{-1}$. The analysis was performed at an applied potential of 0.32 V(RHE).

Conclusions

We have prepared polycrystalline $CuBi_2O_4$ photoelectrodes by a simple inkjet printing technique of a film thickness between 100 nm and 280 nm, with an effective band gap of about 2.0 eV. The material acts mainly as a p-type semiconductor and a cathodic photocurrent corresponding to water reduction is observed at potentials negative of about 0.8 V(RHE), however, an anodic photocurrent can also be obtained at potentials sufficiently positive, illustrating the unique properties of this material. The charge transfer and recombination dynamics have been analyzed in detail using intensity-modulated photocurrent spectroscopy, and it is shown that an unfavorable balance of the rate constants

for charge transfer and recombination limits the efficiency of the photoelectrode. In particular, the relative electron transfer efficiency is about 0.2 in the potential range where a photocurrent plateau is observed: this is due to interfacial reduction of the oxide material, which needs to be prevented in order to increase the external quantum efficiency. The relative charge transfer efficiency is significantly larger at lower light intensity, illustrating the promise of p-type $CuBi_2O_4$.

V.2. Charge transfer and recombination kinetics at WO_3 photoanode's surface.

Figure V.11a and b shows the XRD patterns of the starting material tungstic acid, which has an orthorhombic crystal structure, and the well-crystallized WO_3 with a monoclinic crystal structure (JCPDS # 43-1035) after thermal treatment at 550 °C. The temperature was determined according to previous report.[164] The SEM image in figure V.11c, show the morphology of WO_3 films after sintering in which the presence of a wide distribution size of particle between 50-500 nm can be observed, the inset in this image displayed the profile of the film where it is observed a uniform layer for the thinner films. Diffuse reflectance spectra on WO_3 film is shown in figure V.11d, in this plot we can observe an electronic band absorption from 250 to 450 nm which is characteristic for WO_3 material, with a band gap of 2.6 eV.

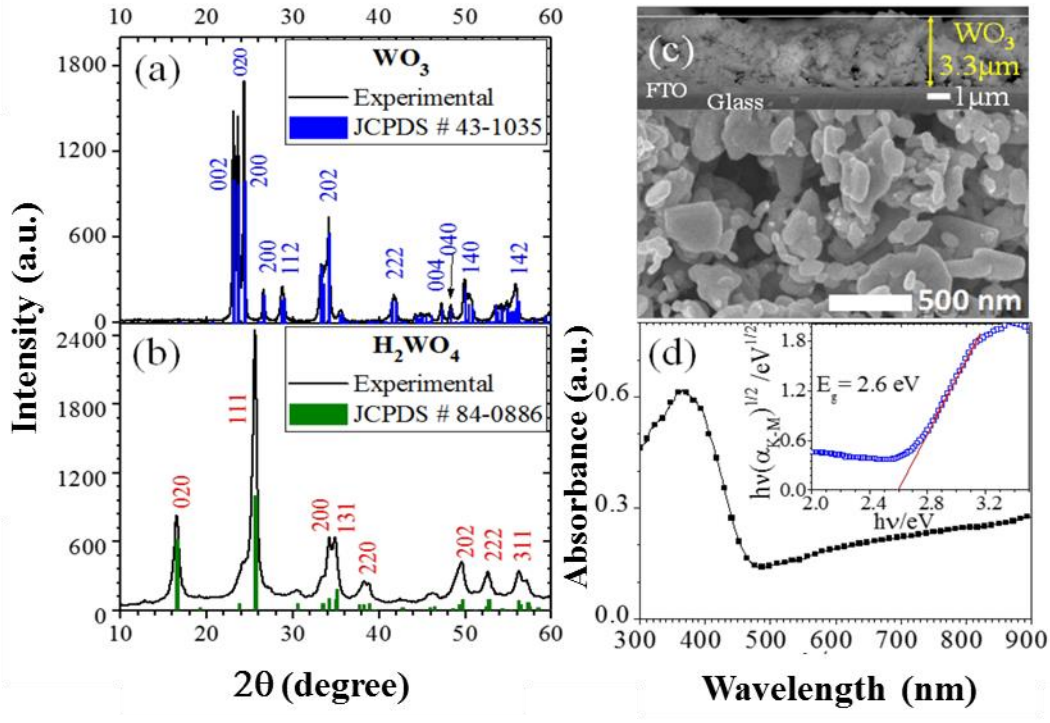

Figure V. 11. X-ray diffraction patterns of the phase-pure a) WO_3, b) H_2WO_4, c) SEM micrograph of WO_3 porous film of 3.3 microns, the inset show the uniform deposit. d) Absorbance spectrum of WO_3 film, the inset corresponds to the Tauc plot.

Figure V.12 shows the cyclic voltammetry curves including the forward and reverse scan for WO_3 electrodes with different film thickness under front and back side illumination. Under dark conditions a sharp increase in anodic current is observed at potentials around 2.0 V (RHE) related to water oxidation and a small cathodic current is observed at potentials at 0.3 V (RHE) which is related to the reduction of WO_3, due to the presence of W^{5+} or W^{6+} bronzes, [164,170–172] and water reduction. The onset potentials for the anodic and cathodic dark current were independent of the film thickness; for films thicker than 10 μm, a larger charging current was observed, indicating the effect of charge storage on the film.

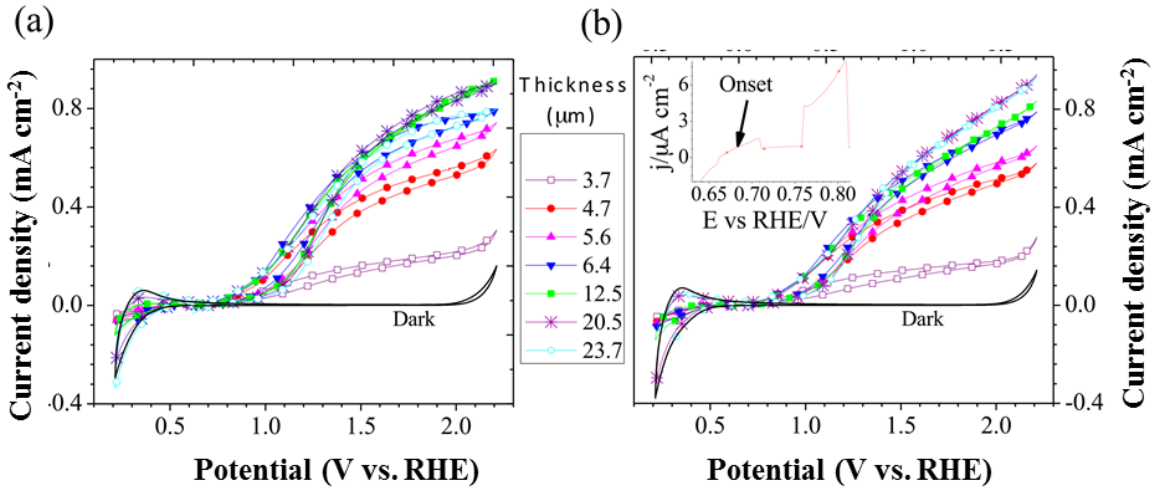

Figure V. 12. Cyclic voltammetry results of WO_3 electrodes of different thickness under (a) front and (b) back side illumination. The inset in (b) show the onset potential obtained for the film optimal thickness from chopped light measurements. All the experiments were performed in 1 M $NaClO_4$ adjusted to pH 5 as electrolyte solution, with a 5 mV/s scan rate and under 1 sun simulated solar illumination.

Figures V.12a and V.12b illustrate different electrochemical behavior under front and back side illuminations: under front side illumination, a plateau is observed at potentials more positive than 1.8 V (RHE). Under back side illumination a more pronounced photocurrent dependence on film thickness was observed that increased with more positive applied potential. Under front side illumination (figure V.12a) the anodic photocurrent showed a linear increase for film thicknesses below 12.5 μm with a maximum photocurrent of 0.8 mA/cm^2 at 2.0 V (RHE). Under backside illumination (figure V.12b), the current density

increases as a function of the film thickness with a maximum photocurrent of 0.81 mA/cm^2 at 2.0 V (RHE) in the film of 20.5 µm.

In order to gain a deeper understanding in the charge separation and collection from WO_3 films under illumination, IMPS measurements were employed. Electrodes with 4.3 µm film thickness were chosen as a model system, and the effect of film thickness was determined.

IMPS as a function of applied potential. Although for classical single-crystal semiconductors, the charge transfer and recombination rates are determined by the potential dependence of charge carrier densities at the surface, while the respective rate constants are expected to remain unchanged, this situation is likely different for these complex, porous, nanocrystalline oxide semiconductor electrodes. In particular, if band edges shift due to oxidation or reduction of the surface, or if interfacial states are created due to a change in potential, the rate constants may depend on the applied potential and the light intensity.[157] Figure V.13 shows a representative current – potential curve under blue LED illumination, and IMPS plots are presented for selected potentials while a complete sets of IMPS plots are presented in figure V.14.

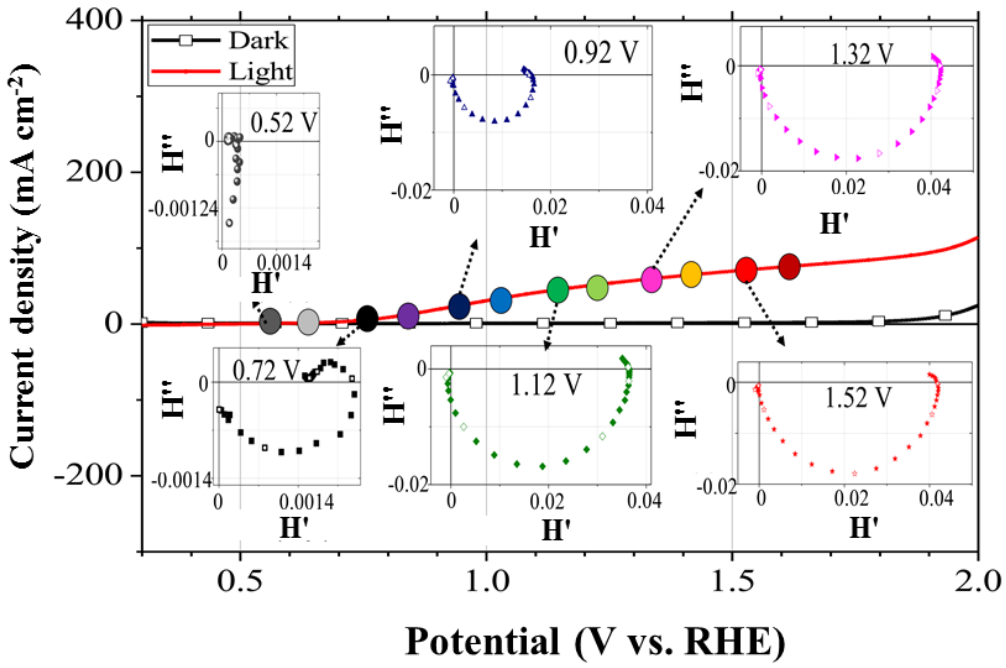

Figure V. 13. Current - voltage curve under light and dark conditions, with IMPS plots presented at selected potentials. These data were obtained for a WO_3 film of 4.3 µm thickness.

At potentials more negative than 0.7 V, the steady-state photocurrent is close to zero, which may imply that the photogenerated carriers recombine. At applied potentials more positive than 0.7 V, an onset of photocurrent related with a photo oxidation of water is observed.[137,156] This is reflected in the IMPS plot presented at 0.72 V (RHE), where the intercept with the real axis at low frequencies moves away from zero, indicating a steady-state photocurrent. A semicircle is observed in the first quadrant, related with the competition between recombination and charge transfer to the electrolyte solution.[137,156–158,161,162,173] If the recombination rate becomes smaller in comparison to the charge transfer rate to the electrolyte solution, this semicircle should decrease and, ultimately, disappear, as we can observe when the potential is shifted to more positive values.[137,156–158,161,162,173] At the same time, an increase in photocurrent is obtained at more positive potentials, associated with a decrease in the recombination semicircle in the first quadrant.

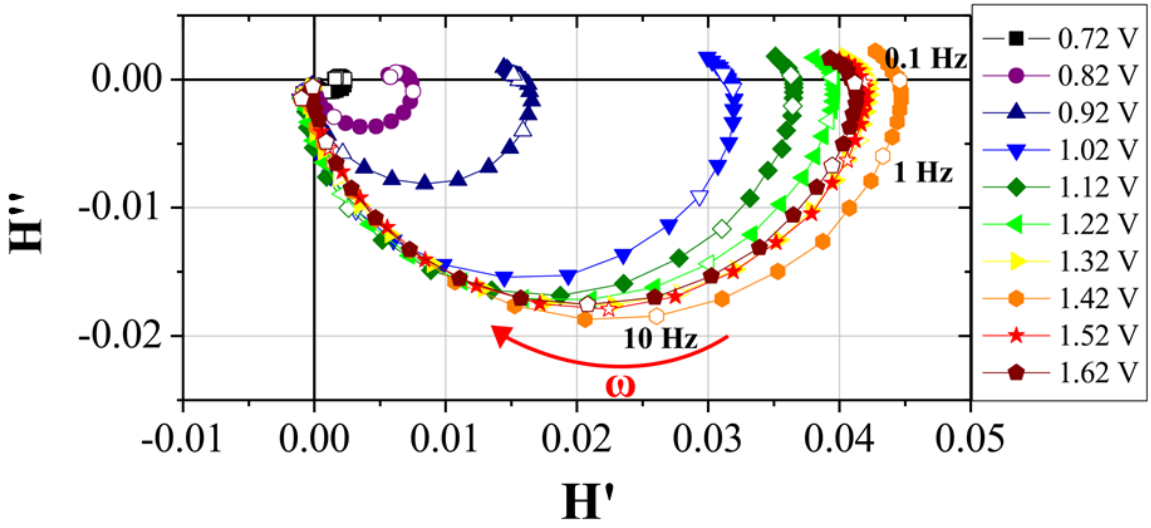

Figure V. 14. IMPS Nyquist plots obtained at different scan potentials (V vs RHE) with a 455 nm blue LED as the illumination source. The frequency was modulated from 20000 to 0.02 Hz.

The kinetic rate constants and the hole transfer efficiency to the electrolyte solution, obtained from the IMPS analysis at different potentials, are presented in figure V.15. According to figure V.15a, the recombination (K_{rec}) and charge transfer (k_{tr}) rate constants seems to depend in a very similar way with the applied potential. At more positive potentials, both charge transfer and recombination become slower, while at potentials closer to 0.7 V, both processes are faster. However, at potentials more positive than about

1.0 V, it is important to observe that the charge transfer rate constant to the electrolyte solution is significantly larger than the recombination rate constant, highlighting the potential of the material to work as an electrode on the water oxidation reaction. The sudden change of both rate constants in a very similar way between 0.8 – 1.0 V implies that a surface modification occurs, which significantly affects both processes. From the semicircle in the fourth quadrant, the RC time constant of the cell can be obtained, and in order to compare this with the rate constants for charge transfer and recombination, $1/\tau_{RC}$ is also shown in figure V.15a. It is clear that at potentials more positive than 1.0 V, the RC process is much faster than the charge carrier kinetics, which allows for an adequate determination of the respective rate constants, however, at potentials more negative than 0.8 V, the RC charging process is clearly at the same order of magnitude, which effectively makes it unreliable to determine the charge transfer and recombination rate constants at these potentials.

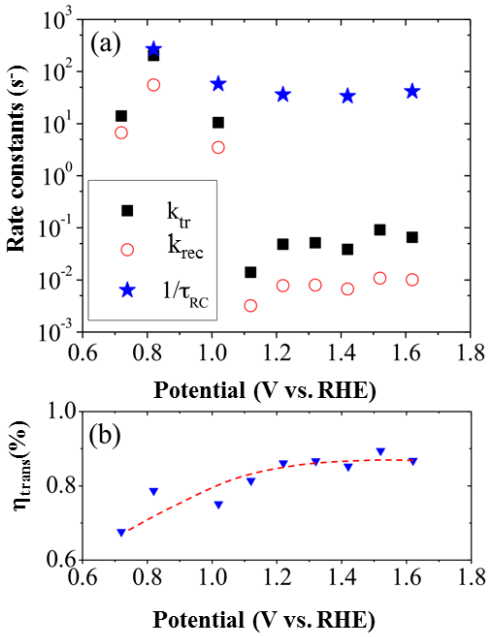

Figure V. 15. (a) Charge transfer rate constant (k_{tr}) and recombination rate constant (k_{rec}), as well as the $1/\tau_{RC}$ frequency cell constant as a function of the applied potential; (b) Relative transfer efficiency as a function of applied potential obtained from IMPS analysis.

Another way of understanding at this result is that charge transport through the WO_3 film and the corresponding charging of the surface limits the Faradaic charge transfer to the

solution, thus resulting in the strong decrease in current at these potentials. In spite of presenting relatively sluggish charge transfer to the electrolyte solution at potentials above 1.1 V, figure V.15b shows that the relative transfer efficiency to the electrolyte solution it is actually higher when increasing the applied potential. This is due to a suppression of the recombination reaction, implying that a higher percentage of the charge carriers collected at the semiconductor surface will transfer to the electrolyte solution, favoring an oxidation reaction at the semiconductor surface.

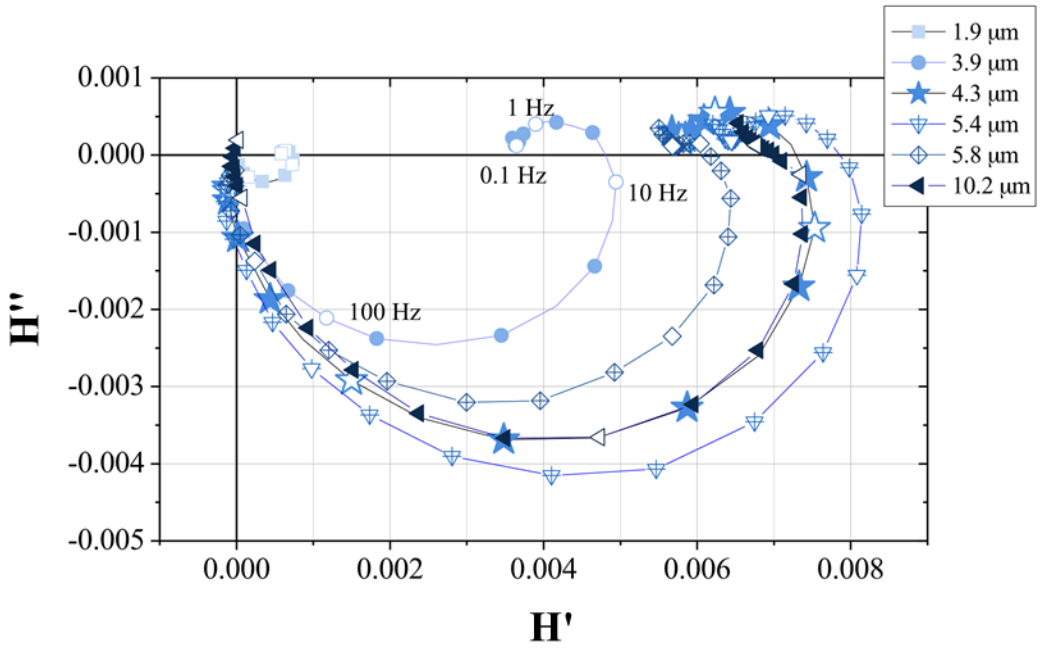

Figure V. 16. IMPS plots as a function of WO_3 film thickness. All the measurements were performed at 0.82 V.

IMPS as a function of film thickness. Figure V.16 shows the IMPS results for WO_3 electrodes as a function of film thickness. It is noticeable that the intercept with the real axis in the right upper quadrant at intermediate frequencies (around 10 Hz) occurs at higher values for thicker films, although there seems to be no significant difference once the thickness of the electrode is around 4 µm. This intercept is related with the flux of photogenerated carriers towards the surface of the semiconductor upon illumination.[137,156–158,161,162,173] When the electrode is made thicker, more photogenerated carriers can travel to the semiconductor surface, thus increasing the current. However, as discussed previously,

there is an optimum value for the film thickness, which is also observed with the IMPS measurements.

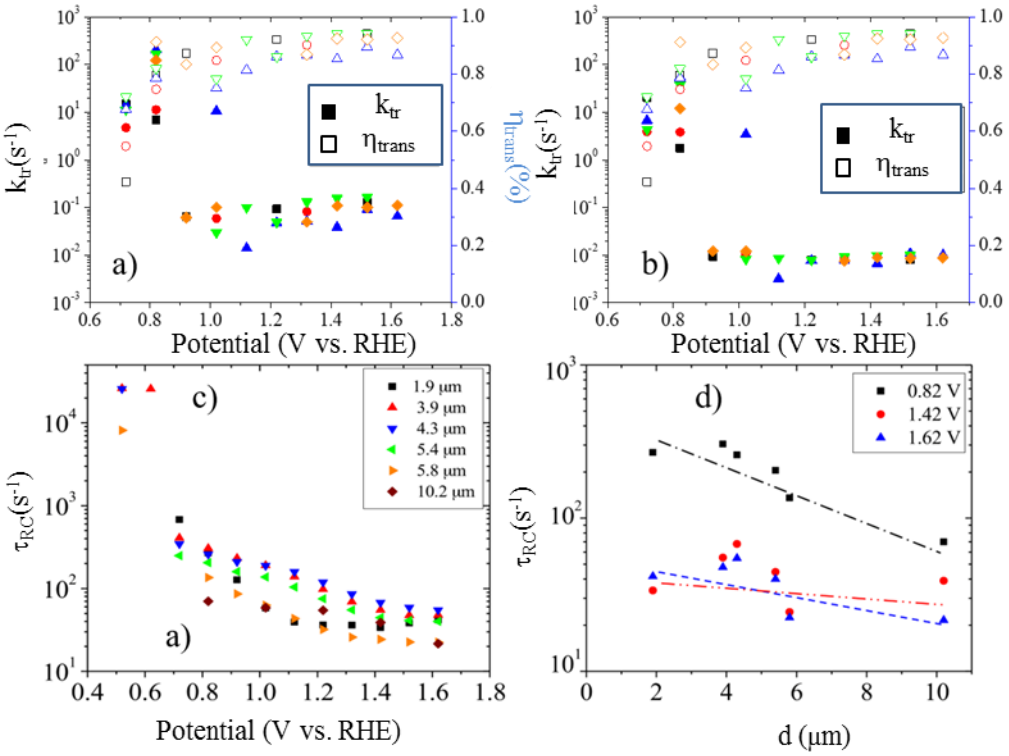

Figure V. 17. a) Charge transfer rate to the electrolyte solution; b) surface recombination rate as a function of the WO_3 thickness film and applied potential. The right side in each plot show the transfer efficiency as a function of WO_3 thickness and c)τ_{RC} as function of applied voltage. d) dependence of τ_{RC} film thickness.

The right lower quadrant is formed by the contribution of the total resistance of the cell, the space charge and the Helmholtz capacitance on the sample, i.e., the RC time.[174] Figure V.17a,b shows that the thickness of the WO_3 layer does not significantly influence the kinetics of charge transfer and recombination inside the system. The trend for both rate constants is consistent with the results reported in figure V.15, where both rate constants become slower for applied potentials above about 0.9 V. The right side on figure V.17a shows that the transfer efficiency of holes towards the electrolyte solution seems to be essentially independent of WO_3 thickness, and instead it depends mainly on the applied potential. However, there is a trend to an increase in RC time and, hence, a slowing down

of the transport and charging process with increasing thickness (figure V.17d), which may affect the onset potential of the photocurrent somewhat. In spite of having very similar rate constants and the implication that the thickness does not influence the kinetics of the system, the current - potential curves presented in figure V.12 clearly show that the photocurrent increases as the thickness of the WO_3 increases. This strongly suggests that the charge carrier driving force is also determined by light penetration and not only by kinetics; hence the ideal thickness of the photoelectrode is clearly related to the absorption coefficient of the semiconductor material.

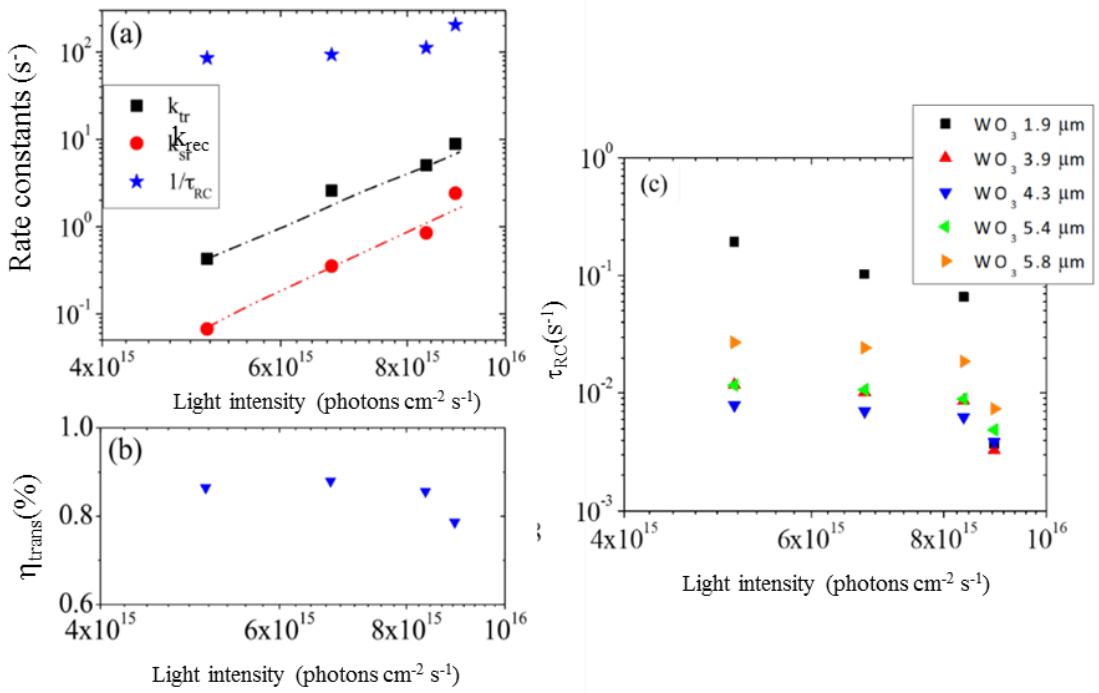

Figure V. 18. (a) Charge transfer rate constant (k_{tr}) and recombination rate constant (K_{rec}), as well as the $1/\tau_{RC}$ frequency cell constant as a function of the photon flux (base light intensity); b) Relative transfer efficiency as a function of photon flux; c) RC time constant on the cell for WO_3 electrodes with different thickness as a function of photon flux. The measurements were performed at 0.82 V.

IMPS as function of light intensity. Figure V.18a shows the dependence of the surface recombination and charge transfer processes as a function of the base light intensity at 0.82

V, close to the photocurrent onset: both rate constants become faster when the system is irradiated with a higher number of photons. This is another illustration of the complex dynamics at these porous, nanoparticulate oxide semiconductors: the increase in light intensity appears to slightly disfavor charge transfer, hence, although the charge transfer rate constant is larger than the recombination rate constant regardless of the illumination intensity, the charge transfer efficiency appears to increase at lower illumination intensities. Similarly, the RC time constant decreases as the illumination intensity increases, which may indicate a somewhat faster transport and charging process at higher light intensity. This trend is observed in many oxide semiconductors and is regularly interpreted in terms of a trap-limited transport process. The behavior of the RC time constant as a function of potential does not depend significantly on the thickness of the semiconductor layer. De Jongh and Vanmaekelberg[175] proposed that the RC time constant obtained from IMPS measurements was closely related with the diffusion time of the majority carriers in the semiconductor, in this case electrons. Taking this approximation, the diffusion time of electrons are represented by figure V.17d as a function of potential, semiconductor thickness and illumination intensity. Disregarding the thinnest electrode and comparing at the same potential, it suggests that the diffusion time is higher for thicker electrodes and it seems to increase with more positive potentials. Figure V.18(c) shows that the diffusion time will be shorter at higher illumination intensities, which is what is expected in some transport mechanisms limited by traps.

Conclusions

In this work, we present a simple method to synthesize WO_3 with a favorable photoelectrochemical response for the water oxidation reaction. This photocurrent response shows an optimal thickness under front side illumination of about 4 μm, but almost a steady state photocurrent was obtained for thicker films under back side illumination. IMPS measurements illustrate that for this material the charge transfer rate constant and relative efficiency is mainly determined by the potential applied and not so much by film thickness. For potentials more negative than about 0.8 V, the charge transfer and recombination rate constants are faster probably as a result of a surface modification, meanwhile for more positive potentials a slow charge transfer and recombination process are obtained.

Additionally, it was found that charge transfer rate to the electrolyte solution is faster than the recombination rate, highlighting the potential of the material to work as an electrode in the water oxidation reaction. The results also show that charge carrier-driving force is strongly determined by light penetration and not only by carrier dynamics.

V.3. Effect of Surface Recombination on the Photoelectrochemical Performance of WO_3-$CuWO_4$ and $CuWO_4$-$BiVO_4$ Heterojunction Materials

Due to its interesting photocatalytic properties, $CuWO_4$ is an attractive n-type semiconductor with potential application in solar water splitting. As this material is considered as an indirect n-type semiconductor, a thick layer is necessary for a good light absorption that present a low photocurrent density. Also, carrier mobility is low due to trap states associated with Cu_{3d} electrons. The low current density is associated to reduced chemical efficiency and slow surface kinetics. [113,114]

After the hydrothermal growth of the WO_3 nanorod array films, the samples presented a blue color, which has previously been related to the presence of $(NH_4)WO_3$ [165]. After annealing at 550 °C, the layers turned to a yellowish color corresponding to stoichiometric WO_3. After the conversion step using a $Cu(NO_3)_2$ solution, the impregnated films sintered at 550 °C and 650 °C turned to bright yellow in concordance with previous reports [114,176,177], while for films annealed at 450 °C a light yellow coloration was observed.

Figure V.19 shows the X-ray diffraction patterns and the cross-sectional SEM images of the sintered WO_3 and $CuWO_4$ films at different temperatures. Figure V.19a illustrates that the WO_3 nanorod film sintered at 550 °C exhibits the characteristic plane reflections of monoclinic WO_3.

Note that the intensity of the (002) plane reflection is lower than the half of the expected value indicating a considerable preferential orientation along the [001] direction, in accordance with the rod-like morphology, essentially orthogonal to the substrate surface. After impregnation with the Cu^{2+} solution followed by annealing at 450 °C, weak reflections at 15.2° and 18.8° indicate a small fraction of $CuWO_4$ in the films, thus forming a WO_3-$CuWO_4$ heterojunction; these reflections correspond to the (010) and (100) planes of the triclinic crystal structure of the tungstate phase (JCPDS # 72-0616). After annealing at 550 °C, a mixture of WO_3 and $CuWO_4$ is still present, while after annealing at 650 °C the majority of material corresponds to $CuWO_4$. With increasing annealing temperature, the complete crystallization of $CuWO_4$ can be observed, as shown in figure V.19a-iv. According to previous reports, the decomposition of $Cu(NO_3)_2$ occurs first at 170 °C

forming CuO [177,178], which afterwards reacts with WO_3 to produce $CuWO_4$ at about 550 °C [113].

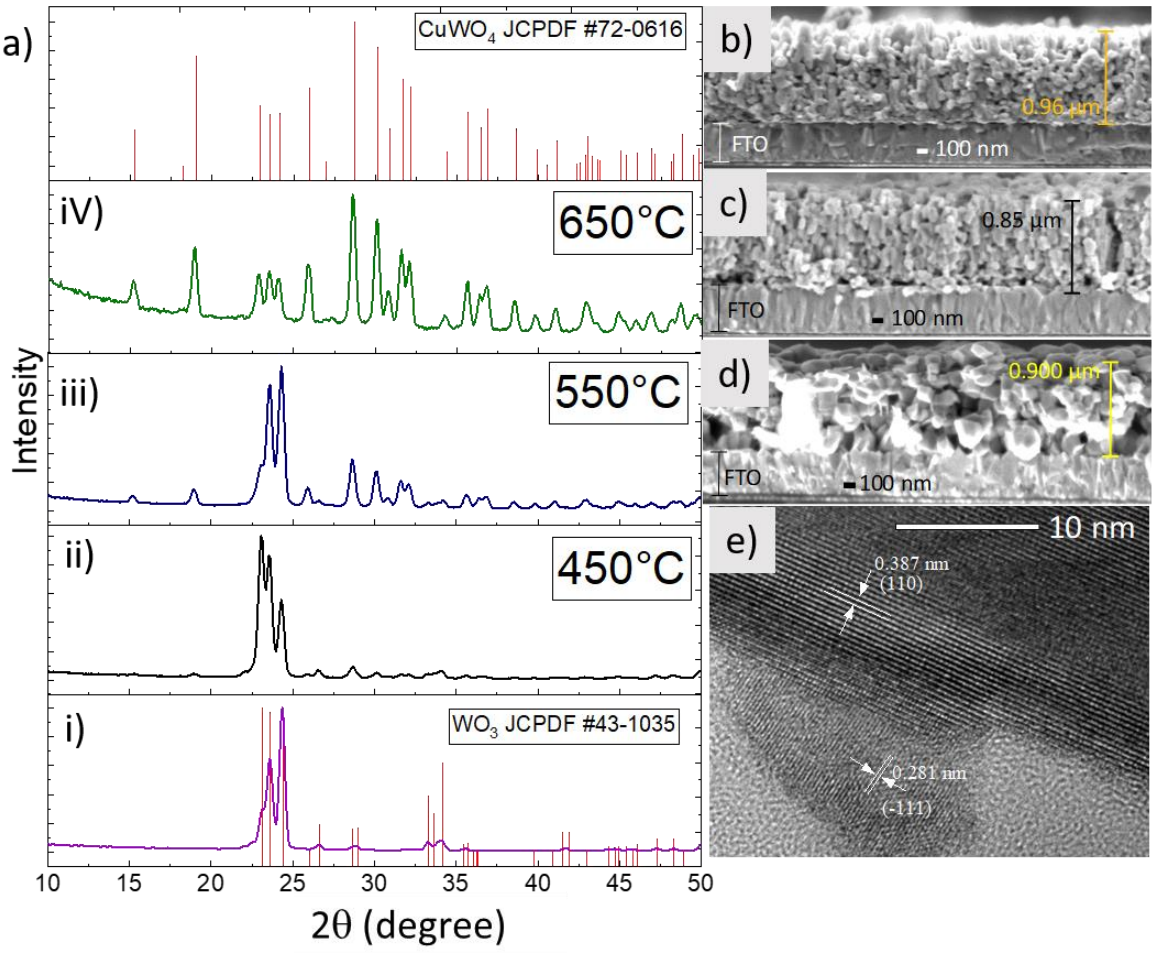

Figure V. 19. a) XRD patterns of the WO_3 and $CuWO_4$ films: i) WO_3 film annealed at 550 °C, ii), iii), iv) $CuWO_4$ films prepared at annealing temperatures of 450, 550 and 650 °C, respectively. On the right, cross-sectional SEM images of b) $CuWO_4$ sintered at 450 °C; c) $CuWO_4$ sintered at 550 °C; d) $CuWO_4$ sintered at 650 °C. e) HRTEM image of an individual nanorod of $CuWO_4$ sintered at 550°C.

A cross-sectional SEM image for film annealed at 450 °C is shown in figure V.19b, where the 1D rod array structure is visible with a 960 nm thickness, suggesting that the morphology of the sacrificial template has not been appreciably changed at this temperature. For the film sintered at 550 °C film (figure V.19c), the reduced elongation of the rods results in an apparently more compact film as result of the volume contraction corresponding to the conversion of WO_3 to $CuWO_4$: the monoclinic WO_3 unit cell and a

volume of about 422.8 $Å^3$, while $CuWO_4$ is triclinic with a unit cell and a volume of about 132.1 $Å^3$. Interestingly, the $CuWO_4$ morphology observed is similar to the typical morphology of WO_3 sintered at temperatures higher than 600 °C, indicating an epitaxial growth mechanism. After sintering at 650 °C, the $CuWO_4$ grain size increases and the pinacoidal morphology is easily observable in particles larger than 100 nm. The high-resolution TEM image in figure V.19e of particles annealed at 550 °C shows a lattice spacing of 0.387 nm, that matches with the (110) inter-planar distance of triclinic $CuWO_4$. However, as the triclinic structure shares several inter-planar distances with WO_3, it is difficult to conclude from TEM if the system is phase-pure.

The normalized UV-Vis absorbance spectra of the WO_3 and the $CuWO_4$ array films obtained at different temperatures are shown in figure V.20. The WO_3 nanorod array film shows an absorbance onset wavelength of 480 nm corresponding to a bandgap of about 2.6 eV [95,104,107,179]. Upon conversion of WO_3 into $CuWO_4$, the band edge absorption wavelength gradually red-shifts to 550 nm, that corresponds with the relatively narrow bandgap of about 2.3 eV of $CuWO_4$ [112,113,176].

Figures V.20b and c show *IPCE* plots recorded at 1.42 V(RHE) for $CuWO_4$ films prepared at different annealing temperatures, under front-side and back-side illumination. Under back-side illumination, the light corresponding to the wavelength range from 300 – 340 nm is effectively absorbed by the FTO substrate, thus limiting the observed photocurrent. In general, it can be concluded that the films prepared at 450 °C and 550 °C exhibit similar *IPCE* values, with much smaller values for the sample sintered at 650 °C. These results indicate that although light absorption is very similar for the films annealed at 650 °C, the photocurrent is much smaller suggesting that either charge separation or surface recombination significantly affect the collection efficiency of the photoanode. Note that the films annealed at 650 °C consist of essentially pure $CuWO_4$, but that at lower annealing temperature, a core of WO_3 is still apparently present, which appears to be essential in order to obtain photocurrent.

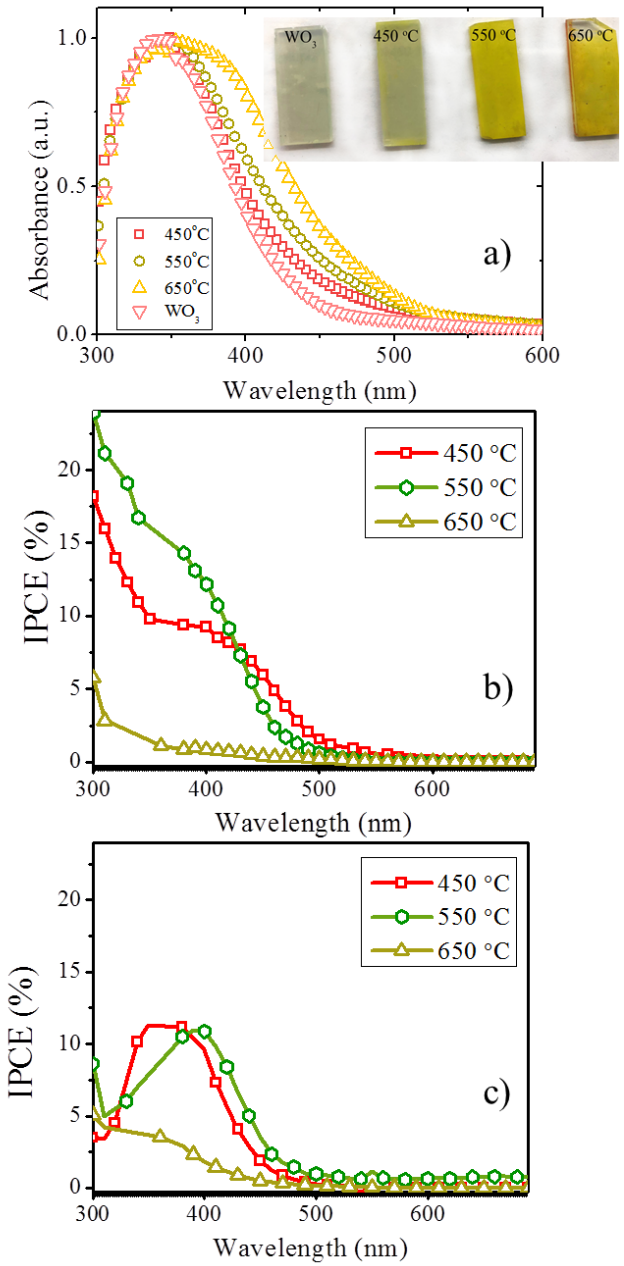

Figure V. 20. a) UV-Vis absorbance spectra of WO_3 annealed at 500 °C for 3 h, and $CuWO_4$ prepared by annealing at 450 °C, 550 °C and 650 °C for 1 h; the inset in a) shows a photograph of samples. Figures b and c show the IPCE versus wavelength measured for $CuWO_4$ films annealed at 450 °C, 550 °C and 650°C: b) under front-side illumination; and c) under back-side illumination.

Figure V.21 shows the current density – potential (*I-V*) curves for the WO_3-$CuWO_4$ samples prepared at different annealing temperatures under simulated 1 sun illumination (100 mW cm^{-2}) in two different electrolyte solutions; a phosphate buffer at pH 7 and a

borate buffer at pH 9. In the dark, the $CuWO_4$ electrodes exhibit an I-V curve typical for an n-type semiconductor, with no appreciable anodic current from 0.5 V(RHE) to 1.8 V(RHE), while a forward cathodic current is observed at more negative potentials; at a potential larger than 1.8 V a dark oxidation current is observed caused by either a breakdown mechanism or oxidation at the partially exposed FTO surface related to the porosity of the films. Under illumination, the anodic photocurrent onset for all films was observed at about 0.7 V(RHE), related to the water oxidation reaction [176,177,180,181].

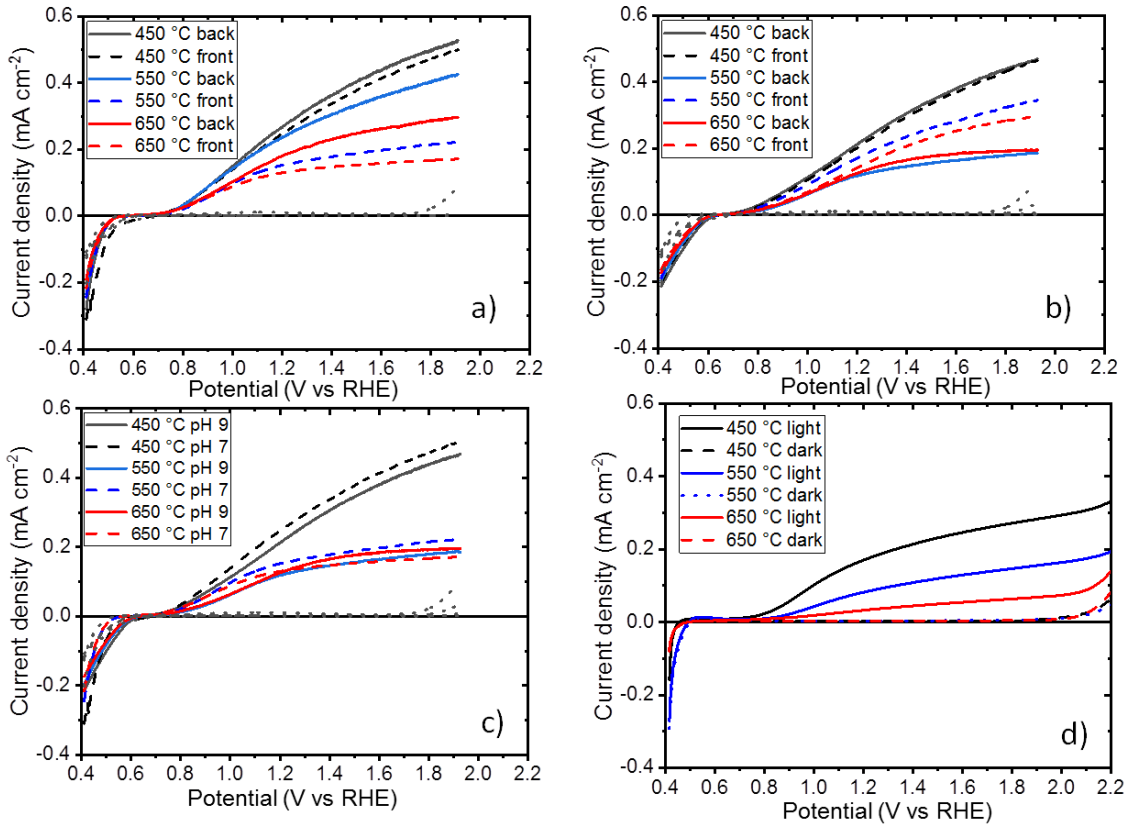

Figure V. 21. Current density–potential curves of the $CuWO_4$ photoanodes in: a) 0.1 M phosphate buffer solution at pH 7; b) 0.1 M sodium borate buffer solution at pH 9. Figure c shows a comparison between the curves for both pH values under back-side illumination. The curves were measured under 1 sun, AM 1.5G at 100 mW cm^{-2}. Figure d shows the I-V curves for illumination with a 455 nm blue LED source.

The photoelectrodes annealed at 450 °C showed a better performance under both front and back-side illumination than the electrodes annealed at 550 °C and 650 °C, with a photocurrent of 0.4 mA/cm^2 at 1.5 V(RHE). This correlates with the observation that the

material annealed at 450 °C has a significant presence of WO_3, which has been reported to have a better charge collection efficiency than $CuWO_4$ [104,145,182], while surface states significantly affect the performance of $CuWO_4$ [176]. On the other hand, WO_3 has a poor stability at pH 7 and 9, and it seems that even a small amount of $CuWO_4$ can prevent surface degradation. The electrodes annealed at 550 °C and 650 °C suffer from a large photocurrent difference under front and back-side illumination. This suggests that the collection efficiency is smaller for front-side illumination: although light absorption is better from the front side, the carriers are generated further from the FTO contact, resulting a larger loss of photocurrent. The low photocurrent obtained for the samples annealed at 650 °C, even under back-side illumination, correlates with the presence of larger particles and smaller surface area. Figure V.21c shows that the PEC performance is very similar in neutral and slightly basic electrolyte solutions. Figure V.21d shows the *I-V* curves obtained under monochromatic illumination using the 455 nm blue LED. The *I-V* curves show a better pronounced photocurrent plateau at potentials larger than 1.1 V(RHE), without change of the onset potential. Simulated sunlight contains photons of different energy, which are absorbed at different average distance from the incident surface; if the collection efficiency is a function of applied potential, the *I-V* curve is expected to show a slow increase in photocurrent with increasing potential.

In order to better understand the effect of materials properties on the charge separation and collection dynamics for the different electrodes prepared, a detailed IMPS analysis has been performed as a function of applied potential. Figure V.22 shows the IMPS spectra as a function of applied potential for the samples annealed at 450 °C, 550 °C, and 650 °C. In general, it can be observed that the crossing point on the Re(H) axis moves to larger values for more positive potentials, indicating that the *CSE* increases with more positive potential. Hence, an internal potential difference is developed that helps charge separation for all three samples. The materials annealed at 450 °C and 550 °C show similar values for the *CSE*, while the material annealed at 650 °C shows a *CSE* of a factor 10 times lower. This indicated that charge separation is not achieved efficiently for the $CuWO_4$ sample, suggesting that bulk recombination is faster than collection. On the other hand, for the samples with WO_3-$CuWO_4$ heterojunction, charge separation is much more efficient, which

indicated that the charge is separated across the heterojunction, thus preventing bulk recombination.

For all samples, at potentials more negative than 0.6 V(RHE) the IMPS spectra essentially remain in the origin, indicating that charge separation is not achieved, i.e., all generated electron – hole pairs recombine in the bulk of the materials. Between 0.6 – 0.9 V(RHE), the IMPS spectra present two semicircles, the low-frequencies semicircle in the first quadrant is associated to the competition between recombination and charge transfer to the electrolyte solution, while the high-frequency semicircle in the fourth quadrant is given by the cell time constant.

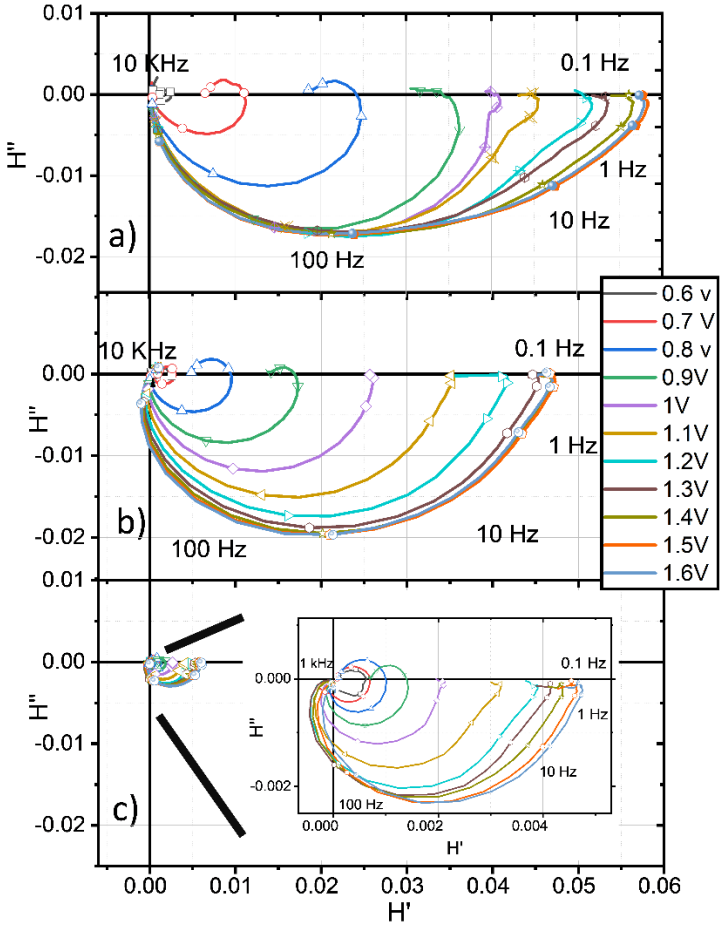

Figure V. 22. IMPS spectra obtained for photoelectrodes annealed at: a) 450 ºC; b) 550 ºC; and c) 650 ºC. The experiments were performed using a 455 nm blue LED as the illumination source. The frequency was modulated from 10,000 Hz to 0.05 Hz. The electrolyte solution consisted of a 0.1 M phosphate buffer at pH 7.

For potentials more positive than 0.9 V(RHE) the semicircle in the first quadrant is no longer observed, suggesting that charge transfer is more efficient at more positive potentials [104,137,157,161–163,183]. Interestingly, for the material annealed at 450 °C, at potentials more positive than 1.1 V(RHE) the semicircle in the fourth quadrant appears to be deformed. This is likely related to the significant presence and contribution of both phases, WO_3 and $CuWO_4$, to the charge transfer process. At potential more positive than about 1.3 V(RHE), the IMPS spectra stay essentially the same suggesting that the photocurrent plateau have been reached, which is in good agreement with the *I-V* curves in figure V.21d.

The rate constants for charge transfer and surface recombination are shown as a function of the applied potential in figure V.23. It can be concluded that the cell time constant is significantly smaller (i.e. at higher frequency), and that the rate constants observed for the samples annealed at 550 °C and 650 °C are similar, while for the samples annealed at 450 °C, the rate constants are smaller. For the 450 °C photoelectrode, consisting of the WO_3 - $CuWO_4$ heterojunction with the largest fraction of WO_3, the rate constant for surface recombination is significantly smaller, allowing for a relatively high charge transfer efficiency. Combined with the observation that the *CSE* for 450 °C is similar to the samples at 550 °C, and a factor 10 larger than for the 650 °C samples, these results are in agreement with the higher photocurrent observed for the heterojunction sample prepared at 450 °C.

In summary, the IMPS results show that the WO_3 - $CuWO_4$ heterojunction obtained by annealing at 450 °C has the largest conversion efficiency, related to both a higher charge separation efficiency and a higher relative transfer efficiency at lower potentials. It can be concluded that although CuWO4 has superior light absorption characteristics, it is necessary to optimize a heterojunction configuration in order to fully take advantage of these properties.

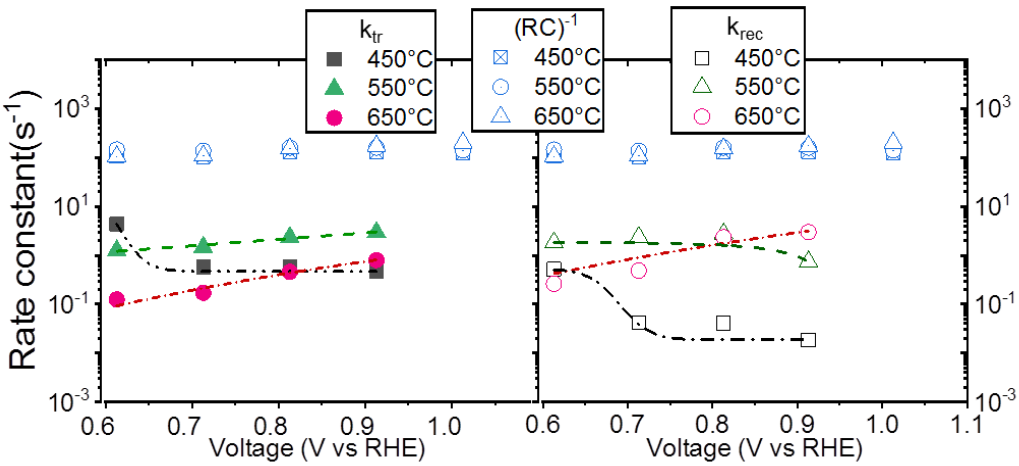

Figure V. 23. Charge transfer (k_{tr}) and surface recombination rate constant (k_{rec}), as well as the frequency corresponding to the cell time constant as a function of the applied potential, corresponding to the results shown in figure V.22.

$BiVO_4$/$CuWO_4$ heterojunction. $BiVO_4$ has been considered as a promising oxide material for solar water oxidation; the band gap of about 2.4 eV [134,184–186] permits the absorption of a considerable part of the solar spectrum, and the direct transitions allows for thin films to absorb most of the incident light, unlike $CuWO_4$. As for most semiconducting oxides, the integration of an oxygen evolution catalyst improves the photoelectrochemical efficiency [140,187,188], and strategies to further improve the performance consists in the formation of heterojunctions to enhance the charge carrier collection [125,189–191].

From the results in the previous sections, it was concluded that the materials annealed at 450 ºC and 550 ºC contain a $CuWO_4$ - WO_3 heterojunction, which helps in maximizing the *CSE*. We used this material as a substrate and deposited a thin $BiVO_4$ film on top to determine the influence of a second heterojunction, comparing the results with photoelectrodes of the $CuWO_4$ - WO_3 material annealed at 550 ºC, and $BiVO_4$ photoelectrodes deposited by spin coating. In the following, the $CuWO_4$ – WO_3 material annealed at 550 ºC will be denominated $CuWO_4$ electrode for convenience. Figures V.24a and b show the XRD patterns of the $BiVO_4$ - $CuWO_4$ heterojunction, a $BiVO_4$ film of about 200 nm, and the standards of each phase. It can be concluded that the heterojunction material shows a pattern that is a simple sum of the patterns of both components. FigureV.24c shows SEM micrographs (top view and cross-sectional images) of the

$BiVO_4/CuWO_4$ heterojunction film. A porous thin (about 100 nm) layer of $BiVO_4$ consisting of small and homogeneous particles is observed on the top of $CuWO_4$ film. Although the $BiVO_4$ layer presents some porosity, the particles form an interconnected film. The corresponding UV-Vis absorbance spectra are shown in figureV.24d. The heterojunction presents an absorption profile that resembles the weighted average of the individual phases.

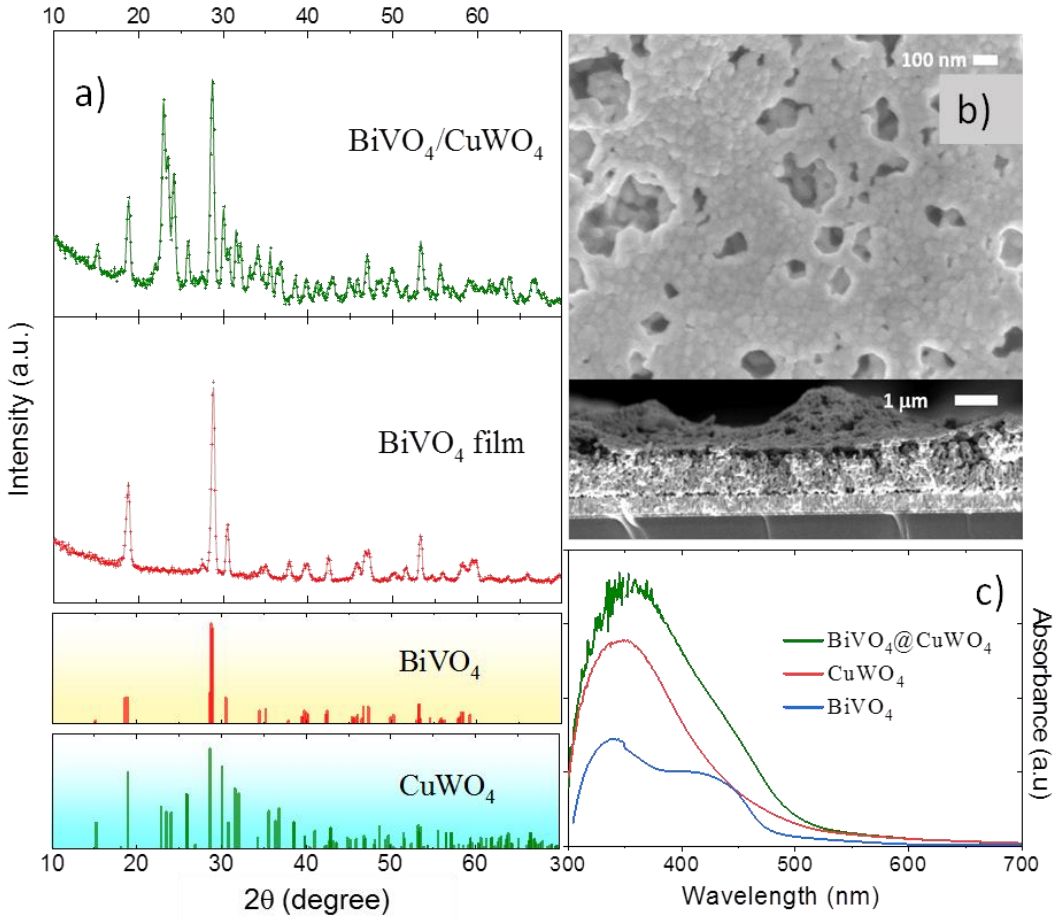

Figure V. 24. XRD pattern of: a) the $BiVO_4$ - $CuWO_4$ heterojunction; b) the $BiVO_4$ film (200 nm). The reference patterns correspond to $CuWO_4$ (JCPDS # 72-0616) and $BiVO_4$ (JCPDS #14-0688). c) Top view and cross-sectional images of $BiVO_4$ - $CuWO_4$ heterojunction. d) Absorbance spectra of the films for each phase.

Figure V.25a shows the current density - potential curves for $CuWO_4$ (550 ºC), $BiVO_4$ - $CuWO_4$ and $BiVO_4$ photoelectrodes in 0.1 M phosphate buffer (pH 7) under blue LED (455 nm) front-side illumination. It can be observed that the onset for $BiVO_4$ is at a potential about 500 mV more positive than for the $BiVO_4$ - $CuWO_4$ heterojunction electrode, which is similar as for the $CuWO_4$ electrode. At 2.1 V(RHE), the photocurrent for $BiVO_4$ only is 1.8 mA/cm^2, while for the $BiVO_4$ - $CuWO_4$ electrode the photocurrent is 1.5 mA/cm^2, and for the $CuWO_4$ electrode the photocurrent is a factor 10 times lower. Figure V.25b shows corresponding IPCE measurements at 1.22 V(RHE). The $BiVO_4/CuWO_4$ heterojunction shows a significantly higher IPCE than the other photoelectrodes, with an onset shift close to 600 nm corresponding to an optical absorption edge of about 2.1 eV. The IPCE response for $BiVO_4$ shows a lower value, suggesting that although the material presents higher absorbance, recombination at this potential is very fast.

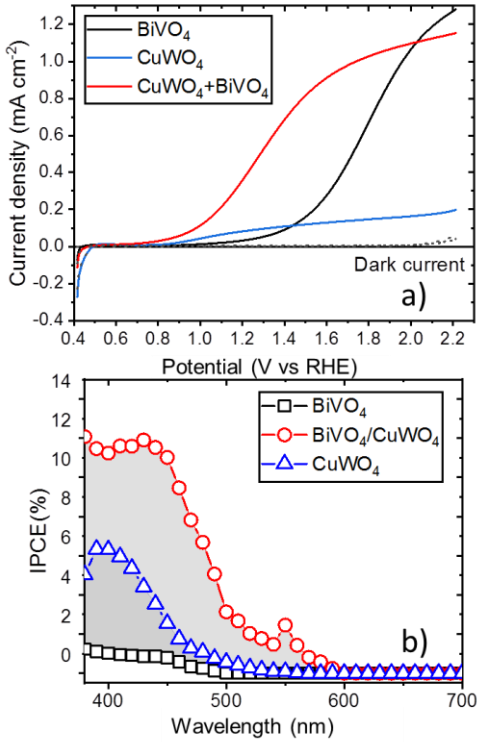

Figure V. 25. a) Current density – potential curves, and b) IPCE for $BiVO_4$, $BiVO_4$ - $CuWO_4$ and $CuWO_4$ photoanodes in 0.1 M phosphate buffer solution at pH 7, illuminated with a 455 nm blue LED source from the electrolyte side of the cell.

To understand the role of surface processes and the role of each phase in the heterojunctions, IMPS measurements were performed. Figure V.26 shows IMPS spectra as a function of the applied potential for $BiVO_4$ and $BiVO_4/CuWO_4$ heterojunction photoelectrodes. For $BiVO_4$, a first quadrant semicircle is observed from 0.6 - 1.5 V(RHE) that ends back in the origin at low frequencies, indicating that although charge separation is achieved, not many holes are transferred to the electrolytic solution as surface recombination dominates in agreement with previous reports [137,143]. It can also be concluded that the CSE for the $BiVO_4$ only film is also not large – the medium frequency crossing point occurs at relatively small values for the CSE. When the potential is increased, the low frequency intercept on the H´-axis slowly shifts to larger values, indicating an increase in EQE, which is reflected in the I-V curve.

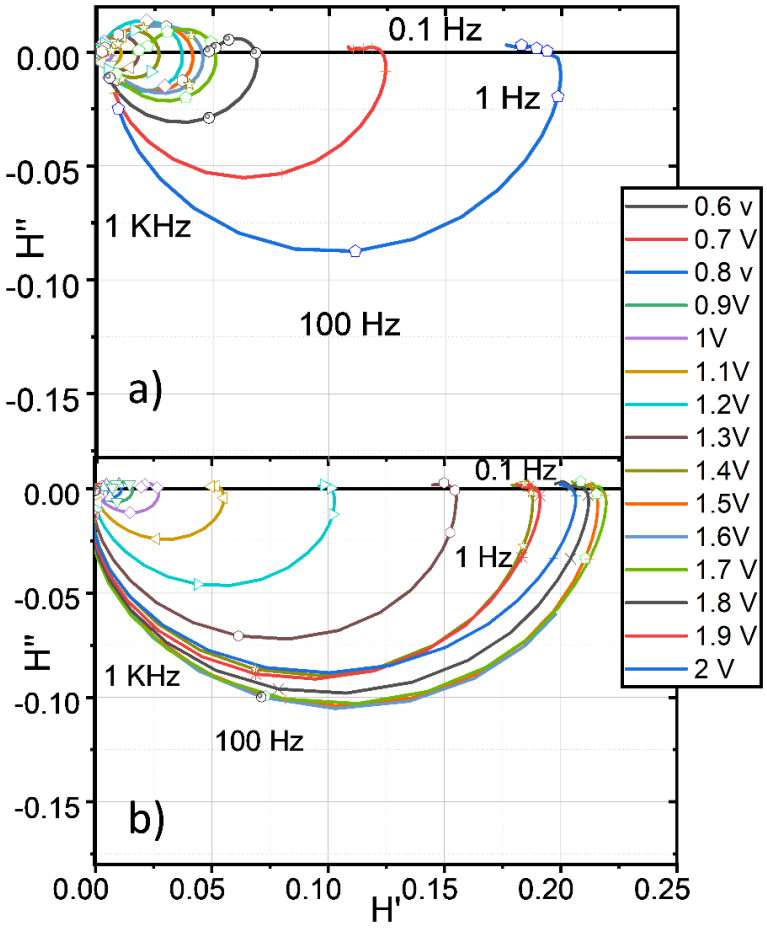

Figure V. 26. IMPS spectra of: a) $BiVO_4$; and b) $BiVO_4$ - $CuWO_4$ heterojunction photoelectrodes as a function of applied potential in 0.1 M phosphate buffer under blue LED illumination.

The IMPS spectra for the $BiVO_4/CuWO_4$ heterojunction show a different tendency. At potentials more negative than 1.0 V(RHE), an upper semicircle is observed that quickly becomes smaller when the voltage increases, indicating the balance between recombination and transfer is similar as was observed for the $CuWO_4$ photoelectrode. The CSE increases significantly at potentials more positive than 1.0 V(RHE), indicating the influence of the internal field.

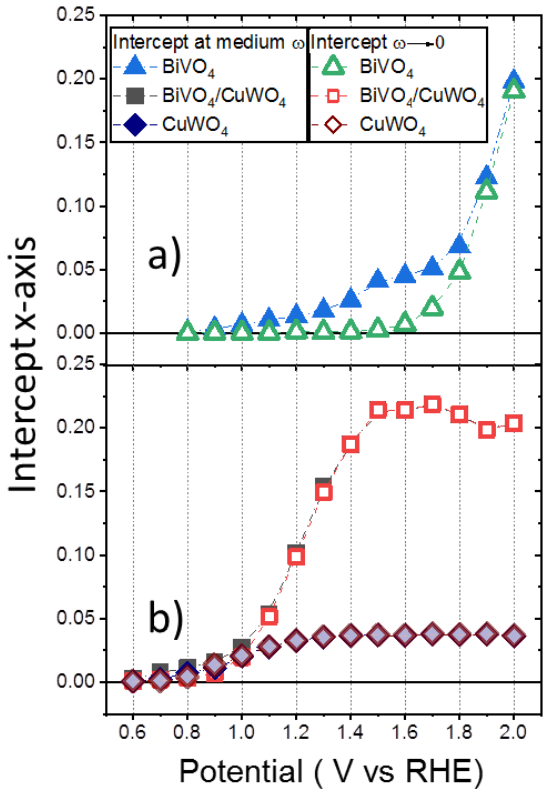

Figure V. 27. a) Crossing points and intercepts from the results shown in figure V.26 on the H´-axis of: a) $BiVO_4$; and b) the $CuWO_4$ and $CuWO_4$ - $BiVO_4$ photoelectrodes. The medium frequency crossing point corresponds to the CSE, while the low frequency intercept pertains to the EQE, respectively.

These results are highlighted in figure V.27: the crossing point on the *H´*-axis at medium frequency, corresponding to the *CSE*, and the intercept at very low frequency, corresponding to the *EQE*, are plotted against the applied potential. For both the $CuWO_4$ and the $BiVO_4$ – $CuWO_4$ heterojunction photoelectrodes, *CSE* = *EQE* for potentials more positive than about 1.0 V(RHE) indicating that charge transfer is faster than surface

recombination, and only between 0.6 – 1.0 V(RHE), there is a slight influence of surface recombination. However, for the $BiVO_4$ electrode, the *CSE* is larger than the *EQE* between 1.0 – 1.8 V(RHE), which shows that surface recombination losses are important. Note that the *CSE* for $BiVO_4$ is still lower than for the $BiVO_4$ – $CuWO_4$ heterojunction, which indicates that although light is efficiently absorbed, bulk recombination prevents the observation of a high value for the *CSE*. Interestingly, also the *EQE* is much larger for the $BiVO_4$ – $CuWO_4$ heterojunction than for the two materials alone, indicating that charge separation across the heterojunction significantly improves collection, not only by improving the *CSE* but also the transfer efficiency, by lowering the impact of surface recombination.

Conclusions

In this work, $CuWO_4$ films were synthesized by chemical modification of a WO_3 nanorod array as a partially sacrificial template, using a $Cu(NO_3)_2$ solution. The films annealed at 450 °C preserves the morphology of the sacrificial template, and XRD indicates that these films are composed of a WO_3 - $CuWO_4$ heterojunction. The films annealed at 550 °C consist mainly of $CuWO_4$, although a core of WO_3 remains. At 650 °C, the material transforms completely into the $CuWO_4$ phase, accompanied by a change in the grain size and morphology. The optical properties illustrate the transformation with the absorbance onset moving from the typical onset for WO_3 (2.6 eV) to that of $CuWO_4$ (2.3 eV). The photo-oxidation of water under front-side and back-side illumination demonstrate the collection problem of $CuWO_4$: Photoelectrodes annealed at 650 °C show a low photocurrent, due to a low charge separation efficiency. These results indicate that bulk recombination dominates the photoelectrochemical performance. For the photoelectrodes obtained at 450 °C and 550 °C, the current is higher, with similar charge separation efficiency. IMPS spectra for the material annealed at 450 °C shows that WO_3 also contributes to the charge transfer of photogenerated holes to the solution. Hence, it can be concluded that the heterojunction structure of the $CuWO_4$ – WO_3 photoelectrodes is beneficial in order to increase both the charge separation and external quantum efficiency. In addition, the $CuWO_4$ serves as a protective layer for the WO_3 material that is not generally stable at pH 7. In fact, good performance was also observed in a solution at pH 9.

The $CuWO_4$ – WO_3 material annealed at 550 °C was further explored as an underlayer substrate and using $BiVO_4$ as an overlayer. The advantages of this configuration include a better light harvesting, as $BiVO_4$ is a direct semiconductor while $CuWO_4$ is characterized by an indirect gap, and the inclusion of a second heterojunction. It is found that a $BiVO_4$ photoelectrode alone suffers from a low CSE due to bulk recombination as well as a lower EQE related to surface recombination. These two detrimental effects can be mitigated by using the $CuWO_4$ – WO_3 underlayer, which effectively extracts the photogenerated electrons thus preventing both mechanisms of recombination.

V.4. Insight into the charge transfer processes at $WO_3/BiVO_4$ sandwich heterojunction photoanodes

It has been shown in literature that $WO_3/BiVO_4$ heterojunction systems can generate a much larger photocurrent density than for the respective bare films.[142,145,192–194] The suitable light harvesting ability of $BiVO_4$ combined with the good electron conductivity of WO_3 make this heterojunction system particularly attractive for solar water splitting. Related to the band alignment between both oxides, the transfer of photoexcited electrons from the $BiVO_4$ CB to the WO_3 CB is possible, followed by rapid transport to the external circuit promoted by the higher electron mobility of WO_3.[141] Several groups have investigated this heterojunction coupling them in different configurations, including the sandwich structure.[142]

The sandwich structure deposited by spin coating showed a higher photocurrent density in comparison with a cross finger configuration, but the exact nature of the charge carrier processes in the sandwich structure is still a mystery. In this structure, $BiVO_4$ layer form an interface between the electrolyte solution and the heterojunction while WO_3 was deposited as the first layer in order to be in contact with the FTO as it is shown in figure V.28.

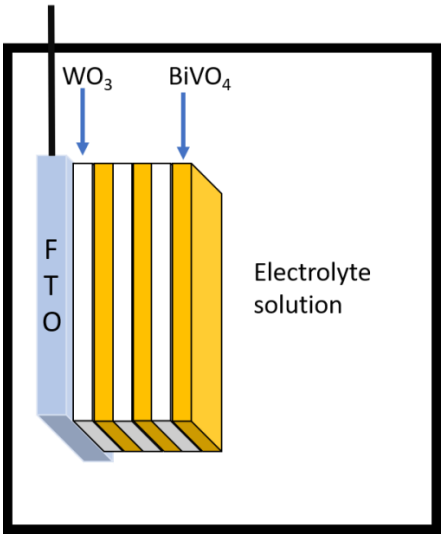

Figure V. 28. Scheme of $WO_3/BiVO_4$ sandwich heterojunction. The white rectangles correspond to WO_3 layer deposited while the yellow rectangles correspond to $BiVO_4$.

Once deposited by spin coating the films were annealed at 500 °C, and a yellow, transparent film was achieved on the FTO substrate. FigureV.31 shows the XRD patterns of the WO_3–$BiVO_4$ sandwich heterojunction; for these photoelectrodes, the peaks corresponding to WO_3 and $BiVO_4$ and clearly observed, and there is no indication of any new compound formation.

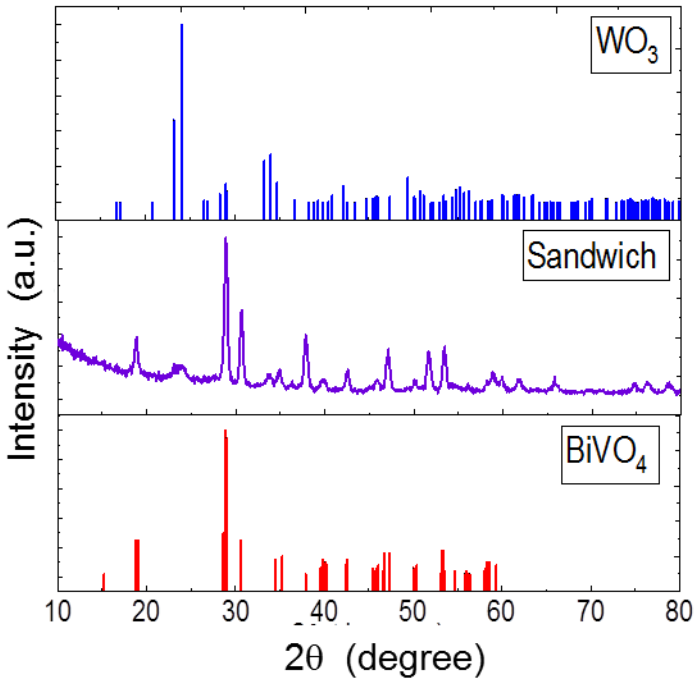

Figure V. 29. X-ray diffraction patterns of the WO_3 (JCPDS #87-2404) and $BiVO_4$ (JCPDS #14-0688) references, and the fabricated WO_3–$BiVO_4$ sandwich heterojunction film.

The surface morphologies of bare $BiVO_4$ films and the sandwich heterojunctions are shown in figure V.30. These films present the same morphology observed in previous work.[142] SEM images show that the grains of bare $BiVO_4$ are irregular in size, and that $BiVO_4$ and WO_3 particles in the sandwich configuration are interconnected.

Cross sectional SEM images of the bare films show that the WO_3 film thickness is around 50 nm while for $BiVO_4$ the film thickness is 250 nm. The sandwich structure, heterojunction film thickness is found around 300 nm, equal to the sum of both layers.

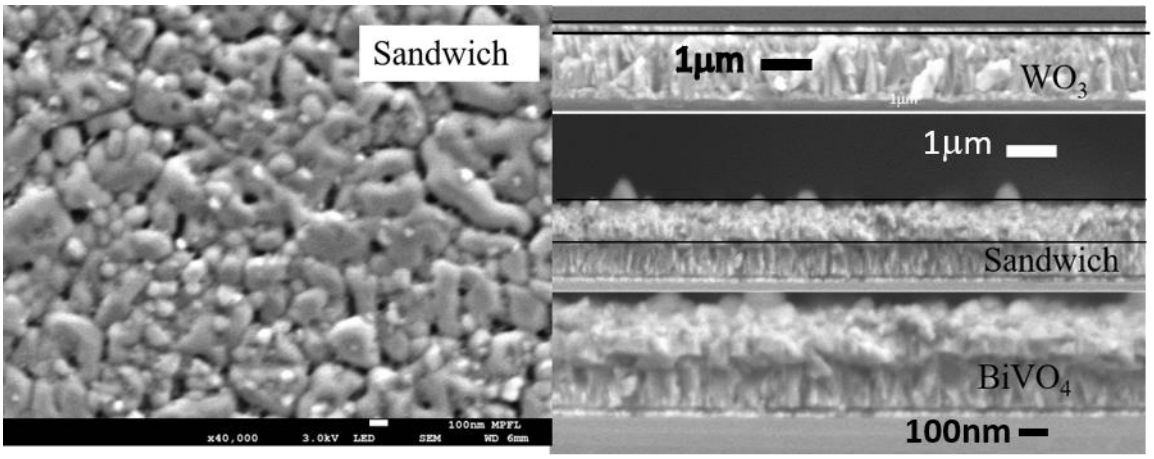

Figure V. 30. On the left, top view of the sandwich heterojunction configuration. On the right, cross-sectional images of the WO_3, $BiVO_4$ and WO_3-$BiVO_4$ sandwich structure films.

UV-Vis absorptance spectra are shown in figure V.31a). The onset of light absorption for WO_3 films is at around 450 nm, while for $BiVO_4$ photoelectrodes, the absorption edge is observed around 550 nm. In case of the heterojunctions configuration we observe two absorption edges, essentially corresponding to the sum of the WO_3 and $BiVO_4$ bare films.

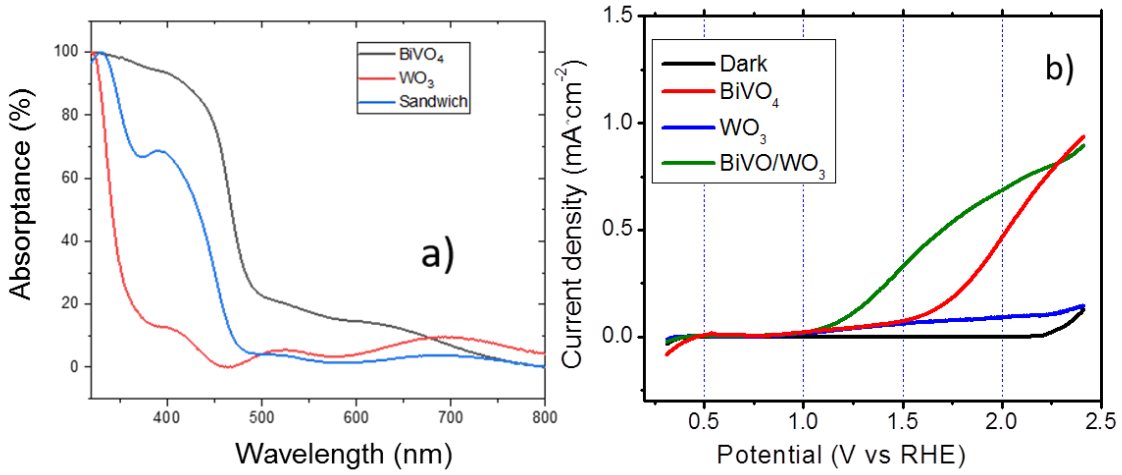

Figure V. 31. a) Absorptance spectra for WO_3, $BiVO_4$ and WO_3-$BiVO_4$ heterojunctions. b) Current-potential curves for WO_3, $BiVO_4$, and WO_3/$BiVO_4$ heterojunction films, under simulated sunlight (100 mW/cm^2) in an aqueous solution of 0.5 M sodium sulfate (Na_2SO_4) at pH 6.88.

Figure V.31b shows a set of linear-sweep voltammograms (RHE) obtained when the films are illuminated through the electrolyte (front-side illumination) with a calibrated light intensity of 100 mW/cm^2 AM 1.5G. Upon illumination, the $BiVO_4$ bare film showed a photocurrent onset at about 1 V (RHE), with an additional current onset at 1.5 V (RHE), similar to the observations in section V.3. In the case of the WO_3 film, the photocurrent onset is found at about 0.5 V (RHE)and a plateau photocurrent is reached at 1.5 V (RHE). The sandwich structure shows a significant photo-response enhancement, with the photocurrent onset being the same as obtained for WO_3 bare films.

The right choice of the electrolyte solution plays an important role in the charge transfer processes across the semiconductor/electrolyte interface, as the electrolyte composition, concentration and pH can influence the performance of the PEC cell. In most of the articles were the $BiVO_4/WO_3$ system is studied, the electrolyte solution is based on Na_2SO_4,[142,192,193,195] mainly because of the good stability of $BiVO_4$ in this electrolyte solution. However, to our knowledge, there is no study of pH influence on the photoresponse of the material. As WO_3 is part of this system, a small decrease in the pH could improve the current density: figure V.32a shows the I-V curves at in electrolyte solutions as a function of pH. At neutral pH, the photoresponse is smaller than for other pH values; additionally, the onset is more positive. Interestingly, when the pH decreases, an increase of photocurrent density is observed for the films while the onset is shifted to more negative potential values. The best photoresponse is observed at pH 3. This can be related to the presence of WO_3 particles on the surface contributing to the charge transfer process.

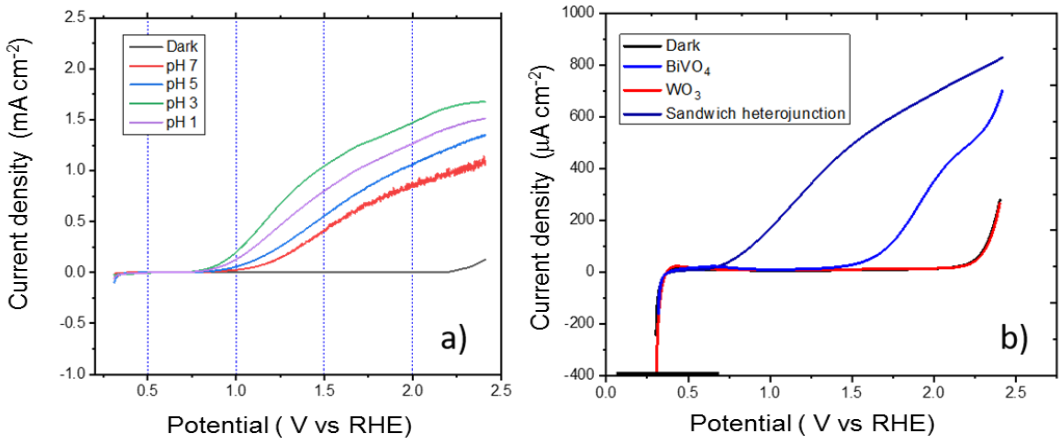

Figure V. 32. a) Current density vs applied potential curves of the $BiVO_4/WO_3$ sandwich measured at different pH values. The curves were measured using 0.5 M Na_2SO_4 adjusted at different pH and a Xe lamp as illumination source. b) I-V curves of $BiVO_4$, WO_3 and sandwich heterojunction using 0.5 M Na_2SO_4 (pH 6.88) and a blue LED as illumination source.

Although the best performance was obtained at pH 3, the IMPS characterization was performed at neutral pH, in order to compare the results to literature. Before measuring the IMPS spectra of each film in order to analyze the charge dynamics, a blue LED (455 nm) was used to measure the I-V curves (figure V.32b). Under blue LED illumination, the sandwich heterojunction presents a significantly better performance than that obtained for only $BiVO_4$ and, unlike the results obtained using a Xe lamp (figure V.31b), the WO_3 film does not show any photocurrent. This is related to the optical absorption of the very thin WO_3 film, which in addition is relatively weak at 455 nm. This implies that the modulated charge carrier generation due to the modulated blue LED light intensity occurs exclusively in the $BiVO_4$ phase. The IMPS response will therefore be determined mainly by the charge separation and recombination in the $BiVO_4$, while the WO_3 serves as an efficient charge collector.

The I-V curve measured under blue LED illumination and the corresponding IMPS spectra at different applied potentials of the sandwich heterojunction photoelectrode are shown in figure V.33. Between 0.42 and 0.82 V (RHE) the intercept at low frequencies tends to zero, indicating that surface recombination is faster than charge transfer to the solution. For $BiVO_4/WO_3$ sandwich structure, the photocurrent onset is observed at about 0.8 V

indicating that charge transfer to the solution becomes faster than recombination. This behavior can be monitored by the decrease of the semicircle present in the first quadrant of each IMPS plot as the potential is increased, related with the values of the recombination and charge transfer rate constants. At V > 1.42 V (RHE), a deformation in the second quadrant semicircle is observed that suggest that a second reaction pathway is created that influences the IMPS behavior. The appearance of the deformation coincides with the observation that the electrode surface presents bubbles due to the water oxidation reaction. It is important to mention that some authors attribute similar observations to a current multiplication process related to the use of a hole scavenger or other parallel reactions.[126]

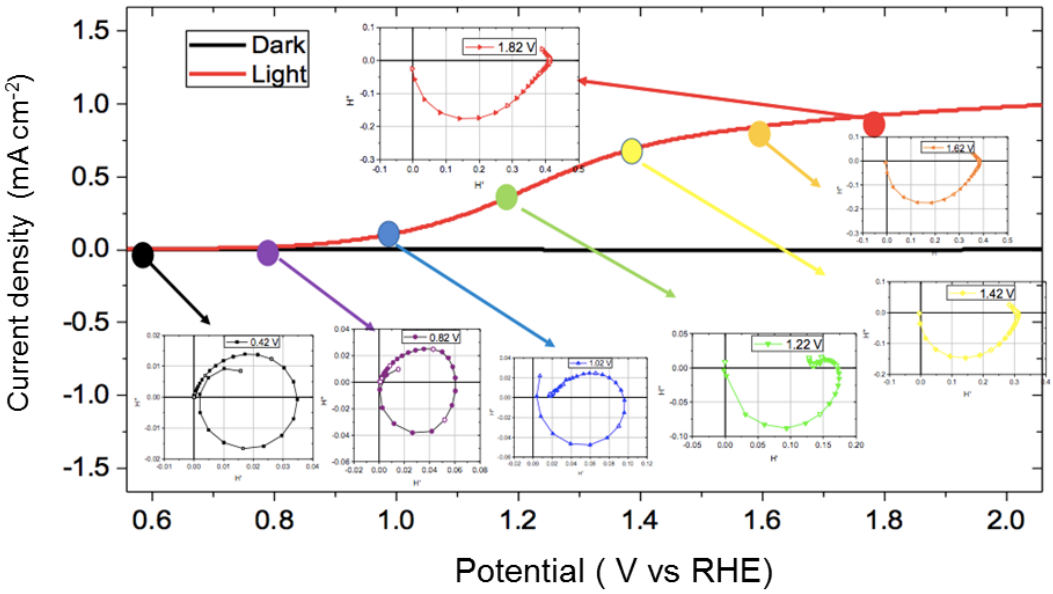

Figure V. 33. I-V curve of the WO_3–$BiVO_4$ sandwich heterojunction photoelectrode in an aqueous solution of 0.5 M Na_2SO_4 under blue LED illumination. The insets correspond to the IMPS spectra at th e specified applied potential.

The transfer and recombination rate constants and relative charge transfer efficiency are shown in figure V.34. At V < 0.82 V a full circle is observed, indicating that charge separation across the space charge layer is achieved, but that surface recombination is faster than hole transfer to the solution; i.e., the recombination rate constant is larger than the transfer rate constant.

When the applied potential is close to the photocurrent onset at 0.9 V, the tendency changes and transfer rate constant becomes larger than the recombination rate constant, implying

that transfer process is activated on the electrode. As shown in the IMPS plots as a function of the potential, the relative charge transfer efficiency increases as the potential is increased, which leads to an increase in steady-state photocurrent.

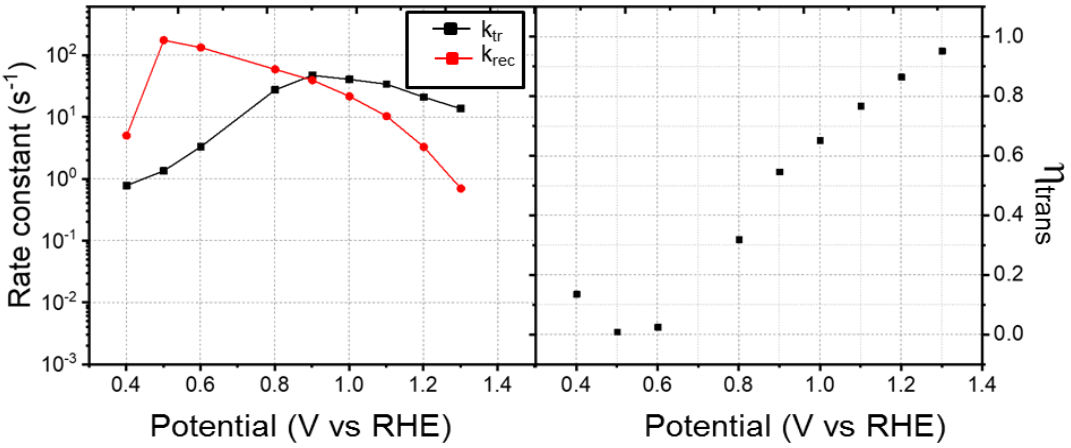

Figure V. 34. On the left, charge transfer and recombination rate constants versus applied potential, and, on the right, the relative charge transfer efficiency versus potential, both for the WO_3/$BiVO_4$ sandwich heterojunction photoanode.

These results indicate that WO_3 enhances the charge collection of $BiVO_4$ better than $CuWO_4$. Although there is a significant improvement in performance, the use of a co-catalyst could improve further the current density of the heterojunction system and shift the I-V curves to more negative potentials.

Conclusions

WO_3/$BiVO_4$ heterojunction films have been synthesized by spin coating in a multilayer sandwich configuration. The heterojunction presents an optical band gap of 500 nm similar to $BiVO_4$ films. From the cross-sectional SEM images, it was not possible to confirm the multilayer configuration, rather it appears that particles of each material are interconnected and that both phases take part in water oxidation. The photocurrent measured at pH 7 appears stable, however, it has been shown that a photoresponse improves for a solution of pH 3. IMPS measurements using a blue LED as illumination source shed light on the charge carrier dynamics of $BiVO_4$ and its interaction with WO_3, which is mainly a charge collector. The current density of the system may be further increased by the addition of co-catalyst to decrease surface recombination at lower voltages.

V.5. IMPS Study of Sn-doped iron oxide for solar water splitting

Hematite (α-Fe_2O_3) is an atractive material to be used as photoanode in PEC water splitting related to its excelent light absorption properties and abundance. The modification of hematite with Sn^{4+} has been reported to lead to an increase of the conductivity and surface area of the hematite electrode.[148,196]

Moreover, potentiostatic anodization is a simple technique for the fabrication of oxide photoelectrodes; by adding dopant precursors in the electrolyte solution, the modified oxide can be prepared in one step. It has been found that the purity of the iron foil is an important parameter in order to obtain efficient hematite photoelectrodes.[197] The objective of Sn^{4+} doping consists in improving the conductivity and electron collection efficiency of the iron oxide. A complete characterization by XRD, XPS, current – potential curves under sunlight illumination, and electrochemical impedance spectroscopy (EIS) has been performed at the Clean Energy and Nanotechnology (CLEAN) Laboratory, Joint Laboratory for Energy and Environmental Catalysis, School of Energy and Environment, City University of Hong Kong, Kowloon, Hong Kong S.A.R., in the group of Dr. Wey Yang Teoh. As part of the project, IMPS characterization of the photoelectrodes has been realized at CINVESTAV-Mérida. For this reason, this section will focus on the photoelectrochemistry and IMPS results in this system, after a brief summary of the synthesis and characterization of the materials.

The anodization synthesis of hematite was performed under alternating square wave voltage conditions that comprise of highly positive (V_{+ve} = +50 to +80 V) and slightly negative voltages (V_{-ve} = -2 to -10 V) at 100 Hz. The range of positive voltages is in line with a previous report on the potentiostatic anodization of Fe foil.[198] As the anodized layers are formed, electrostatically adsorbed fluoride ions promote localized etching of the anodized layer to form pores. Subsequent switching from positive to negative voltage repels the fluoride ions and attracts the conjugate Sn^{2+} cations. The subsequent return to the positive voltage co-oxidizes the Sn^0 and Fe foil and integrates the former into the anodized iron oxide layer as Sn-dopant. According to the *I-V* curves (fig. V.35), the optimum SnF_2 concentration to get the highest current was 75 mM while the optimum duration of

anodization synthesis was found to be 20 min (fig. V.35). The optimal annealing temperature was determined to be 600 °C.

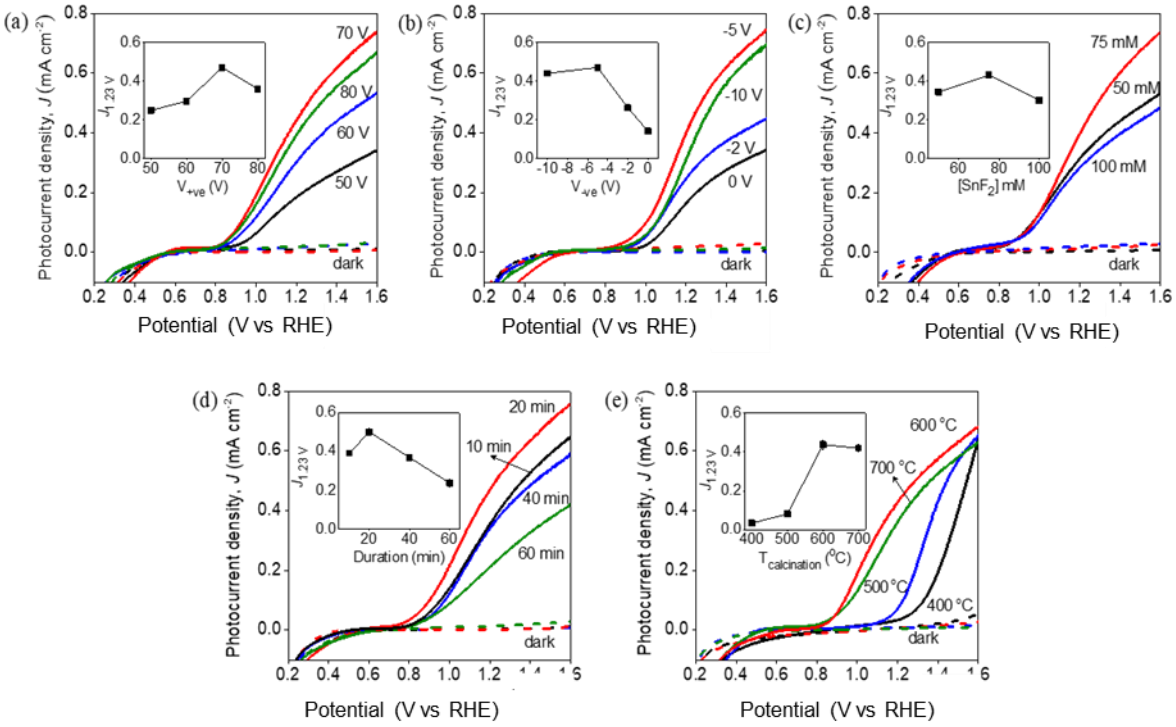

Figure V. 35. Linear sweep voltammetry (LSV) of undoped and Sn-doped iron oxide samples prepared through the parametric optimization of the synthesis of Sn-doped iron oxide by modulated anodization: (a) magnitude of applied positive voltage, V_{+ve}, (b) magnitude of applied negative voltage, V_{-ve}, (c) concentration of SnF_2, (d) duration of anodization synthesis, and (e) calcination temperature. Unless varied under the optimization of each parameter, the standard synthesis condition is V_{+ve} = +70 V, V_{-ve} = -5 V, 75 mM SnF_2, 20 min anodization synthesis, and calcination temperature 600 °C. The insets show the measured photocurrent density of the electrodes at +1.23 V vs. RHE ($J_{1.23V}$). The LSV was carried out under simulated solar irradiation, A.M. 1.5 G (1 sun intensity), in 1 M KOH aqeuous electrolyte.

XRD measurements (fig- V.36) of the Sn doped iron oxide annealed at 600 °C, show that the sample are composed by a mixture of hematite and magnetite (Fe_3O_4)). The occurrence of mixed magnetite and hematite phases are unique not only to the anodization synthesis but the general thermal annealing of metallic Fe substrate,[198–200] possibly due to the interfacial diffusion of lattice oxygen that limited the complete oxidation of the anodized layer to Fe^{3+}. Also, previous reports also did not find inferior effects of the mixed magnetite and hematite phases.[198]

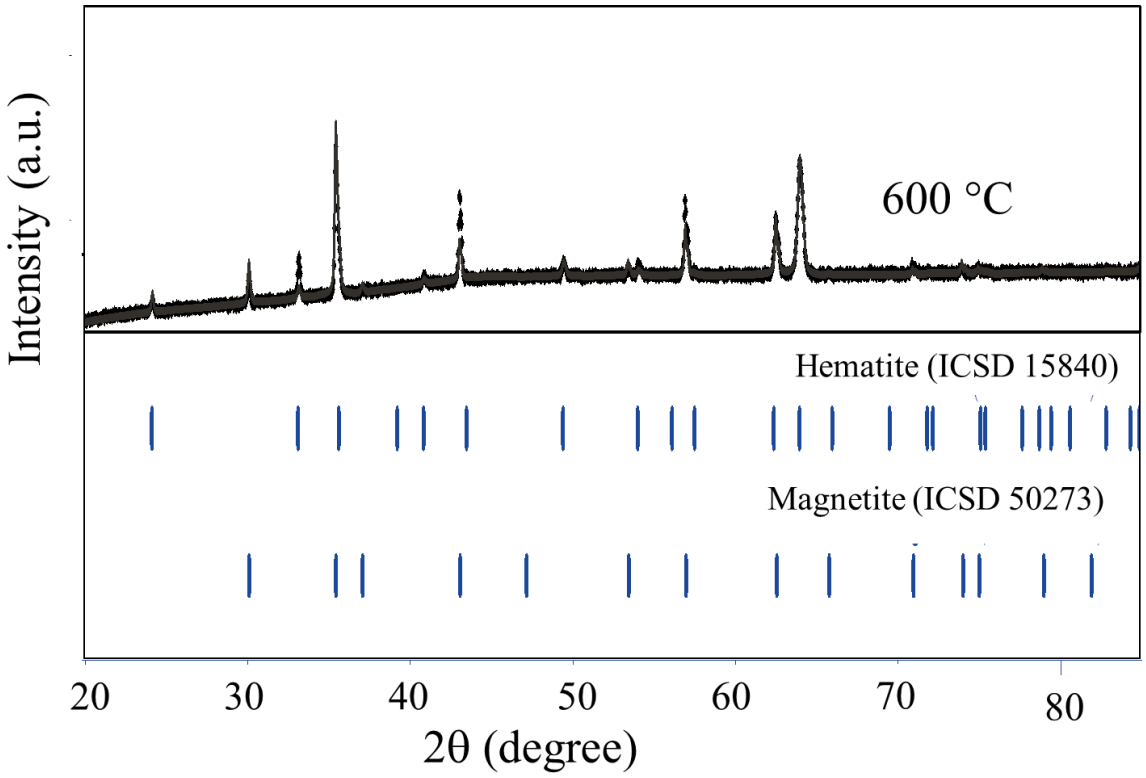

Figure V. 36. XRD pattern for Sn-doped iron oxide annealed at 600°C, with the reference peaks from the Inorganic Crystal Structure Database (ICSD) of hematite and magnetite.

The X-ray photoelectron spectroscopy (XPS) was used to gain local information of the Sn-doped and undoped anodized iron oxide samples. Figure V.37a shows the Fe 2p XPS spectra of Sn^{4+}-FeO_x and undoped FeO_x, consisting of Fe $2p_{3/2}$ (711.2 eV) and $2p_{1/2}$ (724.8 eV) belonging to the Fe^{3+} state.[201] In addition, these peaks are associated with two satellite peaks centred at 718.6 and 732.8 eV, respectively.[36] The Fe $2p_{3/2}$ and $2p_{1/2}$ peaks at 723.1 and 709.3 eV with accompanying satellite peaks at 714.2 eV and 728.1 eV, respectively, show the presence of Fe^{2+}, which verifies the coexistence of Fe_3O_4 detected earlier by XRD. The corresponding O 1s spectra for undoped and Sn-doped iron oxide (figure V.37b) show the predominant contributions of lattice oxygen (O^{2-}, binding energy at 529.2 eV), surface adsorbed moisture/molecular oxygen (binding energy at 531.9 eV) and the surface hydroxyls (–OH, binding energy at 530.6 eV).[37] Analysis of the Sn 3d of the Sn-doped iron oxide found the binding energy peak centred at 495.7 eV, inferring the oxidation of Sn^{2+} to Sn^{4+} during the process of anodization and thermal treatment (figure V.37c).[202] Further depth profile analyses were carried out to probe the actual distribution of the Sn-dopant. As shown in the inset, the Sn-dopant was enriched on the and gradually decreased up to the

depth of ~13 nm below the surface. By comparison, we verify in figure V.37d the absence of Sn in the undoped iron oxide since the negative voltage polarization was absent throughout the anodization process hence preventing the electrostatic adsorption and further reaction with Sn^{2+}.

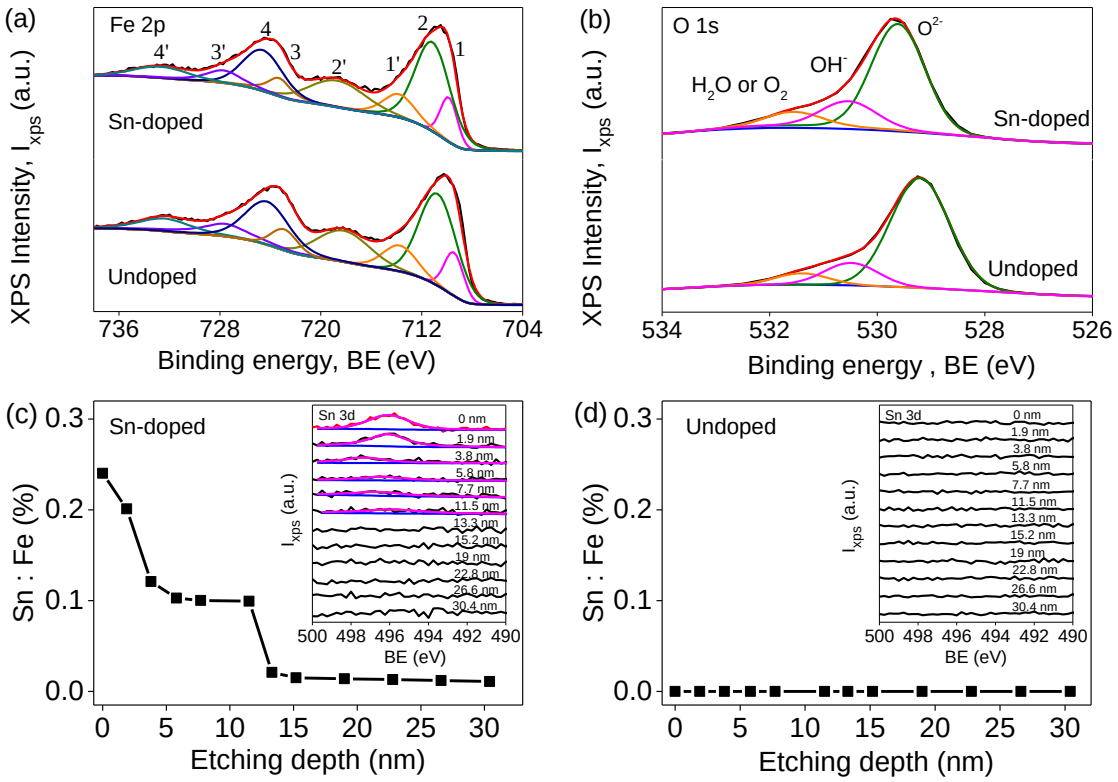

Figure V. 37. XPS spectra of (a) Fe 2p and (b) O 1s for Sn-doped and undoped iron oxide. The binding energy peaks in (a) are assigned to (1) Fe^{2+} $2p_{3/2}$, (1') Fe^{2+} $2p_{3/2}$ satellite, (2) Fe^{3+} $2p_{3/2}$, (2') Fe^{3+} $2p_{3/2}$ satellite, (3) Fe^{2+} $2p_{1/2}$, (3') Fe^{2+} $2p_{1/2}$ satellite, (4) Fe^{3+} $2p_{1/2}$, and (4') Fe^{3+} $2p_{1/2}$ satellite. The depth profile of the Sn:Fe in (c) Sn-doped and (d) undoped iron oxide samples as revealed by Ar^{+} sputtering.

Once it was proved the Sn doping on the electrode's surface, linear sweep voltammetry in dark and under illumination were performed. Figure V.38 illustrate that Sn^{4+} acts as electrocatalyst on the FeO_x film, where water oxidation starts around 1.3 V vs RHE, while for undoped films the water oxidation reaction starts only at 1.5 V vs RHE. Under illumination, both films present photoactivity under blue LED illumination. However, the doped film presents a slight shift of the onset potential of the photocurrent density.

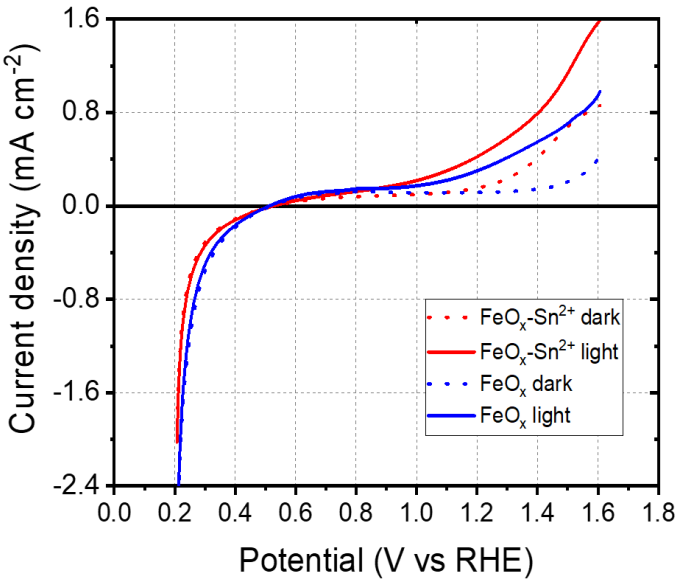

Figure V. 38. I-V curves of Iron oxide (FeO_x) and Sn-doped Iron oxide (Sn^{2+}-FeO_x) measuring in 1 M KOH using a blue LED as light source.

Figure V.39 shows the corresponding IMPS spectra of FeO_x and Sn-doped FeO_x electrodes as a function of applied potential. A low frequency semicircle in the upper quadrant is observed from 0.8 V to 1.2 V vs RHE in both cases. It can be observed that the medium frequency crossing point on the real axis is generally larger for the Sn-doped film, indicating a higher charge separation efficiency at the same potential. In addition, at relatively low potentials, for the undoped film the IMPS signal ends up close to the origin at low frequencies while for the doped samples the low frequency intercept is significantly larger at the same potential, indicating a larger external quantum efficiency.

The potential dependence of the charge transfer and recombination rate constants is illustrated in figure V. 40. For doped films, the recombination rate constant tends to decrease faster than for undoped film. Also, k_{tr} is larger than for doped films in accordance with previous results.[156] These results indicate that Sn acts as catalyst for the OER. This doping also influences the photocurrent onset; although this effect is not clearly visible in the *I-V* curves, IMPS measurements show a shift of 100 mV in the potential where the rate constants for recombination and charge transfer are equal with respect to the undoped samples.

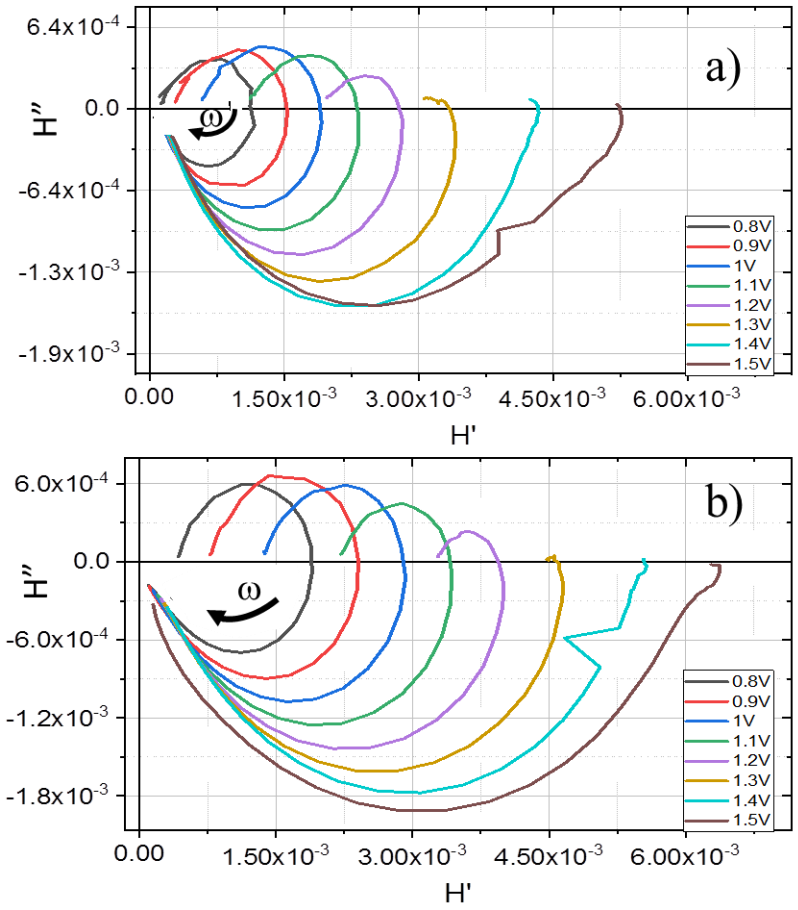

Figure V. 39. IMPS plots as a function of applied potential of a) FeO_x films and b) $Sn:FeO_x$.

The intercepts at medium and low frequencies for $Sn\text{-}FeO_x$ (figure V.41) show that although light is absorbed and excitons are formed in the space charge region, a very small number of VB holes are transferred to the electrolyte solution at V < 0.6 V vs RHE. Upon increasing the applied potential, the charge separation efficiency (CSE) increases while the external quantum efficiency (EQE) lags behind, due to surface recombination. Sn^{4+} helps to decrease surface recombination but does not eliminate this problem. This could be due to the short hole diffusion length characteristic of hematite. The layers have a thickness of 9.7 µm, implying that most of the photogenerated holes are lost by recombination in the bulk.

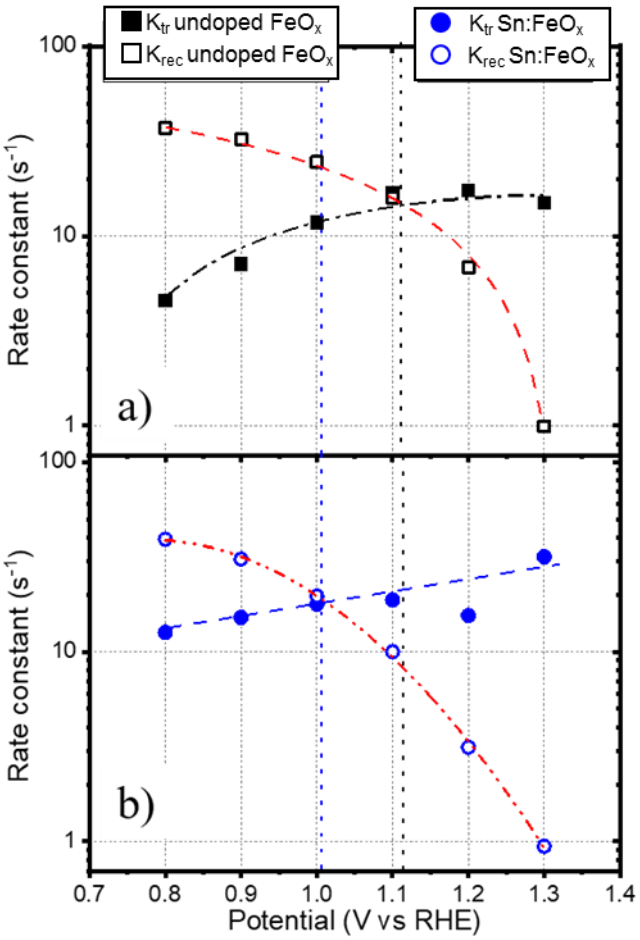

Figure V. 40. Rate constants deconvoluted from IMPS of (a) Undoped iron oxide and (b) Sn doped films.

As part of the work, the influence of Co-Pi on Sn-FeO_x films was analyzed. Unfortunately, the samples are not stable to be analyzed. Some experiments performed at CLEAN in Hong Kong suggest that Co-Pi further reduces surface recombination; however we have not yet been able to confirm these results with IMPS.

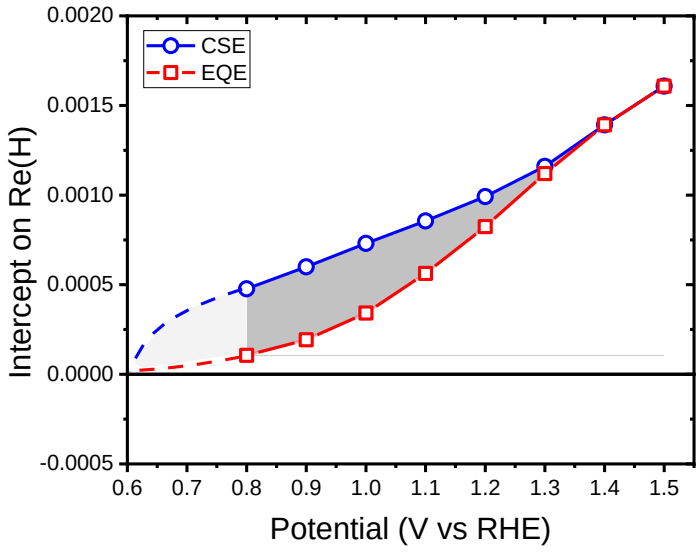

Figure V. 41. Intercept on *Re(H)* axis for Sn-FeO_x, corresponding to the product of *CSE* and *LHE* at medium frequency, and the small-signal external quantum efficiency for the frequency limit to zero, respectively.

Conclusions

IMPS measurements demonstrate the beneficial influence of Sn-doping on the behavior of iron oxide (hematite and magnetite). Sn-doping enhances the activity of the iron oxide and reduces the current onset potential by 100 mV. The Sn-dopant helped to reduce surface recombination, however, surface recombination is still significant at potentials smaller than 1.4 V vs RHE. Strategies to improve the behavior of the system such as the addition of an addicional catalyst may enhance the performance of the electrodes.

Summary and Outlook

In this work, five different semiconductor oxide systems have been evaluated for photoelectrochemical water splitting. The charge carrier dynamics at the semiconductor/electrolyte interface were characterized with the help of intensity-modulated photocurrent spectroscopy (IMPS), which is a non-destructive method to analyze these processes. The analyzed oxides are composed of earth-abundant elements and their properties make them promising materials to be used as photocathodes or photoanodes for solar water splitting. Different synthesis methodologies such as inkjet printing, screen printing, hydrothermal methods, spin coating and anodization were employed to prepare the variety of semiconducting oxide films and heterojunction photoelectrodes.

$CuBi_2O_4$ is a p-type semiconductor that can absorb a significant part of the solar spectrum and a cathodic photocurrent is observed at $V < 0.8$ V vs RHE. However, IMPS analysis shows that surface recombination plays an important role, preventing an efficient charge transfer process. Additionally, it seems that the interaction between the FTO and the material results in losses that affect the transfer efficiency. For this oxide, it may be necessary to find a new substrate capable of creating a Schottky barrier, which could allow a better collection efficiency. Also, the electrodes prepared by inkjet printing are porous, implying that the FTO substrate is also in contact with the solution, which also could interfere. In the range of film thicknesses studied, the photocurrent increases with thickness, hence new strategies for the preparation of thicker films should be explored. Figure VI.1 summarizes the processes taking place at the electrode; although $CuBi_2O_4$ is capable of absorbing a significant portion of the solar spectrum, the presence of surface states has a large impact on the behavior of the system: in the entire reverse applied potential range, the surface recombination rate constant is large in comparison to the charge transfer rate constant. Also, at more negative potentials the reduction of Cu^{2+} in the $CuBi_2O_4$ lattice appears to result in a decrease of the relative transfer efficiency. Additionally, the light intensity affects the transfer rate constant but not the recombination rate constant: as a consequence, at 1 sun, the relative transfer efficiency is significantly smaller than at lower light intensity.

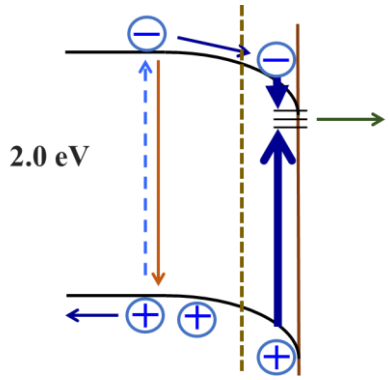

Figure VI. 1. Summary of processes taking place at inkjet printed $CuBi_2O_4$ photocathodes. The arrow thickness gives an indication of the respective rate constants – the thicker the arrow, the higher the rate constant. For $CuBi_2O_4$, the surface recombination rate constant is large in comparison to the charge transfer rate constant. Although surface recombination is the principal limitation for this photocathode, a loss of about 30% is associated to bulk recombination.

In contrast with $CuBi_2O_4$, WO_3 is an n-type semiconducting oxide material with a band gap of 2.6 eV for which surface recombination does not significantly affect the charge transfer process. However, both the charge separation and external quantum efficiencies are still below optimal, mainly due to bulk recombination, as illustrated in figure VI. 2. Strategies including the synthesis of thin nanostructured films with minimal trap density can be used to enhance the photoelectrochemical performance. At V<0.8 V(RHE), surface recombination affects the electrode, which is likely related to surface modifications at more negative voltages. For thicker films, bulk recombination increases significantly.

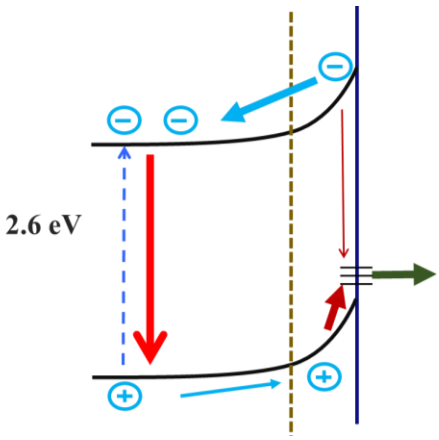

Figure VI. 2. Charge transfer dynamics at screen printed WO_3 photoanodes. IMPS analysis shows that surface recombination does not affect the transfer process of the electrode; however, bulk

recombination is the process that limits the efficiency of the electrode. Additionally, with increasing film thickness bulk recombination becomes more important.

An interesting option is to modify the WO_3 material, for example, by treatment with a Cu^{2+} solution, and subsequent sintering at high temperature. At temperatures higher than 550 °C, phase-pure films of $CuWO_4$ can be obtained, which is also an n-type semiconductor with a band gap of 2.3 eV, somewhat smaller than that of WO_3. Photoelectrochemical measurements show that this material also has a low collection efficiency, however, this problem can be solved by using a $WO_3/CuWO_4$ heterojunction system. The band alignment of both oxides (figure VI.3a) illustrates the charge transfer processes; in this system, the $CuWO_4/WO_3$ heterojunction results in an improved charge separation efficiency, related to less recombination. In addition, $CuWO_4$ is more stable than WO_3 in neutral solutions, hence a surface film of $CuWO_4$ on WO_3 partially protects the electrode. On the other hand, although $CuWO_4$ absorbs a larger range of solar spectrum, the main optical transition is indirect and thicker films are needed to harvest all the sunlight. In addition, surface recombination plays a more important role at lower voltages in comparison with WO_3. At more positive voltages, $CuWO_4$ presents higher bulk recombination and a lower collection efficiency than the $WO_3/CuWO_4$ composite as schematically shown in figure VI.3b.

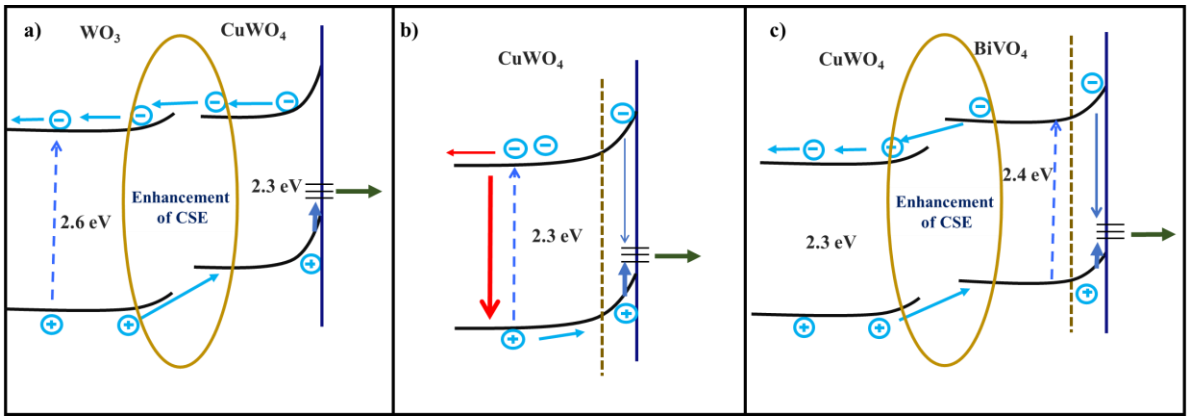

Figure VI. 3. Band diagrams of a) $WO_3/CuWO_4$, b) $CuWO_4$ and c) $CuWO_4/BiVO_4$ photoelectrodes. An enhancement of charge separation efficiency is observed for both heterojunction systems in comparison to pure $CuWO_4$ that also presents a limited collection efficiency. In the case of the $CuWO_4/BiVO_4$ heterojunction, surface recombination still affects the charge carrier dynamics. The arrow thickness is indicative of the rate constants of the respective processes.

As a consequence, it would be advantageous to modify the $CuWO_4$ film with another material with better absorption, faster charge transfer and slower surface recombination kinetics. We deposited $BiVO_4$ by spin coating on top of the $CuWO_4/WO_3$ material prepared at 550 °C, in order to form a $BiVO_4/CuWO_4$ heterojunction. $BiVO_4$ is a direct semiconductor, in contrast to $CuWO_4$, with a band gap of 2.4 eV. Hence, charge carriers are generated in the $BiVO_4$, the holes are transferred to the solution, while $CuWO_4$ acts as charge collector, and helps to decrease surface recombination on $BiVO_4$ films. The band alignment of both oxides is observed in figure VI.3c.

Another interesting possibility is to use a $WO_3/BiVO_4$ multilayer, heterojunction system, which can be prepared by a simple spin coating method that allows to easily modify the electrode design. In a sandwich-type structure, particles of both phases are interconnected to obtain a uniform layer of 300 nm. Measurements with a blue LED show that WO_3 does not absorb at 455 nm in this system, which implies that IMPS measurements performed with this LED permit to selectively observe the charge transfer processes taking place in $BiVO_4$, while observing the role of WO_3 as electron collector. In contrast to the $BiVO_4/CuWO_4$ heterojunction, it is found that the external quantum efficiency is not only defined by $BiVO_4$. Additionally, an enhancement of the charge separation efficiency has been observed. Figure VI.4 summarized the contribution of our research. A complete analysis of the electrolyte solution and the addition of a catalyst should be performed to further enhance the photoelectrochemical activity of the system.

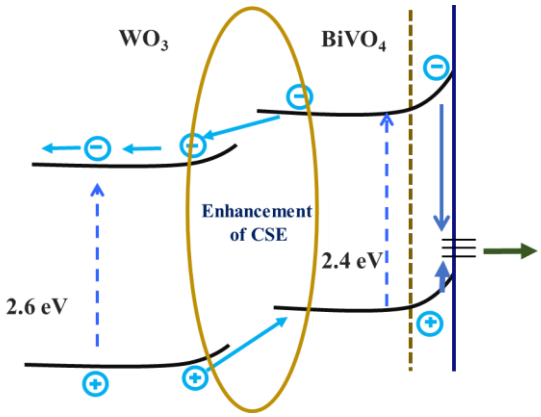

Figure VI. 4. Summary of the charge transfer processes taking place in the $WO_3/BiVO_4$ heterojunction system. For this system, photogeneration is achieved in both phases, which influences the EQE. Surface recombination is an important process in the electrode dynamics.

The final system discussed in this work pertains to iron oxide in the hematite form, modified with tin. The doping with Sn^{4+} results in a reduction of the overpotential, which indicates better charge collection efficiency in this potential range, however, the electrodes still present a high surface recombination rate. Hence, the already improved efficiency by modification with tin may be improved even more by adding a suitable electrocatalyst, which by increasing the charge transfer rate constant can result in less surface recombination. In comparison to undoped films, Sn^{4+} affects the charge separation efficiency and bulk recombination positively. At V > 1.3 V(RHE), the doped electrodes show a favorable balance between charge transfer and surface recombination.

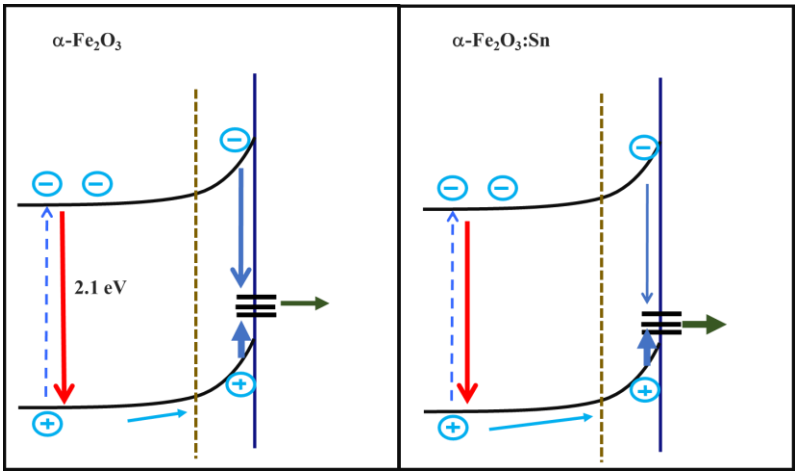

Figure VI. 5. Comparison of the charge carrier dynamics at the surface of a) α-Fe_2O_3 and b) α-Fe_2O_3:Sn electrodes. For α-Fe_2O_3 films, the surface recombination rate is faster than for the doped films. Also, Sn-doped films have a faster charge transfer rate in comparison to undoped films.

In general, this thesis focuses on a detailed study of the balance between charge generation, charge separation, charge transfer to the solution, and both bulk and surface recombination. The balance of the respective rates defines the performance of semiconducting oxide photoelectrodes in the solar water splitting process. The main problems and possible actions to improve the electrode performance have been described for five different systems, illustrating that a better understanding of the fundamental processes is essential to be able to improve our ability to design efficient solar water splitting devices that could be scaled-up in the future, providing us with hydrogen as a clean solar fuel and solar energy storage system.

List of publications

(1) Lv, X.; Rodriguez-Gutiérrez, I.; Hu, C.; Shang, J.; Sit, P. H. L.; Ye, C.; Oskam, G.; Teoh, W. Y. **Modulated Anodization Synthesis of Sn-Doped Iron Oxide with Enhanced Solar Water Splitting Performance**. *Mater. Today Chem.* **2019**, *12*, 7–15.

(2) Rodríguez-Gutiérrez, I. G.; García-Rodríguez, R.; Rodríguez-Pérez, M. J.; Vega-Poot, A.; Rodriguez Gattorno, G.; Parkinson, B. A.; Oskam, G. **Charge Transfer and Recombination Dynamics at Inkjet-Printed $CuBi_2O_4$ Electrodes for Photoelectrochemical Water Splitting.** *J. Phys. Chem. C* **2018**, 122, 48, 27169-27179

(3) Yan, Y.; Qin, D.; Duan, S.-F.; Tao, C.; Geng, Y.-Y.; Yao, X.; Kang, X.-W.; Su, J.-Z.; Rodríguez-Gutiérrez, I.; Kan, M.; et al. **Phosphorus-Doped Isotype g-C_3N_4/g-C_3N_4: An Efficient Charge Transfer System for Photoelectrochemical Water Oxidation**. *ChemCatChem* **2018**, *10*, 1–9.

(4) Rodríguez-Pérez, M.; Rodríguez-Gutiérrez, I.; Vega-Poot, A.; García-Rodríguez, R.; Rodríguez-Gattorno, G.; Oskam, G. **Charge Transfer and Recombination Kinetics at WO_3 for Photoelectrochemical Water Oxidation**. *Electrochim. Acta* **2017,** *258*, 900–908.

(5) Rodríguez-Gutiérrez,I. Djatubai,F. Rodríguez-Pérez,M. Su,J. Rodríguez-Gattorno, G. Vayssieres, L. Oskam. G. **Effect of Surface Recombination in the Photoelectrochemical Performance of $CuWO_4$ And $CuWO_4$-$BiVO_4$ Heterojunction** *submitted to Electrochim. Acta (2019).*

(6) Rodríguez-Gutiérrez,I. Djatubai,F. Rodríguez-Pérez,M. Su,J. Rodríguez-Gattorno, G. Vayssieres, L. Oskam. G. **Influence of the film structure on the charge transfer dynamics of WO_3-$BiVO_4$ multilayer system.** *Manuscript*.

References

(1) Pachauri, R. K.; Allen, M. R.; Barros, V. R.; Broome, J.; Cramer, W.; Christ, R.; Church, J. A.; Clarke, L.; Dahe, Q.; Dasgupta, P.; et al. *Climate Change 2014: Synthesis Report. Contribution of Working Groups I, II and III to the Fifth Assessment Report of the Intergovernmental Panel on Climate Change*; Geneva, Switzerland, 2014.

(2) Hu, S.; Xiang, C.; Haussener, S.; Berger, A. D.; Lewis, N. S. An Analysis of the Optimal Band Gaps of Light Absorbers in Integrated Tandem Photoelectrochemical Water-Splitting Systems. *Energy Environ. Sci.* **2013**, *6* (10), 2984–2993.

(3) Fujishima, A.; Honda, K. Electrochemical Photolysis of Water at a Semiconductor Electrode. *Nature* **1972**, *238*, 37–38.

(4) Jeong, S.; Song, J.; Lee, S. Photoelectrochemical Device Designs toward Practical Solar Water Splitting: A Review on the Recent Progress of $BiVO_4$ and $BiFeO_3$ Photoanodes. *Appl. Sci.* **2018**, *8* (8), 1388.

(5) Scheuermann, A. G.; Lawrence, J. P.; Kemp, K. W.; Ito, T.; Walsh, A.; Chidsey, C. E. D.; Hurley, P. K.; McIntyre, P. C. Design Principles for Maximizing Photovoltage in Metal-Oxide-Protected Water-Splitting Photoanodes. *Nat. Mater.* **2016**, *15* (1), 99–105.

(6) Rajeshwar, K.; McConnell, R.; Licht, S. *Solar Hydrogen Generation: Toward a Renewable Energy Future*, 1st ed.; Springer: New York, 2008.

(7) Atkins, P.; de Paula, J. *Physical Chemistry*, 8th ed.; W.H. Freeman and Company: New York, 2006.

(8) Millet, P. Fundamentals of Water Electrolysis. In *Hydrogen Production*; Godula-Jopek, A., Ed.; Wiley-Interscience: Germany, 2015; Vol. 2, pp 33–62.

(9) Guevarra, D.; Shinde, A.; Suram, S. K.; Sharp, I. D.; Toma, F. M.; Haber, J. A.; Gregoire, J. M. Development of Solar Fuels Photoanodes through Combinatorial Integration of Ni-La-Co-Ce Oxide Catalysts on $BiVO_4$. *Energy Environ. Sci.* **2016**, *9* (2), 565–580.

(10) Fornarini, L.; Nozik, A. J.; Parkinson, B. A. The Energetics of p/n Photoelectrolysis Cells. *J. Phys. Chem.* **1984**, *88* (15), 3238–3243.

(11) Alfaifi, B. Y.; Ullah, H.; Alfaifi, S.; Tahir, A. A.; Mallick, T. K.

Photoelectrochemical Solar Water Splitting: From Basic Principles to Advanced Devices. *Veruscript Funct. Nanomater.* **2018**, *2*, #BDJOC3.

(12) Abe, R. Recent Progress on Photocatalytic and Photoelectrochemical Water Splitting under Visible Light Irradiation. *J. Photochem. Photobiol. C Photochem. Rev.* **2011**, *11* (4), 179–209.

(13) Walter, M. G.; Warren, E. L.; McKone, J. R.; Boettcher, S. W.; Mi, Q.; Santori, E. A.; Lewis, N. S. Solar Water Splitting Cells. *Chem. Rev.* **2010**, *110* (11), 6446–6473.

(14) Fujishima, A.; Honda, K. Electrochemical Evidence for the Mechanism of the Primary Stage of Photosynthesis. *Bull. Chem. Soc. Jpn.* **1971**, *44* (21), 1148–1150.

(15) Pan, H. Principles on Design and Fabrication of Nanomaterials as Photocatalysts for Water-Splitting. *Renew. Sustain. Energy Rev.* **2016**, *57*, 584–601.

(16) Grätzel, M. Photoelectrochemical Cells. *Nature* **2001**, *414*, 338.

(17) Memming, R. Principles of Semiconductor Physics. In *Semiconductor electrochemistry*; Springer, 2015; pp 1–22.

(18) West, A. R. *Solid State Chemistry and Its Applications*, 2nd ed.; Wiley-Interscience: New Delhi, 2014.

(19) Atkins, P.; Overton, T.; Rourke, J.; Weller, M.; Armstrong, F.; Hagerman, M. *Inorganic Chemistry; New York*; Oxford University Press, 2010.

(20) Housecroft, C. E.; Sharpe, A. G. *Inorganic Chemistry;* PEARSON Prentice Hall: London, 2005.

(21) Lüth, H. *Solid Surfaces, Interfaces and Thin Films*; Springer: Berlin, 2010.

(22) D, V. Principles of Photoelectrochemical Cells. In *Photoelectrochemical Hydrogen Production*; van de Krol, R., Michael, G., Eds.; Springer US, 2012; Vol. 102, pp 13–67.

(23) Lewerenz, H.-J.; Peter, L. *Photoelectrochemical Water Splitting*; Energy and Environment Series; The Royal Society of Chemistry, 2014.

(24) Nellist, M. R.; Laskowski, F. A. L.; Lin, F.; Mills, T. J.; Boettcher, S. W. Semiconductor-Electrocatalyst Interfaces: Theory, Experiment, and Applications in Photoelectrochemical Water Splitting. *Acc. Chem. Res.* **2016**, *49* (4), 733–740.

(25) Sze, S. M.; Kwok, K. *Physics of Semiconductor Devices*; Wiley-Interscience: third, 2006.

(26) Butler, M. A. Photoelectrolysis and Physical Properties of the Semiconducting Electrode WO_2. *J. Appl. Phys.* **1977**, *48* (5), 1914–1920.

(27) Grundmann, M. *The Physics of Semiconductors: An Introduction Including Nanophysics and Applications*, third.; Springer: Germany, 2006.

(28) Joshi, U. A.; Palasyuk, A. M.; Maggard, P. A. Photoelectrochemical Investigation and Electronic Structure of a p -Type $CuNbO_3$ Photocathode. *J. Phys. Chem. C* **2011**, *115* (27), 13534–13539.

(29) Gerischer, H. Charge Transfer Processes at Semiconductor-Electrolyte Interfaces in Connection with Problems of Catalysis. *Surf. Sci.* **1969**, *18* (1), 97–122.

(30) Prévot, M. S.; Jeanbourquin, X. A.; Bourée, W. S.; Abdi, F.; Friedrich, D.; van de Krol, R.; Guijarro, N.; Le Formal, F.; Sivula, K. Evaluating Charge Carrier Transport and Surface States in $CuFeO_2$ Photocathodes. *Chem. Mater.* **2017**, *29* (11), 4952–4962.

(31) Pu, P.; Cachet, H.; Sutter, E. M. M. Electrochemical Impedance Spectroscopy to Study Photo - Induced Effects on Self-Organized TiO_2 Nanotube Arrays. *Electrochim. Acta* **2010**, *55* (20), 5938–5946.

(32) Memming, R.; Schwandt, G. Potential and Charge Distribution at Semiconductor-Electrolyte Interfaces. *Angew. Chemie Int. Ed.* **1967**, *6* (10), 851–861.

(33) Yang, Y.; Xu, D.; Wu, Q.; Diao, P. Cu_2O/CuO Bilayered Composite as a High-Efficiency Photocathode for Photoelectrochemical Hydrogen Evolution Reaction. *Sci. Rep.* **2016**, *6* (35158), 1–13.

(34) Valenti, M.; Dolat, D.; Biskos, G.; Schmidt-Ott, A.; Smith, W. A. Enhancement of the Photoelectrochemical Performance of $CuWO_4$ Thin Films for Solar Water Splitting by Plasmonic Nanoparticle Functionalization. *J. Phys. Chem. C* **2015**, *119* (4), 2096–2104.

(35) Pellegrini, B. A Detailed Analysis of the Metal-Semiconductor Contact. *Solid. State. Electron.* **1974**, *17* (3), 217–237.

(36) Ni, M.; Leung, M. K. H.; Leung, D. Y. C.; Sumathy, K. A Review and Recent Developments in Photocatalytic Water-Splitting Using TiO_2 for Hydrogen Production. *Renew. Sustain. Energy Rev.* **2007**, *11* (3), 401–425.

(37) Rajeshwar, K. *Encyclopedia of Electrochemistry*; Wiley-VCH Verlag GmbH & Co.

KGaA, 2007.

(38) Giménez, S.; Bisquert, J. *Photoelectrochemical Solar Fuel Production*; 2016.

(39) Sivula, K.; van de Krol, R. Semiconducting Materials for Photoelectrochemical Energy Conversion. *Nat. Rev. Mater.* **2016**, *1*, 15010.

(40) Huang, Q.; Ye, Z.; Xiao, X. Recent Progress in Photocathodes for Hydrogen Evolution. *J. Mater. Chem. A* **2015**, *3* (31), 15824–15837.

(41) Sun, B.; Zhou, G.; Gao, T.; Zhang, H.; Yu, H. NiO Nanosheet/TiO_2 Nanorod-Constructed p-n Heterostructures for Improved Photocatalytic Activity. *Appl. Surf. Sci.* **2016**, *364*, 322–331.

(42) Sim, L. C.; Ng, K. W.; Ibrahim, S.; Saravanan, P. Preparation of Improved P-n Junction NiO/TiO_2 Nanotubes for Solar-Energy-Driven Light Photocatalysis. *Int. J. Photoenergy* **2013**, *2013*, 659013.

(43) Wu, P.; Liu, Z.; Chen, D.; Zhou, M.; Wei, J. Flake-like NiO/WO_3 p-n Heterojunction Photocathode for Photoelectrochemical Water Splitting. *Appl. Surf. Sci.* **2018**, *440*, 1101–1106.

(44) Sullivan, I.; Zoellner, B.; Maggard, P. A. Copper(I)-Based p-Type Oxides for Photoelectrochemical and Photovoltaic Solar Energy Conversion. *Chem. Mater.* 2016, pp 5999–6016.

(45) Trimarchi, G.; Peng, H.; Im, J.; Freeman, A. J.; Cloet, V.; Raw, A.; Poeppelmeier, K. R.; Biswas, K.; Lany, S.; Zunger, A. Using Design Principles to Systematically Plan the Synthesis of Hole-Conducting Transparent Oxides: Cu_3VO_4 and Ag_3VO_4 as a Case Study. *Phys. Rev. B - Condens. Matter Mater. Phys.* **2011**, *84* (16), 1–14.

(46) Li, C.; Hisatomi, T.; Watanabe, O.; Nakabayashi, M.; Shibata, N.; Domen, K.; Delaunay, J. J. Simultaneous Enhancement of Photovoltage and Charge Transfer in Cu_2O-Based Photocathode Using Buffer and Protective Layers. *Appl. Phys. Lett.* **2016**, *109* (3).

(47) Zhang, J.; Ma, H.; Liu, Z. Highly Efficient Photocatalyst Based on All Oxides WO_3/Cu_2O Heterojunction for Photoelectrochemical Water Splitting. *Appl. Catal. B Environ.* **2017**, *201*, 84–91.

(48) Jang, Y. J.; Jang, J.-W.; Choi, S. H.; Kim, J. Y.; Kim, J. H.; Youn, D. H.; Kim, W. Y.; Han, S.; Sung Lee, J. Tree Branch-Shaped Cupric Oxide for Highly Effective

Photoelectrochemical Water Reduction. *Nanoscale* **2015**, *7* (17), 7624–7631.

(49) Kushwaha, A.; Moakhar, R. S.; Goh, G. K. L.; Dalapati, G. K. Morphologically Tailored CuO Photocathode Using Aqueous Solution Technique for Enhanced Visible Light Driven Water Splitting. *J. Photochem. Photobiol. A Chem.* **2017**, *337*, 54–61.

(50) Samarasekara, P.; Kumara, N. T. R. N.; Yapa, N. U. S. Sputtered Copper Oxide (CuO) Thin Films for Gas Sensor Devices. *J. Phys. Condens. Matter* **2006**, *18* (8), 2417–2420.

(51) Díez-García, M. I.; Gómez, R. Investigating Water Splitting with $CaFe_2O_4$ Photocathodes by Electrochemical Impedance Spectroscopy. *ACS Appl. Mater. Interfaces* **2016**, *8* (33), 21387–21397.

(52) Matsumoto, Y.; Omae, M.; Sugiyama, K.; Sato, E. New Photocathode Materials for Hydrogen Evolution: Calcium Iron Oxide ($CaFe_2O_4$) and Strontium Iron Oxide ($Sr_7Fe_{10}O_{22}$). *J. Phys. Chem.* **1987**, *91* (3), 577–581.

(53) Ida, S.; Yamada, K.; Matsunaga, T.; Hagiwara, H.; Matsumoto, Y.; Ishihara, T. Preparation of P-Type $CaFe_2O_4$ Photocathodes for Producing Hydrogen from Water. *J. Am. Chem. Soc.* **2010**, *132* (49), 17343–17345.

(54) Choi, Y.-H.; Yang, K. D.; Kim, D.-H.; Nam, K. T.; Hong, S.-H. P-Type $CuBi_2O_4$ Thin Films Prepared by Flux-Mediated One-Pot Solution Process with Improved Structural and Photoelectrochemical Characteristics. *Mater. Lett.* **2016**, *188*, 192–196.

(55) Wang, F.; Chemseddine, A.; Abdi, F. F.; van de Krol, R.; Berglund, S. P. Spray Pyrolysis of $CuBi_2O_4$ Photocathodes: Improved Solution Chemistry for Highly Homogeneous Thin Films. *J. Mater. Chem. A* **2017**, *5* (25), 12838–12847.

(56) Hahn, N. T.; Holmberg, V. C.; Korgel, B. A.; Mullins, C. B. Electrochemical Synthesis and Characterization of P-$CuBi_2O_4$ Thin Film Photocathodes. *J. Phys. Chem. C* **2012**, *116* (10), 6459–6466.

(57) Paracchino, A.; Laporte, V.; Sivula, K.; Grätzel, M.; Thimsen, E. Highly Active Oxide Photocathode for Photoelectrochemical Water Reduction. *Nat. Mater.* **2011**, *10*, 456.

(58) Yang, C.; Tran, P. D.; Boix, P. P.; Bassi, P. S.; Yantara, N.; Wong, L. H.; Barber, J.

Engineering a $Cu_2O/NiO/Cu_2MoS_4$ Hybrid Photocathode for H_2 Generation in Water. *Nanoscale* **2014**, *6* (12), 6506–6510.

(59) Díaz-García, A. K.; Lana-Villarreal, T.; Gómez, R. Sol–gel Copper Chromium Delafossite Thin Films as Stable Oxide Photocathodes for Water Splitting. *J. Mater. Chem. A* **2015**, *3* (39), 19683–19687.

(60) Kaya, I. C.; Akin, S.; Akyildiz, H.; Sonmezoglu, S. Highly Efficient Tandem Photoelectrochemical Solar Cells Using Coumarin6 Dye-Sensitized $CuCrO_2$ Delafossite Oxide as Photocathode. *Sol. Energy* **2018**, *169*, 196–205.

(61) Creissen, C. E.; Warnan, J.; Reisner, E. Solar H_2 Generation in Water with a $CuCrO_2$ Photocathode Modified with an Organic Dye and Molecular Ni Catalyst. *Chem. Sci.* **2018**, *9* (6), 1439–1447.

(62) Prévot, M. S.; Jeanbourquin, X. A.; Bourée, W. S.; Abdi, F.; Friedrich, D.; van de Krol, R.; Guijarro, N.; Le Formal, F.; Sivula, K. Evaluating Charge Carrier Transport and Surface States in $CuFeO_2$ Photocathodes. *Chem. Mater.* **2017**, *29* (11), 4952–4962.

(63) Gu, J.; Yan, Y.; Krizan, J. W.; Gibson, Q. D.; Detweiler, Z. M.; Cava, R. J.; Bocarsly, A. B. P-Type $CuRhO_2$ as a Self-Healing Photoelectrode for Water Reduction under Visible Light. *J. Am. Chem. Soc.* **2014**, *136* (3), 830–833.

(64) Guerrero, A.; Bisquert, J. Perovskite Semiconductors for Photoelectrochemical Water Splitting Applications. *Curr. Opin. Electrochem.* **2017**, *2* (1), 144–147.

(65) Berglund, S. P.; Abdi, F. F.; Bogdanoff, P.; Chemseddine, A.; Friedrich, D.; van de Krol, R. Comprehensive Evaluation of $CuBi_2O_4$ as a Photocathode Material for Photoelectrochemical Water Splitting. *Chem. Mater.* **2016**, *28*, 4231–4242.

(66) Nakabayashi, Y.; Nishikawa, M.; Nosaka, Y. Fabrication of $CuBi_2O_4$ Photocathode through Novel Anodic Electrodeposition for Solar Hydrogen Production. *Electrochim. Acta* **2014**, *125* (3), 191–198.

(67) Park, H. S.; Lee, C.; Reisner, E. Photoelectrochemical Reduction of Aqueous Protons with a $CuO|CuBi_2O_4$ Heterojunction under Visible Light Irradiation. *Phys. Chem. Chem. Phys.* **2014**, *16* (41), 22462–22465.

(68) Sharma, G.; Zhao, Z.; Sarker, P.; Nail, B. A.; Wang, J.; Huda, M.; Osterloh, F. Electronic Structure, Photovoltage, and Photocatalytic Hydrogen Evolution with p-

$CuBi_2O_4$ Nanocrystals. *J. Mater. Chem. A* **2015**, *4*, 2936–2942.

(69) Abdelkader, E.; Nadjia, L.; Ahmed, B. Preparation and Characterization of Novel $CuBi_2O_4/SnO_2$ p-n Heterojunction with Enhanced Photocatalytic Performance under UVA Light Irradiation. *J. King Saud Univ. - Sci.* **2015**, *27* (1), 76–91.

(70) Liu, S.; Zhou, J.; Lu, Y.; Su, J. Pulsed Laser/ Electrodeposited $CuBi_2O_4/BiVO_4$ p-n Heterojunction for Solar Water Splitting. *Sol. Energy Mater. Sol. Cells* **2018**, *180* (February), 123–129.

(71) Arai, T.; Yanagida, M.; Konishi, Y.; Iwasaki, Y.; Sugihara, H.; Sayama, K. Efficient Complete Oxidation of Acetaldehyde into CO_2 over $CuBi_2O_4/WO_3$ Composite Photocatalyst under Visible and UV Light Irradiation. *J. Phys. Chem. C* **2007**, *111* (21), 7574–7577.

(72) Walter, M. G.; Warren, E. L.; McKone, J. R.; Boettcher, S. W.; Mi, Q.; Santori, E. A.; Lewis, N. S. Solar Water Splitting Cells. *Chem. Rev. (Washington, DC, United States)* **2010**, *110* (11), 6446–6473.

(73) Vicente, R.; Soler, J.; Arques, A.; Amat, A. M.; Frontistis, Z.; Xekoukoulotakis, N.; Mantzavinos, D. Comparison of Different TiO_2 Samples as Photocatalyst for the Degradation of a Mixture of Four Commercial Pesticides. *J. Chem. Technol. Biotechnol.* **2014**, *89* (8), 1259–1264.

(74) Fujishima, A.; Zhang, X. Titanium Dioxide Photocatalysis: Present Situation and Future Approaches. *Comptes Rendus Chim.* **2006**, *9* (5), 750–760.

(75) Park, J. H.; Kim, S.; Bard, A. J. Novel Carbon-Doped TiO_2 Nanotube Arrays with High Aspect Ratios for Efficient Solar Water Splitting. *Nano Lett.* **2006**, *6* (1), 24–28.

(76) Momeni, M. M.; Ghayeb, Y. Photoelectrochemical Water Splitting on Chromium-Doped Titanium Dioxide Nanotube Photoanodes Prepared by Single-Step Anodizing. *J. Alloys Compd.* **2015**, *637*, 393–400.

(77) Dholam, R.; Patel, N.; Adami, M.; Miotello, A. Hydrogen Production by Photocatalytic Water-Splitting Using Cr- or Fe-Doped TiO_2 Composite Thin Films Photocatalyst. *Int. J. Hydrogen Energy* **2009**, *34* (13), 5337–5346.

(78) Cho, I. S.; Chen, Z.; Forman, A. J.; Kim, D. R.; Rao, P. M.; Jaramillo, T. F.; Zheng, X. Branched TiO_2 Nanorods for Photoelectrochemical Hydrogen Production. *Nano*

Lett. **2011**, *11* (11), 4978–4984.

(79) Pan, K.; Dong, Y.; Zhou, W.; Pan, Q.; Xie, Y.; Xie, T.; Tian, G.; Wang, G. Facile Fabrication of Hierarchical TiO_2 Nanobelt/ZnO Nanorod Heterogeneous Nanostructure: An Efficient Photoanode for Water Splitting. *ACS Appl. Mater. Interfaces* **2013**, *5* (17), 8314–8320.

(80) Wang, G.; Wang, H.; Ling, Y.; Tang, Y.; Yang, X.; Fitzmorris, R. C.; Wang, C.; Zhang, J. Z.; Li, Y. Hydrogen-Treated TiO_2 Nanowire Arrays for Photoelectrochemical Water Splitting. *Nano Lett.* **2011**, *11* (7), 3026–3033.

(81) Iwashina, K.; Kudo, A. Rh-Doped $SrTiO_3$ Photocatalyst Electrode Showing Cathodic Photocurrent for Water Splitting under Visible-Light Irradiation. *J. Am. Chem. Soc.* **2011**, *133* (34), 13272–13275.

(82) Ng, J.; Xu, S.; Zhang, X.; Yang, H. Y.; Sun, D. D. Hybridized Nanowires and Cubes: A Novel Architecture of a Heterojunctioned $TiO_2/SrTiO_3$ Thin Film for Efficient Water Splitting. *Adv. Funct. Mater.* **2010**, *20* (24), 4287–4294.

(83) Kato, H.; Kudo, A. Visible-Light-Response and Photocatalytic Activities of TiO_2 and $SrTiO_3$ Photocatalysts Codoped with Antimony and Chromium. *J. Phys. Chem. B* **2002**, *106* (19), 5029–5034.

(84) Pinheiro, A. N.; Firmiano, E. G. S.; Rabelo, A. C.; Dalmaschio, C. J.; Leite, E. R. Revisiting $SrTiO_3$ as a Photoanode for Water Splitting: Development of Thin Films with Enhanced Charge Separation under Standard Solar Irradiation. *RSC Adv.* **2014**, *4* (4), 2029–2036.

(85) Meng, X.; Zhang, Z. Bismuth-Based Photocatalytic Semiconductors: Introduction, Challenges and Possible Approaches. *J. Mol. Catal. A Chem.* **2016**, *423*, 533–549.

(86) Shim, J.; Lee, C.-R.; Lee, H.-K.; Lee, J.-S.; Cairns, E. J. Electrochemical Characteristics of Pt–WO_3/C and Pt–TiO_2/C Electrocatalysts in a Polymer Electrolyte Fuel Cell. *J. Power Sources* **2001**, *102* (1), 172–177.

(87) Cui, X.; Shi, J.; Chen, H.; Zhang, L.; Guo, L.; Gao, J.; Li, J. Platinum/Mesoporous WO_3 as a Carbon-Free Electrocatalyst with Enhanced Electrochemical Activity for Methanol Oxidation. *J. Phys. Chem. B* **2008**, *112* (38), 12024–12031.

(88) Ham, D. J.; Phuruangrat, A.; Thongtem, S.; Lee, J. S. Hydrothermal Synthesis of Monoclinic WO_3 Nanoplates and Nanorods Used as an Electrocatalyst for Hydrogen

Evolution Reactions from Water. *Chem. Eng. J.* **2010**, *165* (1), 365–369.

(89) Penza, M.; Tagliente, M. A.; Mirenghi, L.; Gerardi, C.; Martucci, C.; Cassano, G. Tungsten Trioxide (WO_3) Sputtered Thin Films for a NO_x Gas Sensor. *Sensors Actuators B Chem.* **1998**, *50* (1), 9–18.

(90) Siciliano, T.; Tepore, A.; Micocci, G.; Serra, A.; Manno, D.; Filippo, E. WO_3 Gas Sensors Prepared by Thermal Oxidization of Tungsten. *Sensors Actuators B Chem.* **2008**, *133* (1), 321–326.

(91) Zeng, J.; Hu, M.; Wang, W.; Chen, H.; Qin, Y. NO_2-Sensing Properties of Porous WO_3 Gas Sensor Based on Anodized Sputtered Tungsten Thin Film. *Sensors Actuators B Chem.* **2012**, *161* (1), 447–452.

(92) Lee, S.-H.; Deshpande, R.; Parilla, P. A.; Jones, K. M.; To, B.; Mahan, A. H.; Dillon, A. C. Crystalline WO_3 Nanoparticles for Highly Improved Electrochromic Applications. *Adv. Mater.* **2006**, *18* (6), 763–766.

(93) Randin, J. P. Chemical and Electrochemical Stability of WO_3 Electrochromic Films in Liquid Electrolytes. *J. Electron. Mater.* **1978**, *7* (1), 47–63.

(94) Deb, S. K. Opportunities and Challenges in Science and Technology of WO_3 for Electrochromic and Related Applications. *Sol. Energy Mater. Sol. Cells* **2008**, *92* (2), 245–258.

(95) Kafizas, A.; Francàs, L.; Sotelo-Vazquez, C.; Ling, M.; Li, Y.; Glover, E.; McCafferty, L.; Blackman, C.; Darr, J.; Parkin, I. Optimizing the Activity of Nanoneedle Structured WO_3 Photoanodes for Solar Water Splitting: Direct Synthesis via Chemical Vapor Deposition. *J. Phys. Chem. C* **2017**, *121* (11), 5983–5993.

(96) Solarska, R.; Jurczakowski, R.; Augustynski, J. A Highly Stable, Efficient Visible-Light Driven Water Photoelectrolysis System Using a Nanocrystalline WO_3 Photoanode and a Methane Sulfonic Acid Electrolyte. *Nanoscale* **2012**, *4* (5), 1553.

(97) Feng, X.; Chen, Y.; Qin, Z.; Wang, M.; Guo, L. Facile Fabrication of Sandwich Structured WO_3 Nanoplate Arrays for Efficient Photoelectrochemical Water Splitting. *ACS Appl. Mater. Interfaces* **2016**, *8* (28), 18089–18096.

(98) Newton, K. A.; Osterloh, F. E. Size and Morphology of Suspended WO_3 Particles Control Photochemical Charge Carrier Extraction and Photocatalytic Water Oxidation Activity. *Top. Catal.* **2016**, *59* (8–9), 750–756.

(99) Solarska, R.; Bienkowski, K.; Zoladek, S.; Majcher, A.; Stefaniuk, T.; Kulesza, P. J.; Augustynski, J. Enhanced Water Splitting at Thin Film Tungsten Trioxide Photoanodes Bearing Plasmonic Gold-Polyoxometalate Particles. *Angew. Chemie - Int. Ed.* **2014**, *53* (51), 14196–14200.

(100) Bignozzi, C. A.; Caramori, S.; Cristino, V.; Argazzi, R.; Meda, L.; Tacca, A. Nanostructured Photoelectrodes Based on WO_3: Applications to Photooxidation of Aqueous Electrolytes. *Chem. Soc. Rev.* **2013**, *42* (6), 2228–2246.

(101) Butler, M. A.; Nasby, R. D.; Quinn, R. K. Tungsten Trioxide as an Electrode for Photoelectrolysis of Water. *Solid State Commun.* **1976**, *19* (10), 1011–1014.

(102) Hong, S. J.; Jun, H.; Borse, P. H.; Lee, J. S. Size Effects of WO_3 Nanocrystals for Photooxidation of Water in Particulate Suspension and Photoelectrochemical Film Systems. *Int. J. Hydrogen Energy* **2009**, *34* (8), 3234–3242.

(103) Liu, Y.; Zhao, L.; Su, J.; Li, M.; Guo, L. Fabrication and Properties of a Branched (NH4)x WO3 Nanowire Array Film and a Porous WO3 Nanorod Array Film. *ACS Appl. Mater. Interfaces* **2015**, *7* (6), 3532–3538.

(104) Rodríguez-Pérez, M.; Rodríguez-Gutiérrez, I.; Vega-Poot, A.; García-Rodríguez, R.; Rodríguez-Gattorno, G.; Oskam, G. Charge Transfer and Recombination Kinetics at WO_3 for Photoelectrochemical Water Oxidation. *Electrochim. Acta* **2017**, *258*, 900–908.

(105) Rodríguez-Pérez, M.; Chacón, C.; Palacios-González, E.; Rodríguez-Gattorno, G.; Oskam, G. Photoelectrochemical Water Oxidation at Electrophoretically Deposited WO_3 Films as a Function of Crystal Structure and Morphology. *Electrochim. Acta* **2014**, *140*, 320–331.

(106) Reyes-Gil, K. R.; Robinson, D. B. WO_3-Enhanced TiO_2 Nanotube Photoanodes for Solar Water Splitting with Simultaneous Wastewater Treatment. *ACS Appl. Mater. Interfaces* **2013**, *5* (23), 12400–12410.

(107) Santato, C.; Odziemkowski, M.; Ulmann, M.; Augustynski, J. Crystallographically Oriented Mesoporous WO_3 Films: Synthesis, Characterization, and Applications. *J. Am. Chem. Soc.* **2001**, *123* (43), 10639–10649.

(108) Yun, G.; Balamurugan, M.; Kim, H.-S.; Ahn, K.-S.; Kang, S. H. Role of WO_3 Layers Electrodeposited on SnO_2 Inverse Opal Skeletons in Photoelectrochemical

Water Splitting. *J. Phys. Chem. C* **2016**, *120* (11), 5906–5915.

(109) Anik, M.; Cansizoglu, T. Dissolution Kinetics of WO_3 in Acidic Solutions. *J. Appl. Electrochem.* **2006**, *36*, 603–608.

(110) Sarnowska, M.; Bienkowski, K.; Barczuk, P. J.; Solarska, R.; Augustynski, J. Highly Efficient and Stable Solar Water Splitting at $(Na)WO_3$ Photoanodes in Acidic Electrolyte Assisted by Non-Noble Metal Oxygen Evolution Catalyst. *Adv. Energy Mater.* **2016**, *6* (14), 1600526.

(111) Souza, E. L. S.; Sczancoski, J. C.; Nogueira, I. C.; Almeida, M. A. P.; Orlandi, M. O.; Li, M. S.; Luz, R. A. S.; Filho, M. G. R.; Longo, E.; Cavalcante, L. S. Structural Evolution, Growth Mechanism and Photoluminescence Properties of $CuWO_4$ Nanocrystals. *Ultrason. Sonochem.* **2017**, *38*, 256–270.

(112) Lhermitte, C. R.; Bartlett, B. M. Advancing the Chemistry of $CuWO_4$ for Photoelectrochemical Water Oxidation. *Acc. Chem. Res.* **2016**, *49* (6), 1121–1129.

(113) Yourey, J. E.; Bartlett, B. M. Electrochemical Deposition and Photoelectrochemistry of $CuWO_4$, a Promising Photoanode for Water Oxidation. *J. Mater. Chem.* **2011**, *21* (21), 7651.

(114) Yourey, J. E.; Kurtz, J. B.; Bartlett, B. M. Water Oxidation on a $CuWO_4$-WO_3 Composite Electrode in the Presence of $[Fe(CN)6]^{3-}$: Toward Solar Z-Scheme Water Splitting at Zero Bias. *J. Phys. Chem. C* **2012**, *116* (4), 3200–3205.

(115) Zhang, H.; Yilmaz, P.; Ansari, J. O.; Khan, F. F.; Binions, R.; Krause, S.; Dunn, S. Incorporation of Ag Nanowires in $CuWO_4$ for Improved Visible Light-Induced Photoanode Performance. *J. Mater. Chem. A* **2015**, *3* (18), 9638–9644.

(116) Chen, L.; Shet, S.; Tang, H.; Ahn, K.; Wang, H.; Yan, Y.; Turner, J.; Chen, L.; Shet, S.; Tang, H.; et al. Amorphous Copper Tungsten Oxide with Tunable Band Gaps. *J. Appl. Phys.* **2010**, *108* (043502).

(117) Chang, Y.; Braun, A.; Deangelis, A.; Kaneshiro, J.; Gaillard, N. Effect of Thermal Treatment on the Crystallographic, Surface Energetics, and Photoelectrochemical Properties of Reactively Cosputtered Copper Tungstate for Water Splitting. *J. Phys. Chem. C* **2011**, *115* (51), 25490–25495.

(118) Bohra, D.; Smith, W. A. Improved Charge Separation via Fe-Doping of Copper Tungstate Photoanodes. *Phys. Chem. Chem. Phys.* **2015**, *17* (15), 9857–9866.

(119) Nam, K. M.; Cheon, E. A.; Shin, W. J.; Bard, A. J. Improved Photoelectrochemical Water Oxidation by the $WO_3/CuWO_4$ Composite with a Manganese Phosphate Electrocatalyst. *Langmuir* **2015**, *31* (39), 10897–10903.

(120) Davi, M.; Mann, M.; Ma, Z.; Schrader, F.; Drichel, A.; Budnyk, S.; Rokicinska, A.; Kustrowski, P.; Dronskowski, R.; Slabon, A. An MnNCN-Derived Electrocatalyst for $CuWO_4$ Photoanodes. *Langmuir* **2018**, *34* (13), 3845–3852.

(121) Zhang, Z.; Xiao, C.; Li, S. $CuWO_4$ Films Grown via Seeding-Hydrothermal Method for Photoelectrochemical Water Oxidation. *Mater. Lett.* **2018**, *232*, 25–28.

(122) Wang, D.; Bassi, P. S.; Qi, H.; Zhao, X.; Gurudayal; Wong, L. H.; Xu, R.; Sritharan, T.; Chen, Z. Improved Charge Separation in $WO_3/CuWO_4$ Composite Photoanodes for Photoelectrochemical Water Oxidation. *Materials (Basel).* **2016**, *9* (5), 348.

(123) Salimi, R.; Sabbagh Alvani, A. A.; Naseri, N.; Du, S. F.; Poelman, D. Visible-Enhanced Photocatalytic Performance of $CuWO_4/WO_3$ Hetero-Structures: Incorporation of Plasmonic Ag Nanostructures. *New J. Chem.* **2018**, *42* (13), 11109–11116.

(124) Ye, W.; Chen, F.; Zhao, F.; Han, N.; Li, Y. CuWO4 Nanoflake Array-Based Single-Junction and Heterojunction Photoanodes for Photoelectrochemical Water Oxidation. *ACS Appl. Mater. Interfaces* **2016**, *8* (14), 9211–9217.

(125) Pilli, S. K.; Deutsch, T. G.; Furtak, T. E.; Brown, L. D.; Turner, J. A.; Herring, A. M. $BiVO_4/CuWO_4$ Heterojunction Photoanodes for Efficient Solar Driven Water Oxidation. *Phys. Chem. Chem. Phys.* **2013**, *15* (9), 3273–3278.

(126) Gao, Y.; Hamann, T. W. Quantitative Hole Collection for Photoelectrochemical Water Oxidation with $CuWO_4$. *Chem. Commun.* **2017**, *53* (7), 1285–1288.

(127) Gao, Y.; Hamann, T. W. Elucidation of $CuWO_4$ Surface States During Photoelectrochemical Water Oxidation. *J. Phys. Chem. Lett.* **2017**, *8* (12), 2700–2704.

(128) Kudo, A.; Omori, K.; Kato, H. A Novel Aqueous Process for Preparation of Crystal Form-Controlled and Highly Crystalline $BiVO_4$ Powder from Layered Vanadates at Room Temperature and Its Photocatalytic and Photophysical Properties. *J. Am. Chem. Soc.* **1999**, *121* (49), 11459–11467.

(129) Tokunaga, S.; Kato, H.; Kudo, A. Selective Preparation of Monoclinic and

Tetragonal $BiVO_4$ with Scheelite Structure and Their Photocatalytic Properties. *Chem. Mater.* **2001**, *13* (12), 4624–4628.

(130) Li, G. First-Principles Investigation of the Surface Properties of Fergusonite-Type Monoclinic $BiVO_4$ Photocatalyst. *RSC Adv.* **2017**, *7*, 9130–9140.

(131) Oshikiri, M.; Boero, M. Water Molecule Adsorption Properties on the $BiVO_4$ (100) Surface. *J. Phys. Chem. B* **2006**, *110* (18), 9188–9194.

(132) Iwase, A.; Kudo, A. Photoelectrochemical Water Splitting Using Visible-Light-Responsive $BiVO_4$ Fine Particles Prepared in an Aqueous Acetic Acid Solution. *J. Mater. Chem.* **2010**, *20* (35), 7536–7542.

(133) Mouli, S.; Martinez, C.; Hernández, S.; Bensaid, S.; Saracco, G.; Russo, N. Elucidation of Important Parameters of $BiVO_4$ Responsible for Photo-Catalytic O_2 Evolution and Insights about the Rate of the Catalytic Process. *Chem. Eng. J.* **2014**, *245*, 124–132.

(134) Abdi, F. F.; Savenije, T. J.; May, M. M.; Dam, B.; Van De Krol, R. The Origin of Slow Carrier Transport in $BiVO_4$ Thin Film Photoanodes: A Time-Resolved Microwave Conductivity Study. *J. Phys. Chem. Lett.* **2013**, *4* (16), 2752–2757.

(135) Seabold, J. A.; Zhu, K.; Neale, N. R. Efficient Solar Photoelectrolysis by Nanoporous Mo:$BiVO_4$ through Controlled Electron Transport. *Phys. Chem. Chem. Phys.* **2014**, *16* (3), 1121–1131.

(136) Zhong, D. K.; Choi, S.; Gamelin, D. R. Near-Complete Suppression of Surface Recombination in Solar Photoelectrolysis by "Co-Pi" Catalyst-Modified W:$BiVO_4$. *J. Am. Chem. Soc.* **2011**, *133* (45), 18370–18377.

(137) Zachäus, C.; Abdi, F.; Peter, L. M. P.; van de Krol, R. Photocurrent of $BiVO_4$ Is Limited by Surface Recombination, Not Surface Catalysis. *Chem. Sci.* **2017**, *8*, 3712–3719.

(138) Kim, T. W.; Choi, K. S. Nanoporous BiVO4 Photoanodes with Dual-Layer Oxygen Evolution Catalysts for Solar Water Splitting. *Science* **2014**, *343* (6174), 990–994.

(139) Kim, J. H.; Lee, J. S. $BiVO_4$-Based Heterostructured Photocatalysts for Solar Water Splitting: A Review. *Energy Environ. Focus* **2014**, *3* (4), 339–353.

(140) Su, J.; Liu, C.; Liu, D.; Li, M.; Zhou, J. Enhanced Photoelectrochemical Performance of the $BiVO_4$/Zn:$BiVO_4$ Homojunction for Water Oxidation.

ChemCatChem **2016**, 1–9.

(141) Grigioni, I.; Abdellah, M.; Corti, A.; Dozzi, M. V.; Hammarström, L.; Selli, E. Photoinduced Charge-Transfer Dynamics in WO_3 /$BiVO_4$ Photoanodes Probed through Midinfrared Transient Absorption Spectroscopy. *J. Am. Chem. Soc.* **2018**, *140* (42), 14042–14045.

(142) Liu, C.; Su, J.; Guo, L. Comparison of Sandwich and Fingers-Crossing Type WO_3/$BiVO_4$ Multilayer Heterojunctions for Photoelectrochemical Water Oxidation. *RSC Adv.* **2016**, *6* (33), 27557–27565.

(143) Antuch, M.; Millet, P.; Iwase, A.; Kudo, A. The Role of Surface States during Photocurrent Switching: Intensity Modulated Photocurrent Spectroscopy Analysis of $BiVO_4$ Photoelectrodes. *Appl. Catal. B Environ.* **2018**, *237* (May), 401–408.

(144) Grigioni, I.; Stamplecoskie, K. G.; Jara, D.; Dozzi, M. V.; Oriana, A.; Cerullo, G.; Kamat, P. V.; Selli, E. The Wavelength Dependent Ultrafast Charge Carrier Separation in the WO_3/$BiVO_4$ Coupled System. *ACS Energy Lett.* **2017**, *2*, 1362–1367.

(145) Grigioni, I.; Corti, A.; Dozzi, M. V.; Selli, E. Photoactivity and Stability of WO_3/$BiVO_4$ Photoanodes: Effects of the Contact Electrolyte and of Ni/Fe Oxyhydroxide Protection. *J. Phys. Chem. C* **2018**, *122* (25), 13969–13978.

(146) Seo, J. H.; Park, G.; Oh, K. H.; Kang, S. H.; Lee, H. C.; Cho, S. K.; Nam, K. M. Analysis of Charge Separation Processes in WO_3-$BiVO_4$ Composite for Efficient Photoelectrochemical Water Oxidation. *J. Electroanal. Chem.* **2017**, *789*, 17–23.

(147) Hu, Y.-S.; Kleiman-Shwarsctein, A.; Stucky, G. D.; McFarland, E. W. Improved Photoelectrochemical Performance of Ti-Doped α-Fe_2O_3 Thin Films by Surface Modification with Fluoride. *Chem. Commun.* **2009**, No. 19, 2652–2654.

(148) Ling, Y.; Wang, G.; Wheeler, D. A.; Zhang, J. Z.; Li, Y. Sn-Doped Hematite Nanostructures for Photoelectrochemical Water Splitting. *Nano Lett.* **2011**, *11* (5), 2119–2125.

(149) Hou, Y.; Zuo, F.; Dagg, A.; Feng, P. Visible Light-Driven α-Fe_2O_3 Nanorod/Graphene/$BiV_{1-x}Mo_xO_4$ Core/Shell Heterojunction Array for Efficient Photoelectrochemical Water Splitting. *Nano Lett.* **2012**, *12* (12), 6464–6473.

(150) Le Formal, F.; Grätzel, M.; Sivula, K. Controlling Photoactivity in Ultrathin

Hematite Films for Solar Water-Splitting. *Adv. Funct. Mater.* **2010**, *20* (7), 1099–1107.

(151) Wang, Y.; Wang, L.; Wu, H. Enhanced Microwave Absorption Properties of α-Fe_2 O_3 -Filled Ordered Mesoporous Carbon Nanorods. *Materials (Basel).* **2013**, *6* (4), 1520–1529.

(152) Wang, J.; Feng, B.; Su, J.; Guo, L. Enhanced Bulk and Interfacial Charge Transfer Dynamics for Efficient Photoelectrochemical Water Splitting: The Case of Hematite Nanorod Arrays. *ACS Appl. Mater. Interfaces* **2016**, *8* (35), 23143–23150.

(153) Lin, Y.; Yuan, G.; Sheehan, S.; Zhou, S.; Wang, D. Hematite-Based Solar Water Splitting: Challenges and Opportunities. *Energy Environ. Sci.* **2011**, *4* (12), 4862.

(154) Blake, R. L.; Hessevick, R. .; Zoltai, T.; Finger, L. W. Refinement of Hematite Structure. *Am. Mineral.* **1966**, *51*, 123.

(155) Mirbagheri, N.; Wang, D.; Peng, C.; Wang, J.; Huang, Q.; Fan, C.; Ferapontova, E. E. Visible Light Driven Photoelectrochemical Water Oxidation by Zn- and Ti-Doped Hematite Nanostructures. *ACS Catal.* **2014**, *4* (6), 2006–2015.

(156) Dunn, H. K.; Feckl, J. M.; Müller, A.; Fattakhova-Rohlfing, D.; Morehead, S. G.; Roos, J.; Peter, L. M.; Scheu, C.; Bein, T. Tin Doping Speeds up Hole Transfer during Light-Driven Water Oxidation at Hematite Photoanodes. *Phys. Chem. Chem. Phys.* **2014**, *16* (44), 24610–24620.

(157) Ponomarev, E. A.; Peter, L. M. A Generalized Theory of Intensity Modulated Photocurrent Spectroscopy (IMPS). *J. Electroanal. Chem.* **1995**, *396* (1–2), 219–226.

(158) Ponomarev, E. A.; Peter, L. M. A Comparison of Intensity Modulated Photocurrent Spectroscopy and Photoelectrochemical Impedance Spectroscopy in a Study of Photoelectrochemical Hydrogen Evolution at P-InP. *J. Electroanal. Chem.* **1995**, *397* (1–2), 45–52.

(159) Peter, L. M.; Wijayantha, K. G. U.; Tahir, A. A. Kinetics of Light-Driven Oxygen Evolution at α-Fe_2O_3 Electrodes. *Faraday Discuss.* **2012**, *155* (0), 309–322.

(160) Zachäus, C.; Abdi, F.; Peter, L. M.; van de Krol, R. Photocurrent of $BiVO_4$ Is Limited by Surface Recombination, Not Surface Catalysis. *Chem. Sci.* **2017**, *8*, 4–7.

(161) Cachet, H.; Sutter, E. M. M. Kinetics of Water Oxidation at TiO_2 Nanotube Arrays at

Different PH Domains Investigated by Electrochemical and Light-Modulated Impedance Spectroscopy. *J. Phys. Chem. C* **2015**, *119* (45), 25548–25558.

(162) Peter, L. M. Dynamic Aspects of Semiconductor Photoelectrochemistry. *Chem. Rev.* **1990**, *90* (5), 753–769.

(163) Klotz, D.; Ellis, D. S.; Dotan, H.; Rothschild, A. Empirical in Operando Analysis of the Charge Carrier Dynamics in Hematite Photoanodes by PEIS, IMPS and IMVS. *Phys. Chem. Chem. Phys.* **2016**, *18* (34), 23438–23457.

(164) Márquez, A.; Rodríguez-Pérez, M. J.; Anta, J. A.; Rodríguez-Gattorno, G.; Bourret, G. R.; Oskam, G.; Berger, T. Defects in Porous Networks of WO_3 Particle Aggregates. *ChemElectroChem* **2016**, *3* (4), 658–667.

(165) Liu, Y.; Zhao, L.; Su, J.; Li, M.; Guo, L. Fabrication and Properties of a Branched $(NH_4)_x$ WO_3 Nanowire Array Film and a Porous WO_3 Nanorod Array Film. *ACS Appl. Mater. Interfaces* **2015**, *7* (6), 3532–3538.

(166) Hossain, M. K.; Samu, G. F.; Gandha, K. H.; Santhanagopalan, S.; Liu, J. P.; Janáky, C.; Rajeshwar, K. Solution Combustion Synthesis, Characterization, and Photocatalytic Activity of $CuBi_2O_4$ and Its Nanocomposites with CuO and α-Bi_2O_3. *J. Phys. Chem. C* **2017**, *121*, 8252–8261.

(167) Upul Wijayantha, K. G.; Saremi-Yarahmadi, S.; Peter, L. M. Kinetics of Oxygen Evolution at α-Fe_2O_3 Photoanodes: A Study by Photoelectrochemical Impedance Spectroscopy. *Phys. Chem. Chem. Phys.* **2011**, *13* (12), 5264.

(168) Chen, Z.; Dinh, H. N.; Miller, E. *Photoelectrochemical Water Splitting: Standards, Experimental Methods, and Protocols*, 1st ed.; Springer US, 2013.

(169) Wang, M.; Zai, J.; Wei, X.; Chen, W.; Liang, N.; Xu, M.; Qi, R. N-Type Hedgehog-like $CuBi_2O_4$ Hierarchical Microspheres: Room Temperature Synthesis and Their Photoelectrochemical Properties. *CrystEngComm* **2015**, *17*, 4019–4025.

(170) Martín, A. J.; Maffiotte, C.; Chaparro, A. M. Mechanisms for the Growth of Thin Films of WO_3 and Bronzes from Suspensions of WO_3 Nanoparticles. *ECS Trans.* **2015**, *64* (29), 43–56.

(171) Granqvist, C. G. Electrochromic Tungsten Oxide Films : Review of Progress 1993 - 1998. *Sol. Energy Mater. Sol. Cells* **2000**, *60*, 201–262.

(172) Johansson, M. B.; Mattsson, A.; Lindquist, S.-E.; Niklasson, G. A.; Österlund, L.

The Importance of Oxygen Vacancies in Nanocrystalline WO_{3-x} Thin Films Prepared by DC Magnetron Sputtering for Achieving High Photoelectrochemical Efficiency. *J. Phys. Chem. C* **2017**, *121* (13), 7412–7420.

(173) Klotz, D.; Ellis, D. S.; Dotan, H.; Rothschild, A. Empirical *in Operando* Analysis of the Charge Carrier Dynamics in Hematite Photoanodes by PEIS, IMPS and IMVS. *Phys. Chem. Chem. Phys.* **2016**, *18* (34), 23438–23457.

(174) Zachäus, C.; Abdi, F. F.; Peter, L. M.; Van De Krol, R. Photocurrent of $BiVO_4$ Is Limited by Surface Recombination, Not Surface Catalysis. *Chem. Sci.* **2017**, *8* (5), 3712–3719.

(175) Jongh, P. E. De; Vanmaekelbergh, D. Investigation of the Electronic Transport Properties of Nanocrystalline Particulate TiO_2 Electrodes by Intensity-Modulated Photocurrent Spectroscopy. *J. Phys. Chem. B* **1997**, *5647* (96), 2716–2722.

(176) Pyper, K. J.; Yourey, J. E.; Bartlett, B. M. Reactivity of $CuWO_4$ in Photoelectrochemical Water Oxidation Is Dictated by a Midgap Electronic State. *J. Phys. Chem. C* **2013**, *117* (47), 24726–24732.

(177) Hu, D.; Diao, P.; Xu, D.; Xia, M.; Gu, Y.; Wu, Q.; Li, C.; Yang, S. Copper(II) Tungstate Nanoflake Array Films: Sacrificial Template Synthesis, Hydrogen Treatment, and Their Application as Photoanodes in Solar Water Splitting. *Nanoscale* **2016**, *3* (8), 5892–5901.

(178) Zhang, J.; Richardson, H. W. Copper Compounds. *Ullmann's Encycl. Ind. Chem.* **2006**, 1–31.

(179) Tong, H.; Jiang, Y.; Zhang, Q.; Li, J.; Jiang, W.; Zhang, D.; Li, N.; Xia, L. Enhanced Interfacial Charge Transfer on WO_3 Photoanode by Molecular Iridium Catalyst. *ChemSusChem* **2017**, *10* (16), 3268–3275.

(180) Zhu, T.; Chong, M. N.; Chan, E. S.; Ocon, J. D. Electrochemically-Synthesized Tungstate Nanocomposites γ-WO_3/$CuWO_4$ and γ-WO_3/$NiWO_4$ Thin Films with Improved Band Gap and Photoactivity for Solar-Driven Photoelectrochemical Water Oxidation. *J. Alloys Compd.* **2018**, *762*, 90–97.

(181) Gaillard, N.; Chang, Y.; Deangelis, A.; Higgins, S.; Braun, A. A Nanocomposite Photoelectrode Made of 2.2 EV Band Gap Copper Tungstate ($CuWO_4$) and Multi-Wall Carbon Nanotubes for Solar-Assisted Water Splitting. *Int. J. Hydrogen Energy*

2013, *38* (8), 3166–3176.

(182) Sfaelou, S.; Pop, L. C.; Monfort, O.; Dracopoulos, V.; Lianos, P. Mesoporous WO_3 Photoanodes for Hydrogen Production by Water Splitting and PhotoFuelCell Operation. *Int. J. Hydrogen Energy* **2016**, *41* (14), 5902–5907.

(183) Peter, L. M.; Upul Wijayantha, K. G. Photoelectrochemical Water Splitting at Semiconductor Electrodes: Fundamental Problems and New Perspectives. *ChemPhysChem* **2014**, *15* (10), 1983–1995.

(184) Tolod, K.; Hernández, S.; Russo, N. Recent Advances in the $BiVO_4$ Photocatalyst for Sun-Driven Water Oxidation: Top-Performing Photoanodes and Scale-Up Challenges. *Catalysts* **2017**, *7* (1), 13.

(185) Li, H.; Quan, X.; Chen, S.; Yu, H. Ferroelectric-Enhanced Z-Schematic Electron Transfer in $BiVO_4$-$BiFeO_3$-$CuInS_2$ for Efficient Photocatalytic Pollutant Degradation. *Appl. Catal. B Environ.* **2017**, *209*, 591–599.

(186) Jeong, H. W.; Jeon, T. H.; Jang, J. S.; Choi, W.; Park, H. Strategic Modification of $BiVO_4$ for Improving Photoelectrochemical Water Oxidation Performance. *J. Phys. Chem. C* **2013**, *117* (18), 9104–9112.

(187) Antony, R. P.; Bassi, P. S.; Abdi, F. F.; Chiam, S. Y.; Ren, Y.; Barber, J.; Loo, J. S. C.; Wong, L. H. Electrospun Mo-$BiVO_4$ for Efficient Photoelectrochemical Water Oxidation: Direct Evidence of Improved Hole Diffusion Length and Charge Separation. *Electrochim. Acta* **2016**, *211*, 173–182.

(188) Abdi, F. F.; Van De Krol, R. Nature and Light Dependence of Bulk Recombination in Co-Pi-Catalyzed $BiVO_4$ Photoanodes. *J. Phys. Chem. C* **2012**, *116* (17), 9398–9404.

(189) Jung, H.; Chae, S. Y.; Shin, C.; Min, B. K.; Joo, O.-S.; Hwang, Y. J. Effect of the Si/TiO_2 /$BiVO_4$ Heterojunction on the Onset Potential of Photocurrents for Solar Water Oxidation. *ACS Appl. Mater. Interfaces* **2015**, *7* (10), 5788–5796.

(190) Xie, J.; Guo, C.; Yang, P.; Wang, X.; Liu, D.; Li, C. M. Bi-Functional Ferroelectric $BiFeO_3$ Passivated $BiVO_4$ Photoanode for Efficient and Stable Solar Water Oxidation. *Nano Energy* **2017**, *31*, 28–36.

(191) Xu, S.; Fu, D.; Song, K.; Wang, L.; Yang, Z.; Yang, W.; Hou, H. One-Dimensional WO3/BiVO4 Heterojunction Photoanodes for Efficient Photoelectrochemical Water

Splitting. *Chem. Eng. J.* **2018**, *349*, 368–375.

(192) Ding, J.; Kim, K. 1-D WO_3 @ $BiVO_4$ Heterojunctions with Highly Enhanced Photoelectrochemical Performance. *Chem. Eng. J.* **2018**, *334*, 1650–1656.

(193) Choi, J.; Sudhagar, P.; Kim, J. H.; Kwon, J.; Kim, J.; Terashima, C.; Fujishima, A.; Song, T.; Paik, U. WO_3/W:$BiVO_4$/$BiVO_4$ Graded Photoabsorber Electrode for Enhanced Photoelectrocatalytic Solar Light Driven Water Oxidation. *Phys. Chem. Chem. Phys.* **2017**, *19* (6), 4648–4655.

(194) Liu, C.; Yang, Y.; Li, J.; Chen, S.; Li, W.; Tang, X. An in Situ Transformation Approach for Fabrication of $BiVO_4$/WO_3 Heterojunction Photoanode with High Photoelectrochemical Activity. *Chem. Eng. J.* **2017**, *326*, 603–611.

(195) Zeng, Q.; Li, J.; Li, L.; Bai, J.; Xia, L.; Zhou, B. Synthesis of WO_3/$BiVO_4$ Photoanode Using a Reaction of Bismuth Nitrate with Peroxovanadate on WO_3 Film for Efficient Photoelectrocatalytic Water Splitting and Organic Pollutant Degradation. *Appl. Catal. B Environ.* **2017**, *217*, 21–29.

(196) Cesar, I.; Kay, A.; Martinez, J. A. G.; Grätzel, M. Translucent Thin Film Fe_2O_3 Photoanodes for Efficient Water Splitting by Sunlight: Nanostructure-Directing Effect of Si-Doping. *J. Am. Chem. Soc.* **2006**, *128* (14), 4582–4583.

(197) Lee, C. Y.; Wang, L.; Kado, Y.; Killian, M. S.; Schmuki, P. Anodic Nanotubular/Porous Hematite Photoanode for Solar Water Splitting: Substantial Effect of Iron Substrate Purity. *ChemSusChem* **2014**, *7* (3), 934–940.

(198) Li, M.; Yang, Y.; Ling, Y.; Qiu, W.; Wang, F.; Liu, T.; Song, Y.; Liu, X.; Fang, P.; Tong, Y.; et al. Photoelectrochemical Water Splitting with Mesoporous Hematite Prepared by a Solution-Based Colloidal Approach Photoelectrochemical Water Splitting with Mesoporous Hematite Prepared by a Solution-Based Colloidal Approach. *Nano Lett.* **2010**, *132* (4), 7436–7444.

(199) Xie, K.; Guo, M.; Huang, H.; Liu, Y. Fabrication of Iron Oxide Nanotube Arrays by Electrochemical Anodization. *Corros. Sci.* **2014**, *88*, 66–75.

(200) Kang, J. S.; Noh, Y.; Kim, J.; Choi, H.; Jeon, T. H.; Ahn, D.; Kim, J. Y.; Yu, S. H.; Park, H.; Yum, J. H.; et al. Iron Oxide Photoelectrode with Multidimensional Architecture for Highly Efficient Photoelectrochemical Water Splitting. *Angew. Chemie - Int. Ed.* **2017**, *56* (23), 6583–6588.

(201) Descostes, M.; Mercier, F.; Thromat, N.; Beaucaire, C.; Gautier-Soyer, M. Use of XPS in the Determination of Chemical Environment and Oxidation State of Iron and Sulfur Samples: Constitution of a Data Basis in Binding Energies for Fe and S Reference Compounds and Applications to the Evidence of Surface Species of an Oxidized Pyrite in a Carbonate Medium. *Appl. Surf. Sci.* **2000**, *165* (4), 288–302.

(202) Xia, W.; Wang, H.; Zeng, X.; Han, J.; Zhu, J.; Zhou, M.; Wu, S. High-Efficiency Photocatalytic Activity of Type II SnO/Sn_3O_4 heterostructures via Interfacial Charge Transfer. *CrystEngComm* **2014**, *16* (30), 6841–6847.